



**UNIVERSITÉ  
DE GENÈVE**

UNIVERSITY OF GENEVA

MASTER THESIS

---

**Simulation for a HV-CMOS Sensor for  
High-Luminosity ATLAS Tracker Upgrade**

---

*Author:*  
Le LI

*Supervisor:*  
Prof. Dr. Giuseppe IACOBUCCI,  
Dr. Moritz KIEHN,  
Dr. Mathieu BENOIT

*A thesis submitted in fulfillment of the requirements  
for the degree of Master of Science*

*in the*

Département de Physique Nucléaire et Corpusculaire  
Faculté des Sciences

February 8, 2019



## Declaration of Authorship

I, Le LI, declare that this thesis titled, "Simulation for a HV-CMOS Sensor for High-Luminosity ATLAS Tracker Upgrade" and the work presented in it are my own. I confirm that:

- This work was done wholly or mainly while in candidature for a research degree at this University.
- Where any part of this thesis has previously been submitted for a degree or any other qualification at this University or any other institution, this has been clearly stated.
- Where I have consulted the published work of others, this is always clearly attributed.
- Where I have quoted from the work of others, the source is always given. With the exception of such quotations, this thesis is entirely my own work.
- I have acknowledged all main sources of help.
- Where the thesis is based on work done by myself jointly with others, I have made clear exactly what was done by others and what I have contributed myself.

Signed: Le Li

Date: 08/02/2019



UNIVERSITY OF GENEVA

# *Abstract*

Faculté des Sciences  
Département de Physique Nucléaire et Corpusculaire

Master of Science

## **Simulation for a HV-CMOS Sensor for High-Luminosity ATLAS Tracker Upgrade**

by Le LI

In 2024-2026, the LHC will undergo the High Luminosity upgrade to increase its instantaneous luminosity by 2.5 – 3.5 times in order to facilitate the precision measurements of known particles and to enlarge the explorable mass range of beyond-Standard-Model physics. The augmented luminosity will lead to an increase in the number of interactions and the amount of radiation around the interaction points. The resolution and radiation-hardness of the current ATLAS detector are not sufficient to operate in such an environment. Besides, the current components of the ATLAS detector will reach the end of their designed life by then. Therefore, it is planned that the tracking system of the ATLAS experiment will be completely replaced by an all-silicon Inner Tracker (ATLAS ITk). Novel sensor technologies are under study for the construction of the ATLAS ITk. One promising candidate is the monolithic silicon pixel sensors fabricated through the high voltage complementary metal-oxide-semiconductor (HV-CMOS) technology. The production cost of such sensors can be substantially reduced with respect to the conventional hybrid sensors. The reason is that the sensing part and the readout electronics of a monolithic sensor are fabricated on a single piece of silicon, as opposed to the time-consuming and costly bump-bonding process to connect the sensing and readout parts of the hybrid sensors. To contribute to the research and development of the ATLASPix chip, one of the HV-CMOS candidate designs, the simulation of the FE-I4 beam telescope, a crucial device to measure the performance of the sensor under development, has been performed with the generic silicon tracking devices simulation package AllPix<sup>2</sup>. Besides, the Technology Computer Aided Design (TCAD) simulation of the ATLASPix Simple matrix, one of the three matrices on the the first fully monolithic large-scale prototype of the ATLASPix design, has been performed. The simulation results will be presented in this thesis.



## *Acknowledgements*

To begin with, I would like to express my sincere gratitude to Prof. Dr. Giuseppe Iacobucci, Dr. Moritz Kiehn, and Dr. Mathieu Benoit for providing me with this opportunity to work on this interesting master project, and for their supervision and help throughout the project and thesis writing. This master project is a precious experience that has broadened my horizon, and provided me with insight to hardware development in high energy physics. Moreover, I am indebted to Dr. Sergio Sevilla and Dr. Winnie Wong for their valuable ideas and suggestions to my work which have inspired me to solve the problems I have encountered during the project.

Secondly, I would like to thank Dr. Moritz Kiehn and Dr. Mateus Vicente for their help with the AllPix<sup>2</sup> simulation package and the Proteus reconstruction package, and for their ideas and advices throughout the construction and validation of the simulation of the FE-I4 telescope. Thank Simon Spannagel and Koen Wolters for their timely support when I had problems with the AllPix<sup>2</sup> package, as well as Dr. Branistic Ristic for his detailed explanations of the FE-I4 telescope. Thank Dr. Mathieu Benoit for having introduced me to monolithic sensors, the ATLASPix design, and TCAD, along with his indispensable help in building the TCAD simulation model of the ATLASPix. I also appreciate the help with the Synopsis TCAD software from Dr. Lingxin Meng and Francesco Di Bello. Moreover, my heartfelt gratefulness goes to Xuefeng Ding for the support he has provided throughout my master years, both in academic research and in life.

Last but not the least, I am very grateful to my family and my friends. Especially, I would like to thank my parents for their emotional and financial support, without which it would not have been possible for me to finish this master project. In addition, I would like to thank Nanjun Zhou and JAC Kruczek for their company and moral support, which helped me through the difficult times.



# Contents

<b>Declaration of Authorship</b>	<b>iii</b>
<b>Abstract</b>	<b>v</b>
<b>Acknowledgements</b>	<b>vii</b>
<b>1 Introduction</b>	<b>1</b>
<b>2 The ATLAS Experiment</b>	<b>3</b>
2.1 Overview of the ATLAS Experiment . . . . .	3
2.2 The ATLAS Detector . . . . .	3
2.3 Upgrade Programs of ATLAS . . . . .	5
2.3.1 Phase 0 Upgrade . . . . .	6
2.3.2 Phase I Upgrade . . . . .	7
2.3.3 Phase II Upgrade . . . . .	7
2.4 Summary . . . . .	8
<b>3 Silicon Particle Detectors</b>	<b>11</b>
3.1 Interaction of Charged Particles with Matter . . . . .	11
3.1.1 Collision Loss Process of Massive Charged Particles . . . . .	11
3.1.2 Energy-Loss Minimum . . . . .	12
3.1.3 Restricted Energy-Loss and Fermi Plateau . . . . .	12
3.2 Physics Properties of Silicon Semiconductor . . . . .	13
3.2.1 Structure of Silicon Crystals . . . . .	13
3.2.2 Transport of Charge Carriers in Silicon Semiconductors . . . . .	15
3.3 Detection Mechanism of Silicon Particle Detectors . . . . .	18
3.3.1 P-n Junction and Depletion Region . . . . .	18
3.3.2 Charge Collection and Signal Formation . . . . .	20
3.3.3 Influence of Radiation Damage . . . . .	21
3.4 Silicon Pixel Sensor Types . . . . .	22
3.4.1 Hybrid Pixel Detector . . . . .	22
3.4.2 Monolithic Silicon Radiation Detector . . . . .	23
3.5 Summary . . . . .	26
<b>4 Simulation of FE-I4 Telescope</b>	<b>29</b>
4.1 Testbeam Experiment . . . . .	29
4.2 The FE-I4 Telescope . . . . .	29
4.2.1 Telescope Description . . . . .	29
4.2.2 Reconstruction . . . . .	30
4.3 Data Sample . . . . .	31
4.4 Simulation of the FE-I4 Telescope . . . . .	31
4.5 Validation of the Simulation . . . . .	33
4.6 Evaluation of Reconstruction . . . . .	34

4.7	Summary	37
<b>5</b>	<b>TCAD Simulation of ATLASPix</b>	<b>41</b>
5.1	Technology Computer Aided Design	41
5.2	Model of Single Pixel	42
5.2.1	Simulated Structure	42
5.2.2	Simulation of Device Operations	43
	Electrical Properties	43
	Response to Particle	47
5.3	Simulation of Four-Pixel Matrix	53
5.3.1	Simulated Structure	53
5.3.2	Simulation of Device Operation	55
	Electrical Properties	55
	Response to Minimum Ionizing Particle	57
5.4	Summary	60
<b>6</b>	<b>Summary and Outlook</b>	<b>63</b>
<b>A</b>	<b>Appendix A</b>	<b>65</b>
<b>B</b>	<b>Appendix B</b>	<b>67</b>

## Chapter 1

# Introduction

Particle physics is the branch of physics that studies the nature of the elementary particles, in other words, the presumed indivisible building blocks of matter, and the interactions between them. The term "atom" dates back to ancient Greece, when philosophers such as Leucippus [1] and Democritus [2] proposed the doctrine of "atomism", which stated that all matter consists of indivisible elementary particles called "atoms" [3]. The first scientific interpretation of the nature of atoms was proposed by the British chemist John Dalton in the 19th century in the study of the masses of tin oxides. He hypothesized that everything was composed of atoms, which are indivisible by chemical means but can combine to form more complex compounds, and that chemical reactions result in the rearrangement of the atoms in the reactants and the products. Dalton's theory was proved successful by empirical experiments and thus marked the first scientific theory of atoms [4]. The modern subatomic particle physics started from the discovery of cathode rays [5] which were later identified to be electrons. This discovery showed that atoms are further divisible and paved the way for the studies of subatomic particles. Our modern theories about particle physics is summarized with the Standard Model. This theory has successfully described all known elementary particles and three of the four fundamental forces: the electromagnetic, the strong, and the weak interactions. The Standard Model has proven to be successful, with many of its results confirmed by the observation of cosmic rays and accelerator experiments, such as the discovery of the Higgs boson in 2012 [6][7], the last missing building block which is responsible for the mass of elementary particles. However, there remains several important observations that the Standard Model cannot explain. For instance, the baryonic matter described by the Standard Model accounts for only 5% of the universe, and the other 95% percent remains unknown and is referred to as dark matter and dark energy [8]. Besides, the Standard Model does not include gravity, the fourth fundamental natural force [9]. Rigorous experiments are being carried out to test the Standard Model to a high precision, and to look for hints of the existence of new physics phenomena beyond the scope of the Standard Model.

The Large Hadron Collider (LHC) at CERN is so far the most powerful experimental tool to test the Standard Model in the world [10]. It accelerates protons to a high energy before smashing them against each other. In these energetic collisions, the quarks and gluons in the protons interact with each other, and exotic processes that are otherwise only possible in violent cosmic events may take place. These processes are recorded by particle detectors installed around the collision point. By analyzing the data collected by the detectors, it is then possible to reconstruct the processes that have taken place and measure at what rate they occur. The experimental results are then compared with theoretical results of the Standard Model, to see if they agree to a sufficient level. If the measurement results deviate from the theory, it means that new physics processes may have taken place. The abnormal

experimental results also serve as a guidance to theorists as they work on possible theories beyond the Standard Model. Since its launch in 2009, the analysis results of the LHC data have yielded numerous results, including the discovery of several exotic quark resonances [11], the precision measurement of the W boson, the discovery of the Higgs boson, and preliminary results on searches for supersymmetric particles, one of the Standard Model extensions [12]. By the end of 2023, it is expected that most components of the LHC and the detectors will reach the end of their designed lifetime. To further explore the potential of the LHC, a major upgrade aiming at the increase of the luminosity is planned during 2024-2026. The upgraded accelerator will be referred to as the High-Luminosity LHC, it will collide protons at an increased luminosity and produce 10 times higher integrated luminosity than it does now. However, the High Luminosity upgrade poses a great challenge on the granularity and radiation-hardness of its tracking detectors, so that the detectors will be able to distinguish the increased amount of interactions and survive in an extremely radiant environment.

ATLAS is a general purpose detector on the LHC. It is constituted by several concentric sub-detectors layers that measure important properties of the particles produced in the collisions. The tracking detector is a sub-detector that lies in the innermost volume surrounding the collision point. It consists of several layers of carefully aligned pixel or strip sensors and straw detectors, and serves to measure the tracks and decay vertices of charged particles, which are crucial for determining what particles have been created, when they have decayed were they unstable, and what have been their decay products. During the HL-LHC runs, it is expected that two hundred collisions will take place every 25 ns, the final products from which will leave more than 10,000 tracks in the tracking detectors. Therefore, sensors with advanced temporal and spatial resolution will be needed. Besides, the HL-LHC will deliver ten times greater dose of radiation than the LHC, thus posing a much more stringent requirement on the radiation hardness of the sensor. It is planned that the tracking system of ATLAS will be replaced by an all-silicon Inner Tracker (ITk) which will be constructed with next-generation silicon pixel and strip sensors. Rigorous investigations of various novel sensor technologies along with research and development (R&D) of the candidate sensors are ongoing. The simulation work which will be included in this thesis is within the scope of the R&D of ATLASPix, a candidate pixel sensor for the pixel layer of the ATLAS ITk fabricated using the monolithic HV-CMOS technology, a promising novel sensor fabrication method inspired by the commercial CMOS approach for imaging sensors.

Chapter 2 is an overview of the ATLAS experiment, including an introduction to the collaboration, the current detector, and the upgrade schedule. Chapter 3 addresses relevant semiconductor detector physics. It starts with a discussion of the physics principles through which a charged particle interacts with matter. Then the properties of silicon semiconductors utilized for particle detection are presented in 3.2. Section 3.3 is about silicon sensors, including the signal formation process and the radiation damage they may suffer when they are crossed by charged particles. Finally, the two major types of silicon particle sensors, the hybrid and the monolithic sensors, are illustrated in Section 3.4 using the ATLAS IBL planar sensor and the ATLASPix sensor as examples. Chapter 4 is devoted to the simulation work of the FE-I4 telescope, the beam telescope employed in the Geneva testbeam experiments to measure the resolution and sensitivity of sensors under development, including the ATLASPix prototype. Last but not the least, Chapter 5 presents the TCAD simulation of one of the pixel matrices on the ATLASPix prototype.

## Chapter 2

# The ATLAS Experiment

This chapter is an introduction to the ATLAS experiment, a major experiment on the LHC. Section 2.1 gives a brief overview of the physics goals of the experiment and the collaboration, and Section 2.2 illustrates the structure and function of the ATLAS detector and its sub-detectors. Section 2.3 presents the upgrade projects for ATLAS for each LHC upgrade phase, with an emphasis on the upgrade of the tracking system.

### 2.1 Overview of the ATLAS Experiment

ATLAS (A Toroidal LHC Apparatus) is a particle detector located on one of the collision points on the LHC, a circular particle collider built and operated by CERN, the European Organization for Nuclear Research. It is mainly designed to accelerate and collide protons, but it also collides lead ions or protons with lead ions for the study of heavy ion physics.

The LHC lies in a tunnel beneath the Franco-Swiss border near Geneva. Fig. 2.1a shows a map of the LHC tunnel. It consists of two 27 km long circular beam pipes surrounded with thousands of superconducting dipole magnets to guide the particles along the pipes and accelerating structures to boost the energy of the particle beams. There are four collision points along the ring, each with quadrupole magnets to focus the beam. As shown in fig. 2.1b, inside the LHC, the particle beams travel in opposite directions in one of the two beam pipes and get accelerated up to 99.999999% the speed of light. At the collision points, they are focused to collide by the focusing quadrupole magnets. The particles that do not collide will continue traveling until next collision point, where they will be focused to collide again [10].

The ATLAS detector is a general purpose detector designed to measure a broad range of signals and detect any physical processes that may take place during the proton collisions. ATLAS is one of the two LHC experiments that discovered the Higgs boson in 2012. Its current focus is on the precision measurement of the properties of the Higgs boson and the search for traces of beyond standard model physics.

The ATLAS experiment is one of the biggest experiments on the LHC. The ATLAS detector is 46 meters in length, 25 meters in diameter, and weighs 7,000 tonnes [14]. The ATLAS collaboration includes over 3,000 physicists from over 175 institutions in 38 countries.

### 2.2 The ATLAS Detector

The ATLAS detector serves to detect and identify particles created in the proton collisions on the LHC. It is made of four concentric cylindrical sub-detectors: the Inner Detector, the calorimeters, the Muon Spectrometer, and the magnet systems. Each

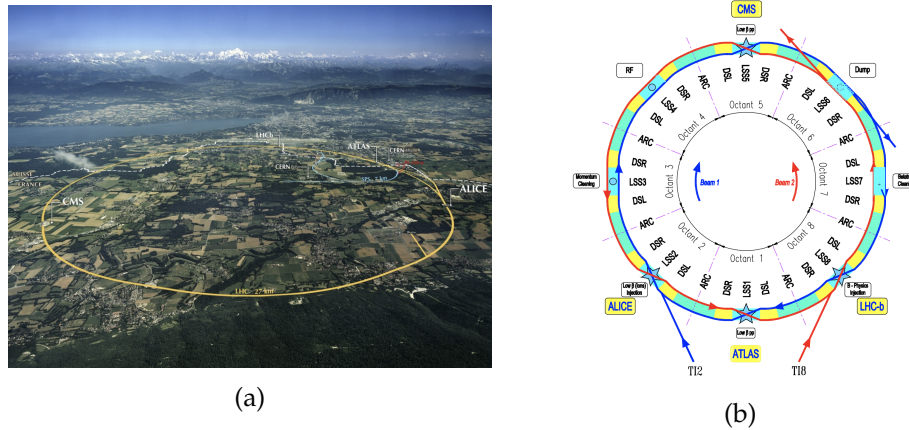


FIGURE 2.1: **a**: Landscape photo of where the LHC is located. The white dotted line is the Franco-Swiss border. The LHC tunnel is denoted with the yellow circle and the locations of the four major experiments are marked. **b**: Schematic drawing of the passage of protons inside the LHC. The four interaction sites are denoted by stars. The red and blue arrowed lines denote the two proton beams. The beams are injected at the interaction points. They travel in different directions in separate beampipes, and at each interaction point, they are brought to collide. Images from [13] and [10].

of the sub-detector performs a different but complementary task. The Inner Detector serves to track particles; the calorimeters measure the energy of easily absorbed particles; the Muon Spectrometer performs additional measurement of the highly-penetrative muons; the magnet system fills the detector with a strong magnetic field to bend the tracks of charged particles to enable the measurement of their charge and momentum, and to make their absorption by calorimeters easier. Neutrinos are the only type of elementary particles that cannot be detected directly, and are inferred by the "missing energy" among detected particles. By combining the information obtained from the sub-detectors, one can reconstruct what physics processes have taken place. Each sub-detector of ATLAS is further made up of several layers.

### Inner Detector

The Inner Detector (ID) is a small and complex tracking detector at innermost of ATLAS. It consists of several layers of millions of small and highly-sensitive sensing units that emit a signal if hit by a particle. When a particle travels through the ID, it will hit a series of sensing units, and leave a precise record of its trajectory through the device. As is mentioned before, a strong magnetic field fills the whole detector, causing the tracks of the charged particles to bend. The direction of the curve indicates whether the particle is positively or negatively charged, and the degree of curvature reveals the particle's momentum. The ID of ATLAS is made of three concentrically aligned cylindrical sub-detectors: the Pixel Detector made of small pixel sensors which measures particle tracks and vertices next to the collision point with a resolution of  $14 \times 115 \mu\text{m}^2$ ; the Semiconductor Tracker constructed with silicon microstrips, and the Transition Radiation Tracker (TRT) made of straw tubes to provide a measurement precision of  $130 \mu\text{m}$  over a large area. Each sub-detector consists of a barrel and two endcaps. Fig. 2.2 is a schematic picture of the Inner Detector.

### Calorimeters

Calorimeters measure the energy of particles by interacting with and absorbing

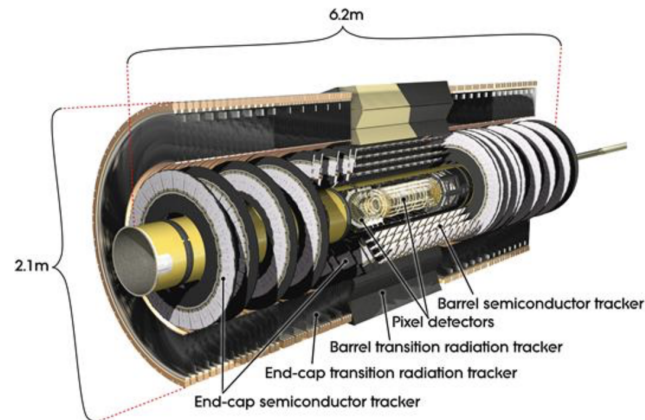


FIGURE 2.2: Computer generated image of the Inner Detector. The sub-layers including the Pixel Detector, the Semiconductor Tracker, and the Transition Radiation Tracker are shown in the image. Image from [14].

them. The calorimetry system of ATLAS includes the Liquid Argon (LAr) Calorimeter that works with liquid argon cooled down to  $-183^{\circ}\text{C}$  and the Tile Hadronic Calorimeter made of 500000 plastic scintillators tiles. The Tile Hadronic Calorimeter consists of 3 barrels that measure the energy of hadronic particles that interacts via the strong force. The LAr Calorimeter is made of one barrel and two endcaps. The LAr barrel is an electromagnetic calorimeter that measures the energy of electrons and photons, while the LAr endcaps serve as both electromagnetic and hadronic calorimeters.

### Muon Spectrometers

Muon Spectrometers are placed at the outermost to absorb and make additional measurements of the energy and tracks of highly-penetrative muons. The Muon Spectrometers consist of various components, including the Thin Gap Chambers and the Resistive Plate Chambers for triggering and the measurement of the 2nd coordinate of muon tracks; the Monitored Drift Tubes; as well as the Cathode Strip Chambers that measure the track curvature.

### Magnet system

The Magnet system includes the Barrel Toroid, the Endcap Toroid, and Central Solenoid Magnet. The Central Solenoid Magnet is placed around the Inner Detector and produces uniform electric field of 2 Tesla inside the Inner Detector to bend particle tracks for momentum detection. Besides, 8 Barrel Toroids and 2 Endcap Toroids are placed outside the calorimeters. The toroids serve to bend particle tracks to make it easier for the calorimeters and the muon detectors to contain particle tracks. The magnetic field provided by the toroids vary from 2 Tesla to 8 Tesla.

Fig. 2.3 shows the full structure of the ATLAS detector with all of its sub-detectors.

## 2.3 Upgrade Programs of ATLAS

The current plan for the running period of the LHC since its launch until 2037 is summarized in Fig. 2.4. The total running period is separated into three evolution

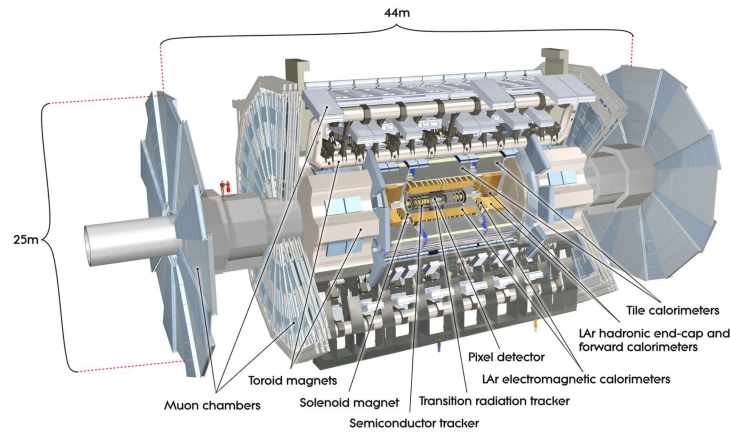


FIGURE 2.3: Computer generated image of the ATLAS detector. Image from [14].

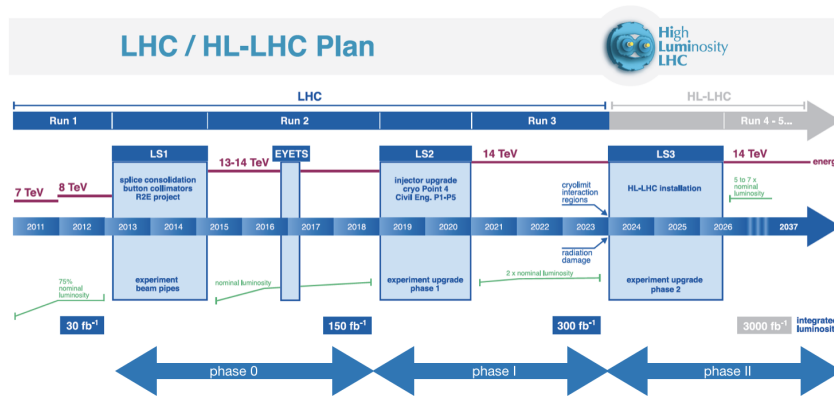


FIGURE 2.4: Plan of running phases of the LHC/HL-LHC from 2011-2037, with the goals in energy and luminosity for each period. Image from [15]

phases, each consisting of physics runs and long shutdowns.

### 2.3.1 Phase 0 Upgrade

The phase 0 period started with the Long Shutdown 1 (LS1) in early 2013 and ended with the end of Run-II at the end of 2018. The LHC restarted in 2015 as planned. During Run-II, proton collision energy has been ramped up to 13 TeV and a peak luminosity of  $2 \times 10^{34}/\text{cm}^2\text{s}^{-1}$ , twice the designed luminosity, has been reached. The LHC has delivered integrated luminosity of  $160 \text{ fb}^{-1}$  in the Run-II.

The main upgrade activity for the ATLAS tracking system during phase 0, i.e., the LS1, is the addition of the Inner B Layer (IBL) to the Pixel Detector between the beam pipe and the old inner layer of the Pixel Detector (B-layer). To make the necessary space for the IBL, the old beam pipe was replaced by a new beam pipe whose radius was reduced to 25mm from 29mm.

The IBL consists of 14 staves surrounding the beam pipe, each holding 32 or 16 modules of pixel sensors. The angles of the sensors to the radial direction are between 0 and  $27^\circ$ . Simulated images of the structure of the IBL are shown in Fig. 2.5.

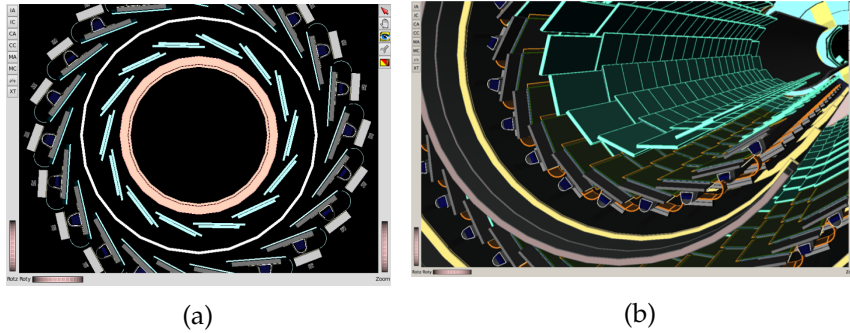


FIGURE 2.5: Simulated images of the IBL. **a**: transverse planes of the beam pipe (pink circle), the ibl layer with modules and staves (drawn in blue), the support tube (white circle), and the old B-layer (outermost gray sensors). **b**: view from inside the Pixel Detector showing the geometrical arrangement of IBL sensors. Image from [16].

The IBL serves to preserve tracking resolution and efficiency at an improved luminosity, where the B-layer and other pixel layers suffer from high pile-up occupancies and irreparable failures due to radiation damage. The IBL uses the Front End chip IBM version 4 (FE-I4) read-out chip, which has 4 buffers per chip to store pixel hit information, while the Front End chip IBM version 3 (FE-I3) chip used by the old B Layer only have 1 buffer per chip, and thus the IBL is able to store and process hit information more quickly. Besides, the IBL is closer to the interaction point and its pixel size is smaller, so the resolution of vertex reconstruction and b-tagging is improved. The planar pixel sensors and the FE-I4 readout chip used by the IBL will be discussed in detail in section 3.4.1.

In addition, a series of consolidation works have been done to the detector, such as renewing the cooling systems for the Inner Detector and replacing services and power supplies [17].

### 2.3.2 Phase I Upgrade

This period will start with the LS2 in 2019 and will last until the end of Run-III in 2023. In Run-III, the LHC is projected to achieve a center of mass collision energy of 14 TeV and a peak luminosity of  $2 \times 10^{34}/\text{cm}^{-2}\text{s}^{-1}$ . It will deliver to its experiments  $300 \text{ fb}^{-1}$  of data. The end of Phase I marks the end of the LHC era. At that time, the components of the LHC such as the superconducting magnets will reach the end of their designed lifetime due to the amount of radiation damage they will have received, and will need to be replaced.

The phase I upgrade will focus on the the addition of new Small Wheels to the muon chambers and updating the trigger system, in order to extract physics information of higher-granularity and resolution from the detected data [17]. No hardware upgrade has been proposed to the Inner Detector during this upgrade. It will continue working until the phase II upgrade, when it will be completely replaced.

### 2.3.3 Phase II Upgrade

The phase II running period, also referred to as HL-LHC era, will start in 2024 with LS3 and last until 2037. During the two years of LS3, a major upgrade of the LHC will take place, where 1.2 km of the accelerator will be renovated.

The most important parameter of the phase II upgrade is the luminosity, a quantity that is directly proportional to the amount of useful data. The goal is to increase

peak luminosity to  $5 - 7 \times 10^{34}/\text{cm}^{-2}\text{s}^{-1}$ , and thus deliver 10 times greater integrated luminosity than what will have been delivered during the LHC era.

The major impact of the increased luminosity is the drastically augmented amount of radiation damage and pile-up, and the main concern of detector research and development (R&D) is how to maintain detector performance under the HL-LHC conditions.

As for radiation damage, the annual dose of radiation delivered to detectors by the HL-LHC will be equivalent to the total dose the current LHC has delivered from when it came into operation to now. Thus, to maintain detector performance on the HL-LHC will require next-generation detectors at least ten times more radiation resistant than current detectors. The requirement of radiation resistance is especially high for the tracking sub-detector, as it is only a few centimeters from the interaction point, and receives the highest amount of radiation.

Another challenge is higher pile-up. In the HL-LHC, thousands of particles will be produced per bunch crossing, and for each event, the tracking sub-detector will experience more than 10,000 hits. Detectors of much higher granularity are required to avoid misidentification of tracks. The correct identification of tracks is of crucial importance to physics probes. For example, electroweak phenomena are characterized by having isolated leptons in their final products. If tracks that are not due to this interaction is wrongly assigned to this event, the leptons may appear non-isolated.

One major upgrade project for the ATLAS tracking sub-detector is the construction of a new all-silicon Inner Tracker (ITk) to replace the current ID, as the silicon parts of the ID will reach the end of their designed life, and the number of particle tracks per event will exceed the occupancy limit of the gas-based TRT.

The design concept of the ITk is similar to that of the ID, with sensors arranged on several concentric cylinder layers. The schematic baseline layout of the ITk is shown in Fig. 2.6. The ITk will have in its central region five layers of silicon pixel sensors, which will be surrounded by 5 layers of strip sensors on the outer region. The forward regions of the ITk will be covered by six pixel endcaps and six strip endcaps to provide coverage for particles coming in high  $\eta$  directions [17].

To maintain tracking efficiency in the harsh HL-LHC environment, next generation silicon pixel sensors with high granularity, fast response time, and high radiation-hardness are being studied for the pixel layers of the ITk. One of the promising candidates under development is the monolithic pixel sensor fabricated using the high voltage complementary metal-oxide-semiconductor (HV-CMOS) technology, an adaptation of the commercial CMOS technology for camera imaging pixel sensors with HV add-ons to shorten response time and to increase radiation-hardness. The ATLASPix is one of the candidate designs using the HV-CMOS technology, and the study of the performances of the first fully monolithic prototype of this design with Technology Computer Aided Design (TCAD) will be covered in Chapter 5.

## 2.4 Summary

The ATLAS detector is a powerful general-purpose detector on the LHC. By combining the data measured by its sub-detectors, it is possible to reconstruct a plethora of physics processes that take place during the proton collisions on the LHC. The analysis of ATLAS data has yielded many important results, including the discovery of the Higgs boson. During the LHC shutdowns, upgrades for the ATLAS detector

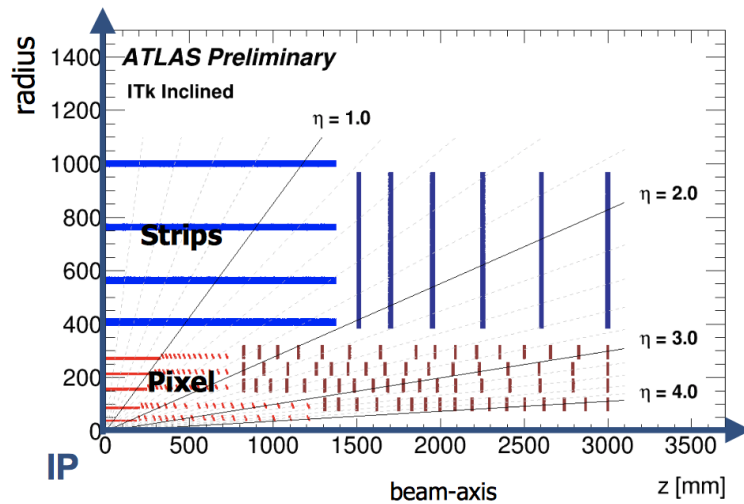


FIGURE 2.6: Designed layout of the transverse plane of ATLAS ITK. The pixel part is drawn in red and strip part in blue. The ITK will have radius of about 1 m and length of about 3 m. Image from [18].

have been planned to help ATLAS to cope with the increased beam energy and intensity for the next LHC running phase. The major upgrades of the tracking systems include the addition of the IBL layer to increase the resolution of b-tagging in phase 0, and the replacement of the tracking system by the all-silicon ITK in phase II. New technologies are under study for the ITK sensors, and the ATLASPix design using with the HV-CMOS technology, the study of which will be presented in Chapter 5 of this thesis, is a promising candidate sensor design with high resolution and relatively low production cost.



## Chapter 3

# Silicon Particle Detectors

As is discussed in Chapter 2, the silicon part of the ATLAS tracking detector is made up of several concentric layers of small pixel or strip sensors that generate a signal when a charged particle crosses them. This chapter is dedicated to the detection mechanism of these sensors. To start with, section 3.1 explains the process through which a charged particle loses its energy and ionizes the atoms when it goes through a medium such as a semiconductor. Section 3.2 is about the basic physics properties of the silicon semiconductor that are relevant to detector fabrication, including the structure of the silicon crystal that allows the presence of charge carriers, and doping, an important practice to alter the concentration charge carriers and the resistivity of the semiconductor. Processes responsible for signal formation, including the transport of charge carriers in the semiconductor, the generation of excess charge carriers by incoming particles, and the recombination of charge carriers, are also discussed. Last but not least, section 3.3 explains the structure and detecting mechanism of the typical silicon particle sensors, and the influence of radiation damage to them, using the ATLAS IBL planar sensor and the prototype sensor studied in Chapter 5 called ATLASPix 1, as examples.

### 3.1 Interaction of Charged Particles with Matter

#### 3.1.1 Collision Loss Process of Massive Charged Particles

When charged particles traverse a medium, such as a silicon sensor, they lose energy by ionizing the atoms in the medium along their trajectories. This process is called collision loss process [19].

The average energy loss due to collision loss process was studied by Bohr [20], Bethe [21], and Bloch [22]. For an incoming particle of mass  $m_p$ , velocity  $v = \beta c$ , charge  $ze$ , the energy loss per unit path is given by (see [23])

$$-\frac{dE}{dx} = 0.1535 \frac{\rho z^2 Z}{A} \left\{ \ln \left[ \frac{2m_e c^2 W_m}{(h\nu_p)^2} \right] - 1 \right\} [\text{MeV}/\text{cm}]. \quad (3.1)$$

where  $\rho$  is the density of the medium in unit  $\text{g}/\text{cm}^3$ ,  $Z$  is the atomic number, and  $A$  is the atomic weight of the material.  $m_e = 9.11 \times 10^{-28}$  g is the mass of the electron,  $h$  and  $\nu_p$  are experimental parameters related to the material. For silicon,  $h\nu_p = 31.06$  eV.

The term  $W_m$  denotes the maximum transferable energy from particles to atomic electrons. For high-energy particles traversing thin mediums such as a tracking detector, the deposited energy is usually much smaller than the energy of the particles. The expression of  $W_m$  is derived assuming the collision loss process is a two-body scattering process where the target is almost at rest (see Section 1.3.1 of [24] for

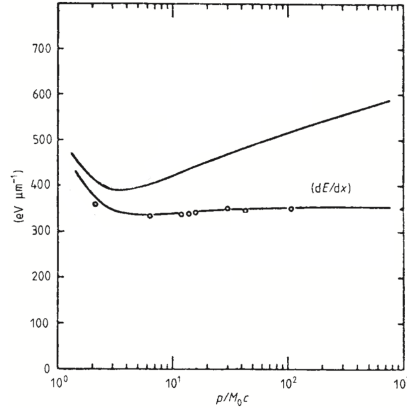


FIGURE 3.1: Energy loss per unit length ( $\text{eV}/\mu\text{m}$ ) of particles in silicon vs. the  $\beta\gamma$  value of the particle. The curve on the top is the energy loss predicted by the Bethe-Bloch formula, and the lower curve is the restricted energy loss and the fermi plateau. The predicted curve of the restricted energy loss is compared to experimental data (denoted with circles) for detector of thickness of  $300 \mu\text{m}$ . Figure from [23].

derivations).  $W_m$  is expressed as

$$W_m = 2m_e c^2 \beta^2 \gamma^2 \left[ 1 + \left( \frac{m_e}{m_p} \right)^2 + 2\gamma \frac{m_e}{m_p} \right]^{-1}, \quad (3.2)$$

where  $m_p$  and  $m_e$  are the rest mass of the particle and of electron.  $\gamma$  is the Lorentz factor, given by

$$\gamma = \frac{1}{\sqrt{1 - \beta^2}}, \quad \text{where } \vec{\beta} = \frac{\vec{v}}{c}.$$

$\vec{v}$  is the velocity of the incoming particle. When  $m_p \gg m_e$ , the maximum transferrable energy is approximated as

$$W_m \approx 2mc^2 \beta^2 \gamma^2 \quad (3.3)$$

### 3.1.2 Energy-Loss Minimum

Eq. 3.1 shows that the energy loss per unit length ( $-dE/dx$ ) depends on the product of  $\beta\gamma$  through the term  $W_m$ , and is the same for different types of particles. The dependence of energy loss on  $\beta\gamma$  values of incoming particles for a given medium is shown in Fig. 3.1. At low  $\beta\gamma$  values, the collision energy loss decreases quickly with the increase of  $\beta\gamma$ . The collision energy loss reaches a minimum at around

$$\beta_{\min} \gamma_{\min} \approx 3, \quad (3.4)$$

which corresponds to  $\beta_{\min} \approx 0.95$ . An incoming particle at energy-loss minimum is called a minimum ionizing particle (mip). Beyond the minimum, the energy loss increases again.

### 3.1.3 Restricted Energy-Loss and Fermi Plateau

The deposited energy in solid state detectors is usually smaller than the energy loss suffered by the incoming particle, as typical detectors are not thick enough to absorb all ionized electrons, especially the most energetic ones emitted along the direction

of the particle. It is useful to define an effective detectable maximum transferred energy  $W_0$  to describe the deposited energy in the detector. Thus, at energies  $\beta \approx 1$ , the energy-loss formula reduces to the so-called restricted energy-loss formula

$$-\left(\frac{dE}{dx}\right)_{\text{restricted}} = 0.1535 \frac{\rho z^2 Z}{A \beta^2} \ln \left[ \frac{2mcW_0}{(hv_p)^2} \right]. \quad (3.5)$$

Eq. 3.5 indicates that at high energies the energy loss is proportional to  $W_0$ . When the energy of the incoming particle increases,  $W_0$  will eventually reach a constant value, and in turn  $-\left(\frac{dE}{dx}\right)_{\text{restricted}}$  will reach a plateau called the Fermi Plateau. The restricted energy loss vs. the  $\beta\gamma$  value of the incoming particle and the fermi plateau are shown, compared to experimental data for silicon detector of thickness of 300  $\mu\text{m}$  in Fig. 3.1. A detailed treatment of this topic can be found in Section 2.1.1.4 of [24].

## 3.2 Physics Properties of Silicon Semiconductor

Semiconductors are a group of materials having conductivities between that of conductors and insulators. They are useful for electronic devices because their conductivity and electrical behaviors can be easily manipulated by the addition of small amount of impurities, a process known as doping. Among semiconductors, silicon (Si) is the most important material for the fabrication of Very-Large-Scale-Integrated circuits (VLSI) and radiation detectors. In this section, the physics properties of silicon crystals and how doping influences these properties will be introduced.

### 3.2.1 Structure of Silicon Crystals

Silicon crystals have face-centered diamond cubic structure. A ball-and-stick model of the unit cell of this structure is shown in Fig. 3.2a. The entire crystal lattice is generated by repeating the unit cell.

The electrons in an isolated silicon atom occupy quantized energy levels in a similar way to the Bohr's model for a Hydrogen atom [25], and each energy level can be occupied by at most two electrons with opposite spin according to the Pauli Exclusion Principle. As the isolated atoms are brought together to form the crystal lattice, the electrons interact with each other, leading to the split of their energy levels into  $N$  narrowly separated energy-levels, where  $N$  is the number of the electrons. If the number of electrons is large enough, the separation between the levels becomes so infinitesimally small that they can be better represented as a continuous energy band on the energy scale [23]. The energy bands of the electrons in the silicon crystal is shown in Fig. 3.2b. They include the valence band, where the electrons are bound in localized states, and the conduction band, where the electrons can move and thus conduct, and the forbidden band, where no electron can exist. The forbidden band is caused by the potential posed on each electron by the other electrons and the nucleus [26].

Silicon atoms have four valence electrons. Inside a crystal, each atom forms four covalent bonds with its four nearest atoms to fully occupy its valence energy-shell. At low temperatures, the energy of the valence electrons lie in the valence band, which means they are bound by covalent bonds and cannot participate in conduction. As temperature increases, the energy of the electrons becomes larger. When the energy increase of an electron is bigger than the energy gap, this electron jumps into

the conduction band. In other words, the thermal vibration of the electron becomes strong enough to break the covalent bond for it to become available for conduction. When an electron escapes a covalent bond, an electron deficiency, called a hole, is left in the covalent bond. A hole may be filled by nearby electrons, resulting in the change of its location. Thus, a hole can be considered as a free charge carrier with a charge opposite to that of an electron. Under the influence of external electric field, holes and electrons move in opposite directions. [23]

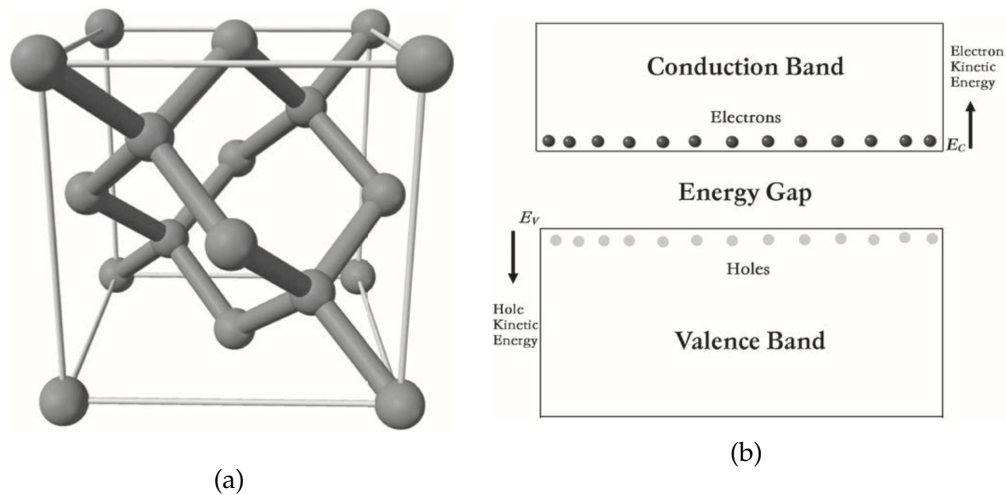


FIGURE 3.2: **a:** Ball and stick model of the unit cell of the silicon crystal. **b:** Energy bands of electrons in a silicon crystal. Images from [23].

## Doping

Doping is the intentional introduction of controlled amount of impurities in the production of semiconductor to vary the electrical properties such as the conductivity of the material. A semiconductor without doping, such as the pure silicon crystal mentioned in section 3.2.1, is referred to as an intrinsic semiconductor, and a doped semiconductor is called an extrinsic semiconductor.

Two of the most commonly used dopants are boron and phosphorus. When boron or phosphorus atoms are introduced in a silicon crystal, they will replace silicon atoms at certain lattice sites. A phosphorus atom has five valence electrons, and when it is at a lattice site, it will form four covalent bonds with the four nearest silicon atoms and release one electron. The released electron occupies an energy level slightly below the lower edge of the conduction band, and is usually excited to the conduction band at room temperature. This type of impurities are called donors, and the doped material is called n-type material. Meanwhile, a boron atom has three valence electrons. When a boron atom is present in a silicon crystal, an additional electron will be accepted to form four covalent bonds. The energy level of the additional electron is slightly above the valence band, and thus it is easy for a valence electron to be excited to this state, leaving a hole in the valence band. Boron and similar impurities are called acceptors and the doped material is referred to as a p-type material. The energy bands and impurity energy levels are shown in Fig. 3.3. Usually, in extrinsic semiconductors, the concentration of thermally excited electrons and holes is much lower than that of charge carriers introduced by dopants, so the concentration of charge carriers in extrinsic semiconductors can be approximated as the concentration of dopants.

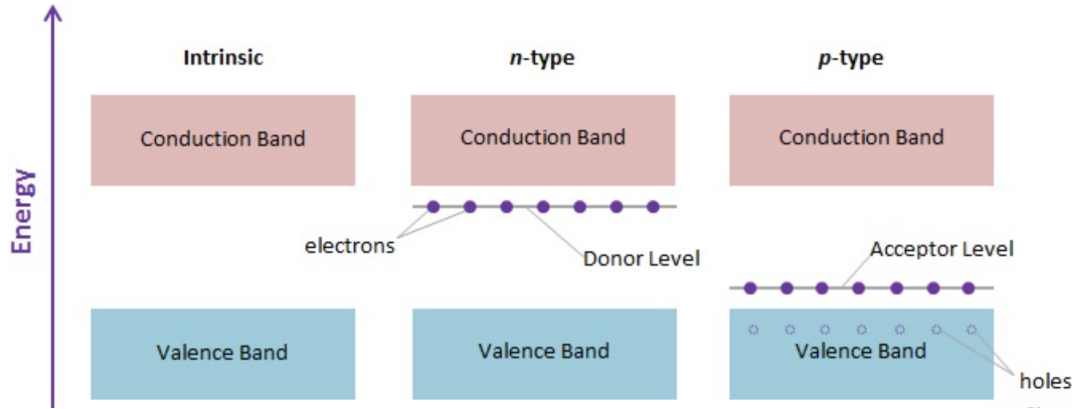


FIGURE 3.3: Energy bands in intrinsic and doped extrinsic semiconductors. Image from [27].

### 3.2.2 Transport of Charge Carriers in Silicon Semiconductors

#### Thermal motion

As is discussed before, charge carriers including electrons and holes do not belong to a single atom but to the whole crystal. They can be considered as free particles with an effective mass that accounts for corrections from their interaction with the lattice.

At temperature above the absolute zero, electrons move with randomly distributed velocities. The statistical behavior of thermal motion of an ensemble of free electrons or other similar microscopic particles is studied in statistical mechanics, which predicts the kinetic energy of thermal motion is directly proportional to the temperature by

$$\frac{1}{2}m_i v_{th,i}^2 = \frac{3}{2}k_B T, \quad (3.6)$$

where  $m_i$  denotes the effective mass of charge carriers, with the subscript  $i = e, h$  for electrons and holes,  $k_B$  is the Boltzmann constant, and  $T$  is the absolute temperature.

$v_{th,n}$  is the thermal velocity of electrons or holes. At 300 K, the thermal velocity of electrons in silicon crystal is

$$v_{th,e} \approx 2.2 \times 10^7 \text{ cm/s.}$$

#### Drift of Charge Carriers and Resistivity

When an external electric field is applied to the semiconductor, the holes will acquire a velocity in the direction of the field, and the electrons in the opposite direction. This velocity is called the drift velocity. The conductivity of a medium is decided mainly by the concentration of its charge carriers, and by their ability to drift.

The drifting ability of charge carriers inside the semiconductor is expressed in terms of drift velocity and drift mobility. The drift mobility  $\mu_i$  ( $i = e, h$ ) is defined as the ratio of the average drift velocity to the strength of the external electric field.

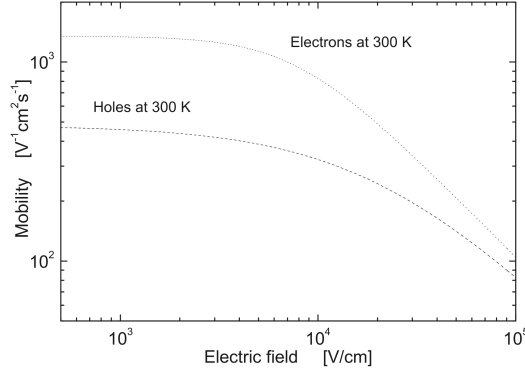


FIGURE 3.4: Drift mobility of electrons and holes ( $\text{V}^{-1}\text{cm}^2\text{s}^{-1}$ ) vs. the electric field ( $\text{V}/\text{cm}$ ) at 300 K as predicted by Eq. 3.11. Image from [23].

The drift current density inside the material is related to the drift velocity as

$$\vec{J}_{\text{dr}} = epv_{\text{dr},h} - env_{\text{dr},e} \quad (3.7)$$

$$= e(\mu_h p + \mu_e n)E \quad (3.8)$$

where  $e$  is the electric charge,  $p(n)$  is the concentration of electrons (holes), and  $E$  denotes the strength of the external electric field. At low electric field, the mobility of electrons and holes is found to be (see [23])

$$\mu_e = \frac{v_{\text{dr},e}}{E} = \frac{-e\tau_{\text{col},e}}{m_e} \quad (3.9)$$

$$\mu_h = \frac{v_{\text{dr},h}}{E} = \frac{e\tau_{\text{col},h}}{m_h} \quad (3.10)$$

where  $\tau_i$ , ( $i = e, h$ ) is the average time that a charge carrier can travel before it collides with other charge carriers. Eq. 3.9 and 3.10 show that, at low electric field, the drift mobility of charge carriers depends on their thermal motion, and will decrease as temperature increases.

At high electric field, the drift mobility becomes dependent on field strength because the influence of the electric field is equivalent or stronger than the thermal motion. The empirical equation describing the dependence of  $\mu_i(E)$  on  $E$  was derived by Thornber (see [23]):

$$\mu_i(E) = \frac{\mu_{0,i}}{[1 + (\mu_{0,i}E/v_i)^m]^{1/m}} \quad (3.11)$$

The mobility calculated using Eq. 3.11 with different field strength at 300 K is shown in Fig. 3.4. At electric field stronger than  $\sim 10^4$  V/cm, the drift velocity of the electron or the hole becomes greater than the thermal velocity, and the drift mobility becomes dependent on the field strength.

The drift mobility is also referred to as conductivity mobility, as the drifting of charge carriers is the main factor influencing the conductivity of the material.

The resistivity  $\rho$  (the inverse of conductivity) is an important electrical property of a material, and is directly related to the drift mobility and the concentration of

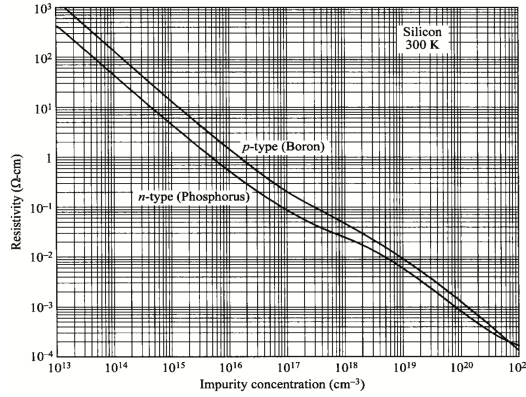


FIGURE 3.5: Resistivity of extrinsic semiconductor vs. doping concentration for p-type and n-type silicon semiconductor at 300 K. Image from [23].

charge carriers. For n-type semiconductors, the resistivity is

$$\rho = \frac{1}{e\mu_e n'}, \quad (3.12)$$

where  $e$  is the electric charge,  $\mu_e$  is the drift mobility of electrons, and  $n$  is the concentration of electrons.

Similarly, for a p-type semiconductor, the resistivity is

$$\rho = \frac{1}{e\mu_h p'}, \quad (3.13)$$

where  $\mu_h$  is the drift mobility of holes, and  $p$  is the concentration of holes.

For extrinsic semiconductors, the resistivity will decrease with the increase of doping concentration, as the doping concentration determines the concentration of charge carriers. The dependence of resistivity on doping concentration is shown in Fig. 3.5.

### Diffusion

Another important transport mechanism of charge carriers in the semiconductor is diffusion. When the distribution of the concentration of carriers inside the material is not uniform, the charge carriers will diffuse from regions of high concentration to regions of low concentration, resulting in the diffusion current. The total diffusion current density  $\vec{J}_{\text{diff}}$  is expressed as

$$\vec{J}_{\text{dif}} = \vec{J}_{\text{dif},e} + \vec{J}_{\text{dif},h} = eD_e\Delta n - eD_h\Delta p, \quad (3.14)$$

where  $e$  denotes the electron charge,  $D_i$  ( $i = e, h$ ) is the diffusion constant for electrons and holes, and  $n$  ( $p$ ) denotes the concentration of electrons (holes).

The total current density in the semiconductor is given by

$$\vec{J} = e(\mu_e n + \mu_h p)\vec{E} + e(D_e\Delta n - D_h\Delta p) \quad (3.15)$$

### Generation and Recombination of Excess Carriers

The concentration of carriers inside a silicon semiconductor is not constant, and excess carriers can be generated thermally or under an external excitation such as a

particle.

The thermal generation and recombination of free electron-hole pairs occur constantly inside the material. However, in doped semiconductors, the thermal excitation of electrons cannot occur directly as it does in pure silicon crystals, as the crystal momenta of the majority and minority carriers are not the same. The creation-recombination processes mainly occur in two steps via the intermediate states formed by crystal defects, which can be introduced through radiation damage. These states are termed generation-recombination centers or trapping centers.

Besides, when a heavy charged particle traverses a silicon semiconductor, excess carriers are created absorbing the deposited energy of the particle. This process is called charge injection. After charge injection, the injected minority carriers tend to recombine with the majority carriers of the semiconductor to restore to equilibrium.

### 3.3 Detection Mechanism of Silicon Particle Detectors

#### 3.3.1 P-n Junction and Depletion Region

A p-n junction is formed when a p-type material is placed adjacent to an n-type material. At the interface, the majority carriers of each material diffuse into each other and recombine, forming a depletion region where almost all free charged carriers are recombined. Inside the depletion region, there is an electric field pointing from n-type material to p-type material, as the depleted n-type region is positively charged, and p-type region negatively charged. This field tends to stop the diffusion of the charge carriers, and grows stronger as the depletion region widens. The system reaches an equilibrium when the fluxes of charge carriers due to diffusion and due to the electric field cancel, and the width of the depletion region remains constant. The depletion region can serve as a particle detector. When a particle passes a p-n junction, the excess charge carriers generated by the particle will drift to the edges of the p-n junction under the electric field inside the depletion region, inducing a current on the charge collection electrode and making it possible to collect the generated charge.

If no external voltage is applied, the electrostatic potential  $\Psi$ , electric field  $\vec{E}$ , and depth of the depletion zone are only determined by the concentrations of charge carriers in the materials forming the p-n junction, and can be obtained by solving the Poisson equation:

$$\frac{d^2\Psi}{dx^2} = -\frac{\rho(x)}{\epsilon}, \quad (3.16)$$

where  $\epsilon = 1.054$  pF/cm is the silicon electric permittivity, and  $\rho(x)$  denotes the charge density in the depletion zone and is given by:

$$\rho(x) = \begin{cases} qN_d, & \text{for } 0 < x < x_n \\ -qN_a, & \text{for } -x_p < x < 0. \end{cases}$$

Inside the depletion region, the total amount of charge is 0, so  $N_d x_n = N_a x_p$ .

By integrating Eq. 3.16 with boundary conditions  $E(x_n) = E(-x_p) = 0$ , the electric field  $E$  is obtained:

$$E(x) = -\frac{d\Psi}{dx} = \begin{cases} E_n(x) = q(N_d/\epsilon)(x - x_n), & \text{for } 0 < x < x_n \\ E_p(x) = -q(N_a/\epsilon)(x + x_p), & \text{for } -x_p < x < 0. \end{cases} \quad (3.17)$$

The electrostatic potential is calculated by integrating Eq. 3.17:

$$\Psi(x) = \begin{cases} \Psi_n(x) = \Psi_n - q[N_d/2\epsilon](x - x_n)^2 & \text{for } 0 < x < x_n \\ \Psi_p(x) = \Psi_p + q[N_a/2\epsilon](x + x_p)^2 & \text{for } -x_p < x < 0. \end{cases} \quad (3.18)$$

The built-in voltage of the p-n junction is defined as

$$V_0 = - \int E(x)dx = \Psi_n - \Psi_p = \frac{k_B T}{q} \ln \left( \frac{N_a N_d}{n_{int}^2} \right) \quad (3.19)$$

For silicon at  $T \approx 300$  K,  $V_0 \approx 0.3 - 0.6$  V. The total depletion depth is calculated to be

$$\begin{aligned} x_n &= \frac{1}{N_d} \sqrt{\frac{2\epsilon V_0}{q} \left( \frac{1}{N_a} + \frac{1}{N_d} \right)^{-1}}, \\ x_p &= \frac{1}{N_a} \sqrt{\frac{2\epsilon V_0}{q} \left( \frac{1}{N_a} + \frac{1}{N_d} \right)^{-1}}, \\ X &= x_n + x_p = \sqrt{\frac{2\epsilon V_0}{q} \left( \frac{1}{N_a} + \frac{1}{N_d} \right)}, \end{aligned}$$

where  $X_n$  and  $X_p$  denotes the depletion depth in n and p regions, while  $X$  is the total depletion depth. The detailed derivation can be found in Section 4.2.1 in [23].

However, the depletion depth of an unpolarized p-n junction is usually a few microns which limits the junction's ability for particle detection, and thus a bias voltage is often applied to widen the depletion depth. When a negative bias voltage of  $V_b < 0$  is applied on the p-side of the junction, the electrostatic potential on the boundaries becomes

$$\begin{aligned} \Psi(-x_p) &= \Psi_p - V_b \\ \Psi(x_n) &= \Psi_n, \end{aligned}$$

and the depletion depth becomes

$$X = \sqrt{\frac{2\epsilon(V_0 + V_b)}{q} \left( \frac{1}{N_a} + \frac{1}{N_d} \right)}.$$

The detectors concerned in this thesis are made of p-n<sup>+</sup> junction for which  $N_a \ll N_d$ . Therefore the depletion depth can be approximated as

$$\begin{aligned} X &\approx x_p = \sqrt{\frac{2\epsilon}{qN_a} (V_0 + V_b)} \\ &\approx \sqrt{\frac{2\epsilon}{q(N_a - N_d)} (V_0 + V_b)} \\ &= \sqrt{\frac{2\epsilon}{q|N_{eff}|} (V_0 + V_b)}, \end{aligned}$$

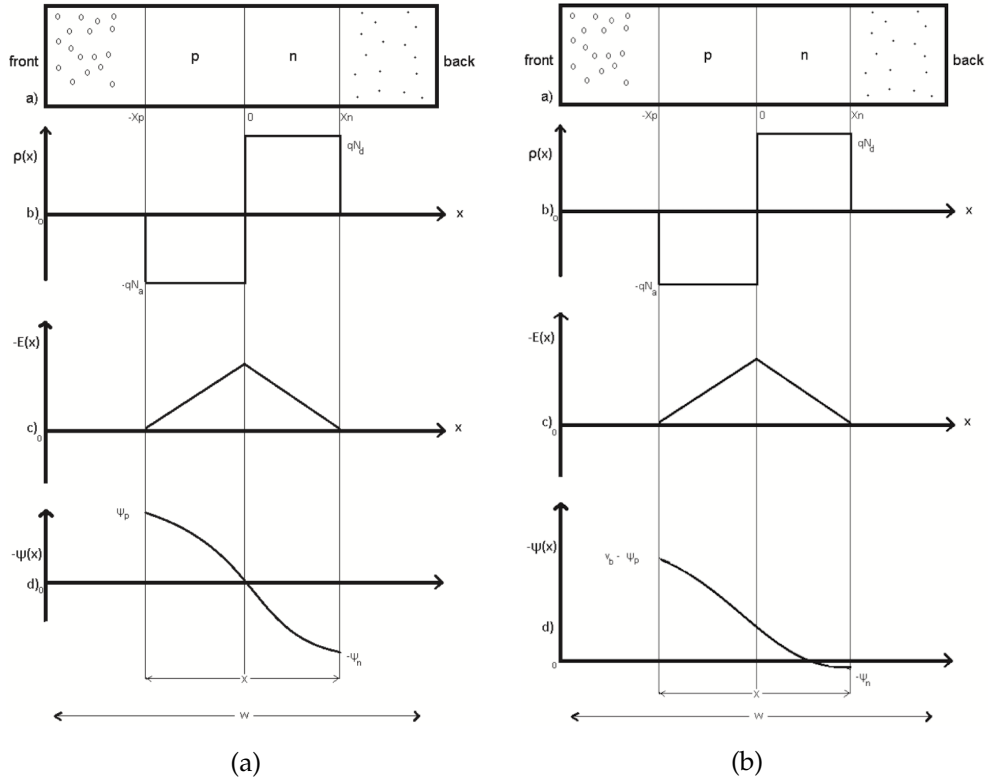


FIGURE 3.6: Illustration of a p-n junction and the distribution of charge density  $\rho(x)$ , electric field  $E(x)$  and electrostatic potential  $\psi(x)$  inside the junction. **a** shows an unpolarized p-n junction, and **b** shows a p-n junction with a bias voltage of  $V_b$ . Image from [23].

where  $N_{\text{eff}} = N_a - N_d$  is the effective dopant concentration. The resistivity of silicon detector is

$$\rho = \frac{1}{\mu q |N_{\text{eff}}|},$$

and the highest measured electron mobility for silicon crystals at room temperature (300K) is  $\mu_e = 1400 \text{ cm}^2/(\text{V}\cdot\text{s})$  [28]. Thus the depletion depth  $X$  can be approximated as

$$X \approx 0.53 \sqrt{\rho(V_0 + V_b)} \quad (3.20)$$

Eq. 3.20 shows that the depletion depth is proportional to the square root of the resistivity of the material. Therefore, the higher the resistivity or the bias voltage, the larger the sensitive volume for particle detection becomes. See Section 4.2.2 in [23] for more details.

### 3.3.2 Charge Collection and Signal Formation

When a charge carrier moves in the proximity of an electrode, an instantaneous current is induced by the change of electrostatic flux lines. According to Ramo theorem (see [29]), the generated charge in the electrode is related to the displacement of the

charge carrier as

$$\Delta q = q \frac{\Delta x}{w}$$

where  $w$  is the thickness of the sensor. The induced current is given by

$$i(x) = \frac{dq}{dt} = \frac{q}{w} \frac{dx}{dt} = \frac{q}{w} v(t).$$

where  $v(t)$  denotes the velocity of the charge carrier. Inside the depletion zone, the velocity of charge carriers is determined by the mobility  $\mu_i$ , ( $i = e, h$ ) of charge carriers and the electric field:

$$\begin{aligned} v_e(t) &= \mu_e E(x) \\ v_h(t) &= \mu_h E(x), \end{aligned}$$

and the electric field in the depletion zone is expressed as

$$E(x) = -\frac{qN_{\text{eff}}}{\epsilon}(x-w) + \frac{V_b - V_f d}{w} = -ax + b.$$

The time it takes for a charge carrier generated at position  $x_0$  to reach the electrode at  $x = w$  is given by

$$\begin{aligned} t_{\text{coll}}(e) &= -\frac{1}{\mu_e a} \ln \left( \frac{aw - b}{ax_0 - b} \right) \\ t_{\text{coll}}(h) &= -\frac{1}{\mu_h a} \ln \left( \frac{-b}{ax_0 - b} \right) \end{aligned}$$

The total amount of charge induced by a charge carrier as it moves from its original position  $x_0$  to the electrode can be obtained by integrating the current over collection time:

$$\begin{aligned} Q_e &= \frac{q}{w}(w - x_0) \\ Q_h &= \frac{q}{w}(x_0), \end{aligned}$$

and the total collected charge is

$$Q_{\text{tot}} = Q_e + Q_h = q. \quad (3.21)$$

Eq. 3.21 indicates that the total amount of charge induced by a charge carrier as it travels to the electrode is the same as the charge it carries. Therefore in a simplified picture, one can say that the charge carrier is collected by the electrode.

### 3.3.3 Influence of Radiation Damage

When an energetic particle traverses a silicon detector, besides generating signals, it also causes damage that degrades detector performance. Radiation damage includes the Total Ionizing Dose (TID), mostly caused by energetic protons and electrons, and Non-Ionizing Energy Loss (NIEL), the displacement damage caused by the scattering of the incoming particle with lattice atoms [30].

The influences of the TID creates additional electron-hole pairs. The electrons produce noise, and the holes tend to be trapped at the Si/SiO<sub>2</sub> interface, influencing the depletion voltage and the charge carrier mobility. In addition, TID deteriorates electronics performance and may result in electronics failure [30].

The NIEL causes crystal defects. The main impacts include the change of effective doping concentration, which in turn will make it more difficult to deplete the sensor, resulting in a smaller detecting area or a need for higher bias voltage.

Besides, NIEL leads to an increased number of generation-recombination centers. Inside the depletion region, these centers give rise to free charges inside the depletion region, and these free charges will move under the electric field of the depletion region, forming a current called leakage current that leads to shot noise or even to destructive thermal runaway. Outside the depletion region, these centers act as trapping centers that facilitate the recombination of the charge generated by the particle, thus reducing the signal strength and the charge collection efficiency.

## 3.4 Silicon Pixel Sensor Types

### 3.4.1 Hybrid Pixel Detector

The hybrid pixel detector is currently the default choice for large scale pixel tracking detectors in LHC experiments [31]. A hybrid pixel consists of an electronically passive sensor and a readout chip connected through the flip-chip bump bonding technology. The sensor collects charge when hit by a particle, the charge is then transported to the readout chip through the bump bonds, where it will be processed and transformed to digital signal for further analysis. The layouts of the individual hybrid pixel and the pixel matrix are illustrated in Fig. 3.7.

A typical sensor is made by placing densely doped n- and p- type implants respectively on the front- and back-side of a highly ohmic ( $\sim 2\text{-}5\text{k}\Omega/\text{cm}$ ) n-type substrate, with aluminum electrodes on the implants. A bias voltage is added between the p<sup>+</sup> and n<sup>+</sup> implants to deplete the sensor. As is shown in Fig. 3.7a, after a particle passes through the sensor, the generated electrons flow to the n<sup>+</sup> implants and the holes to the opposite side, creating a signal in the electrode on the n<sup>+</sup> implant. The signal is then transmitted via the bump bond to the readout chip.

The major advantage of the hybrid pixel technology is that the sensor and the readout chip can be optimized for the LHC demands separately, as the main challenge for the sensor is radiation-hardness while the challenge for the readout chip is the high input rates of  $\sim\text{MHz}/\text{mm}^2$  [31]. However, the hybrid approach has a severe disadvantage. The bump bonding and flip chipping processes are laborious and expensive, and result in tedious production steps and relatively large production budget. [31].

The planar sensor used in the ATLAS IBL is one example of such pixels. The dual-module IBL sensor is 200  $\mu\text{m}$  thick and  $4 \times 2 \text{ cm}^2$  wide. It has planar n<sup>+</sup> implants of an area of  $50 \times 250 \mu\text{m}^2$  [32] on its front-side and 13 ring-shaped p<sup>+</sup> implants, referred to as p-guard rings, on its back. The ring-shape design of the p<sup>+</sup> implants serves to bring the negative bias potential at the bias implants to zero at pixel implants, so to optimize the behavior of the sensors after irradiation. Fig. 3.8 shows the design of the IBL planar sensor matrices.

The readout of the IBL planar sensor is provided by the FE-I4 front end chip, which consists of 26880 pixels arranged in 80 columns and 336 rows. The outline of the FE-I4 pixel array is shown in Fig. 3.9. The FE-I4 pixels have the same size as the

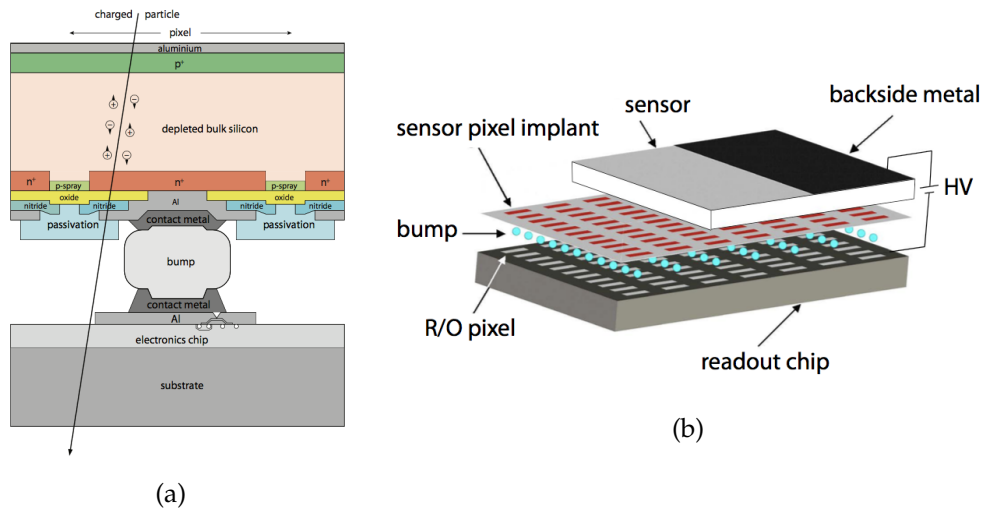


FIGURE 3.7: **a**: Schematic illustration of a single hybrid pixel, including the sensor, the bump bond, and the readout chip. The incoming charged particle is denoted with an arrow. The charge generated by the incoming particle and their motion inside the depletion region are also shown in the graph. **b**: Illustration of a hybrid pixel matrix. The gray box on the top denotes the sensor, and the dark red rectangles are the pixel implants on the bottom of the sensor. A bias high voltage is added between the front and back side of the sensor to fully deplete the sensor bulk. The blue balls are the metal bump bonds. Each sensor pixel and readout pixel are connected with one bump bond. The black gray box on the bottom is the readout chip, and the light gray rectangles on the box are its pixels. Images from [31].

pixels of the IBL planar sensor, and each readout pixel is connected to a corresponding sensor pixel via a bump bond.

When the collected charge enters the readout pixel cell, they first encounter a capacitor, which converts the collected charge to an analog voltage signal through the relationship  $V = Q/C$ , where  $Q$  is the amount of charge, and  $C$  denotes the capacity. Then, the analog signal goes through an amplifier and a discriminator with adjustable threshold, which enables the threshold to be set globally with corrections for each pixel.

As for digitization of the signal, the readout pixel array is subdivided into  $2 \times 2$  pixels regions. The pixels in each region share a common Pixel Digital Region (PDR) which contains the Digital-Analog-Converter (DAC), memory, and trigger processing. The digitization technique is referred to as the "time-over-threshold" method. The analogue voltage pulse can be regarded as a standard-shape curve or a superposition of such curves, and thus by measuring the duration that a pulse stayed above a pre-defined voltage threshold, it is possible to interpolate the amplitude of the pulse. Fig. 3.11 is an illustration of this digitization technique. The measured duration is then converted to a 4-bit digital value. Besides, the pulses are time-stamped using a synchronized timing module. The timing information is converted to a 8-bit digital value. Both the signal and a 8-bit timestamp are stored in memory cells, and are read out after a trigger signal.

### 3.4.2 Monolithic Silicon Radiation Detector

As is mentioned in section 3.4.1, the construction of a hybrid pixel detector is expensive and time-consuming. As a result, alternative pixel fabrication approaches are being explored for the LHC Phase-II Upgrade. One promising candidate is active pixel sensor based on the HV-CMOS technology, a monolithic approach where the

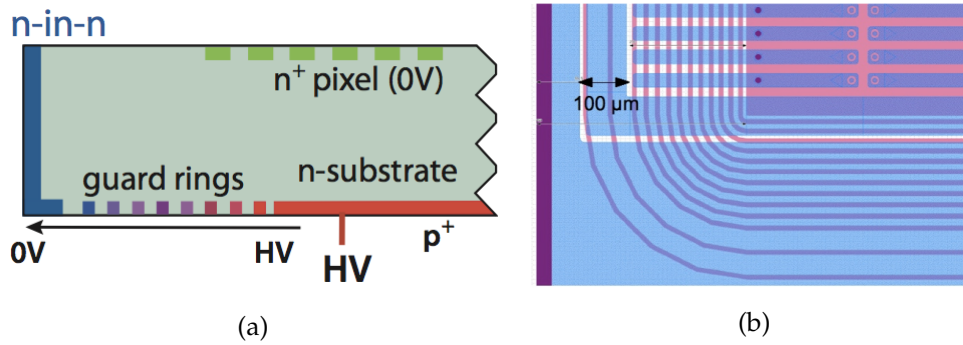


FIGURE 3.8: Schematic drawings of the IBL planar sensor matrix. **a** illustrates the structure of the vertical cross section. This structure is referred to as n-in-in design, as in this design the  $n^+$  pixel implants (green rectangles on the top) are placed on the front side of the n-type substrate. The p-type bias implants for the application of bias high voltage and the p-type guard rings (red and blue rectangles on the bottom) are placed on the back side of the substrate. **b** shows the view from above. The p-type implants and guard rings are drawn in purple, and the n-type pixel implants are drawn in blue. The deep purple dots in the pixel implants are the bump bonds. Notes that n-type and p-type implants are drawn overlapping on this plot, but in reality they are fabricated separately on the front and back side of the substrate. Images from [31] and [16].

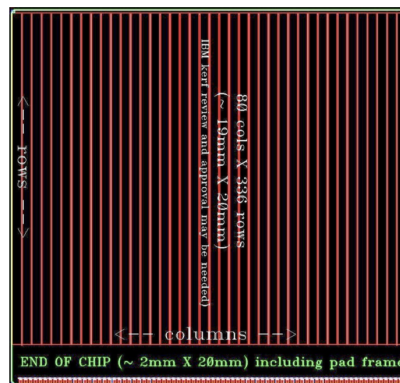


FIGURE 3.9: Outline of the FE-I4 readout chip. The pixel cells are arranged in 80 columns and 336 rows. Image from [16].

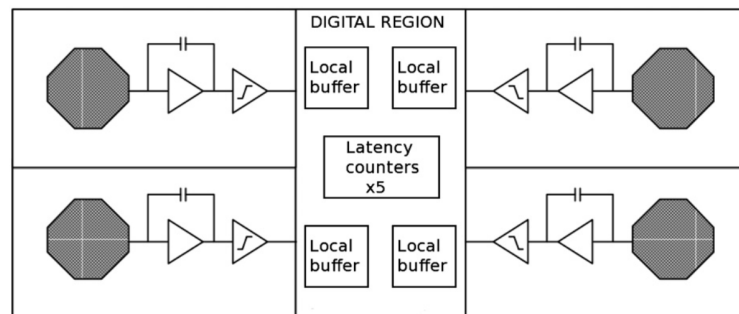


FIGURE 3.10: Diagram of a four-pixel region, showing the geometrical layout of four analog pixel cells and a central digital region. The gray octagons denote the bump bonds. The actual size is  $500 \mu\text{m} \times 100 \mu\text{m}$ . Image from [33].

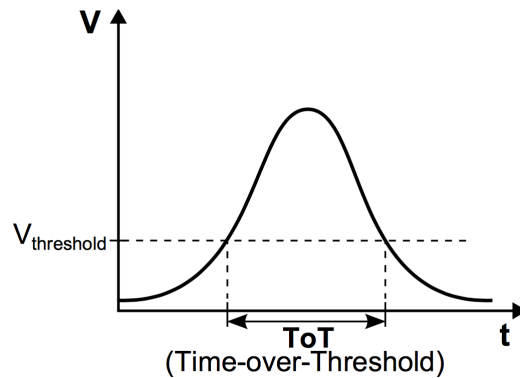


FIGURE 3.11: The time-over-threshold digitization technique. Image from [34].

particle sensor and the readout electronics are fabricated on a single piece of silicon. One of the main advantages of the monolithic approach is that it does not require the laborious and expensive bump bonding process. Besides, in this approach, the bias implant, the guard rings, and the charge collection implants are fabricated on the same side of the substrate, so double-sided processing is not needed. Last but not least, the monolithic approach is an adaptation from commercial CMOS technology, and thus the monolithic sensors are mass-producible. In a word, the monolithic sensors require much less production time and cost.

As is mentioned before, the HV-CMOS technology is an adaptation of commercial CMOS imaging sensor technology to particle detection. The main modifications include additional implant wells to shield the charge collection well and the electronics, and high voltage technology add-ons to optimize the sensor's radiation-hardness and charge collection time. Nowadays, the major commercial CMOS manufacturers are able to make extremely small pixel CMOS imaging sensors ( $< 20 \mu\text{m}^2$  per pixel) with fully depleted charge collection layers and high density CMOS circuitry that can achieve high charge collection speed and efficiency.

At present, the HV-CMOS community within the ATLAS Collaboration is targeting several prototyping designs made by various foundries that provides CMOS technology. One of the most promising prototypes is the ATLASPix design, a fully monolithic CMOS pixel sensor with mature on-chip digital readout architecture fabricated with the 180 nm HV technology provided by ams [35].

The layout of the ATLASPix 1, a first large-scale prototype that contains three matrices of three design variants of similar detecting principles, is shown in Fig. 3.12. Fig. 3.13a and Fig. 3.13b show the top and side views of the ATLASPix Simple matrix, the design that is studied with TCAD simulation in Section 5. The implant wells in a ATLASPix pixel include a dense n well and a p well that are constituents of the standard CMOS architecture. The n well serves as the charge collection well, while the readout electronics are fabricated in the p well. Besides, an additional deep n well with lower doping concentration is implanted surrounding the p well and n well for shielding purpose, and a p-guard ring is placed on the periphery for the application of high bias voltage. As is illustrated in Fig. 3.13b, after a reverse bias voltage is applied on the p guard ring, a wide depletion region is created inside the substrate. When a particle hits the pixel, electron-hole pairs are created along the track. The generated electrons inside the depleted region flow toward the n well to be collected, and the generated charge carriers in the undepleted part of the bulk diffuse randomly until they diffuse into the depletion zone or get trapped at some defect site.



FIGURE 3.12: Layout of the ATLASPix 1 prototype consisting of three matrices of design variants including the ATLASPix M2, the ATLASPix Simple, and the ATLASPix IsoSimple. Image from [37].

The charge collected by the n well is then passed to the electronics in the p well, where they will be amplified, selected, and transformed to digital signals in a similar process as described in section 3.4.1.

### 3.5 Summary

Silicon semiconductor is widely used for particle sensors because their electric properties can be easily manipulated by doping with an exact amount of impurities. When a piece of p-type silicon semiconductor is placed next to the n-type semiconductor, a p-n junction and then a depletion zone, a space-charge area with an electric field and without free charge, are formed. The depletion zone can be used for particle detection.

When a charged particle goes through a depletion zone, it deposits energy which injects free charge to the depletion zone. The free charge moves under the electric field inside the depletion zone, and if an electrode is placed on the p-n junction, the movement of free charge will induce a current signal on the electrode. The current signal is then transferred to the readout circuit, where it will be processed and converted to digital signal, thus making particle detection possible. The width of the depletion zone, i.e., the sensitive detection area, can be widened by the application of an external voltage. Beside charge injection, the interaction of charged particle with the semiconductor may also result in the displacement of lattice atoms. This is called radiation damage, a harmful effect which results in smaller depletion width, increase of noise, and reduction of signal strength.

There are two approaches of sensor fabrication, namely, the hybrid approach where the sensing part and the readout circuit is fabricated on separate chips and connected through bump bonding, and the monolithic approach where the sensing part and the readout circuit are fabricated on a single piece of silicon. These two approaches have been introduced in section 3.4.1 and 3.4.2 using the ATLAS IBL planar sensor and the ATLASPix 1 as examples.

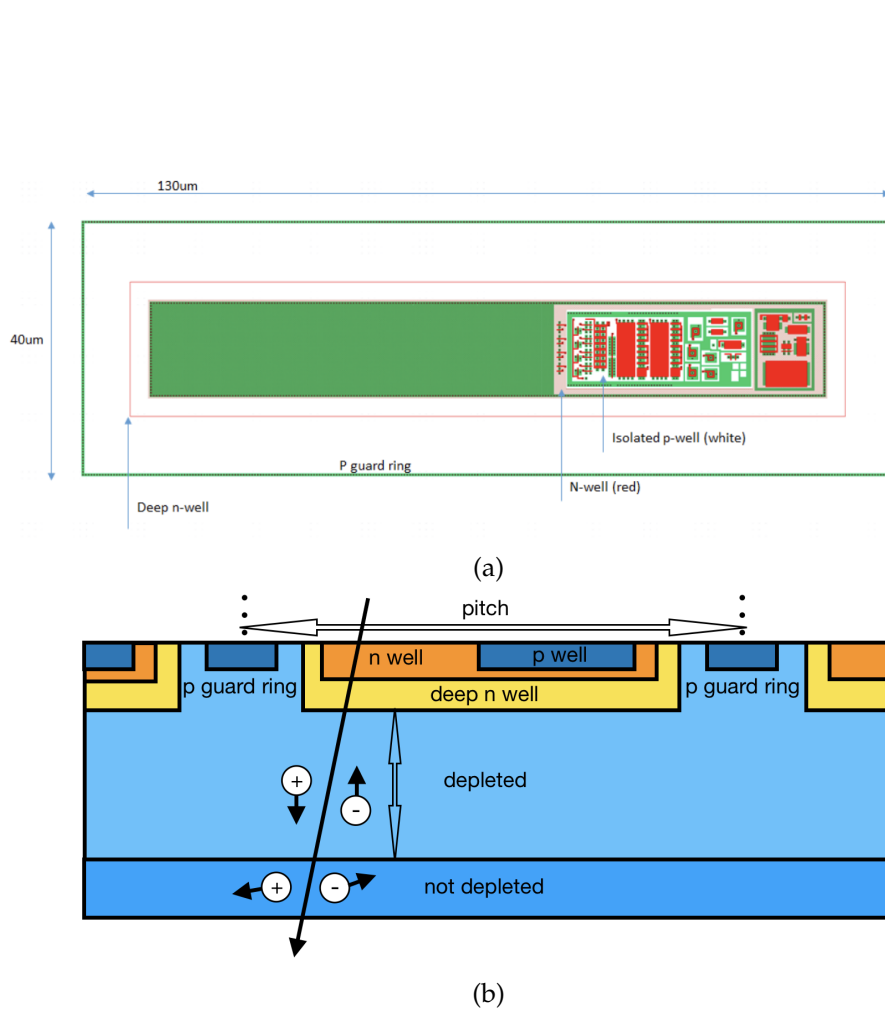


FIGURE 3.13: Layout of a ATLASPix Simple matrix pixel. **a** shows the top view of the pixel, with p guard rings (green lines on the peripheral), deep n well (region inside the pink rectangle), n well (green and pink regions), and p well (white region inside the n well). The bias high voltage is applied on the p guard ring, and the readout electronics are placed in the p well. Picture is drawn to scale. **b** is the vertical cross section of the pixel. The incoming particle track is represented by an arrow. Inside the depletion region, the generated electrons flow to the n well, while the holes flow to the back side of the sensor. Outside the depletion region, the generated charge carriers diffuse randomly. Some of the electrons may diffuse into the depletion region and get collected. Picture not drawn to scale. Image from [37].



## Chapter 4

# Simulation of FE-I4 Telescope

The testbeam experiment is a crucial step in the R&D of tracking detectors. Computer simulation is often employed to aid the analysis and interpretation of testbeam results. A valid simulation model of the FE-I4 telescope, the measurement device used in the testbeam simulations by the ATLAS group of the University of Geneva, has been built with the Allpix<sup>2</sup> [38] simulation framework. Computer experiments with upright and inclined telescope planes have been done to probe the effects of geometry on the spatial resolution of the telescope. The simulation results provided explanations on why better resolution is achieved with inclined geometry. In addition, the model can be used in future research about improvement of resolution by more advanced reconstruction algorithms. It can also be extended to simulate different beam telescopes or experiment under different conditions. In this chapter, the simulation and its validation are presented. In addition, the performance of the reconstruction framework Proteus [36] on inclined planes has been evaluated.

### 4.1 Testbeam Experiment

In testbeam experiments, high energy particle beams are used to test the performance of prototype detectors. Beam telescopes are commonly adopted in testbeam experiments to record particle tracks and to measure the behavior of the prototype. A typical beam telescope is a small tracking detector. It consists of several telescope planes with well-known sensors and readout chips, and one or more planes to install the prototype sensor, called the Device-Under-Test (DUT). During data-taking, the DUT plane is carefully aligned with other telescope planes. By comparing particle hits on the DUT with tracks reconstructed from the telescope sensors, information can be obtained about important characteristics of the DUT, including spatial and temporal resolution and efficiency.

### 4.2 The FE-I4 Telescope

#### 4.2.1 Telescope Description

The FE-I4 telescope [32] is a powerful beam telescope constructed in 2014 and is since then employed by the Geneva group in testbeam experiments. It is able to test prototypes of up to 4 cm<sup>2</sup> area with event trigger rate of  $\sim$ kHz and beam-tracking of  $\sim$ 10  $\mu$ m precision at the DUT [32].

The telescope is composed of 6 telescope planes and a DUT box inside which the temperature is controlled. It has two arms, each holding three adjustable telescope planes, and the DUT box in the middle. Each telescope plane has a 200  $\mu$ m thick

IBL planar silicon sensor [16]. Fig. 4.1 shows a computer generated image of the telescope [32].

Readout of the telescope plane sensors is provided by ATLAS FE-I4 frontend chips [33]. Each sensor has two FE-I4 chips, but only one chip is read out during data-taking. The reason is that, in the experiments, the two mid-planes on each arm are flipped by  $90^\circ$  around the beam axis to ensure similar resolution in  $x$  and  $y$  direction. As a result, only one of the two FE-I4 chips on each plane can remain overlapping. The overlapping chips are read out.

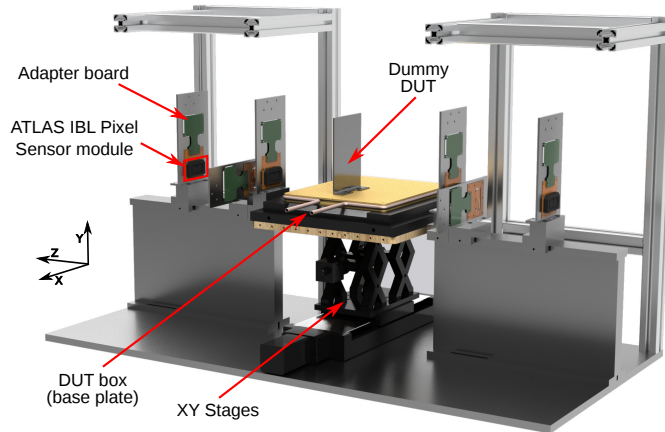


FIGURE 4.1: Computer generated image of the FE-I4 telescope. Shown in the image are two arms, each with 3 telescope planes, and a dummy DUT in the middle. Image from [32].

## 4.2.2 Reconstruction

The raw data taken by the telescope are reconstructed with Proteus [36], a software to reconstruct and analyze data from pixel beam telescopes based on C++ and ROOT. The reconstruction proceeds through multiple steps.

**Noise masking.** Preprocessing includes masking noisy pixels.

**Clustering.** When a particle hits a telescope plane, it can trigger more than one pixels. Proteus implements an algorithm to group all neighboring hits into a cluster. The position of the cluster is by default estimated as the geometric mean of the pixel positions weighted by the amount of deposited charge in each of the pixels.

**Track finding.** The tracking algorithm starts with a seed cluster, and then searches for following clusters inside a cone determined by the scattering angle of the particle and the beam divergence on the planes. The algorithm assumes initially that the track is parallel to the plane's longitudinal axis, and modifies the direction of the track when clusters are added. If multiple candidates are found on one plane, the track divides and searches continue at each node. The candidate tracks with the largest number of clusters are kept. Clusters that have been assigned to tracks are excluded from further searches.

**Track fitting.** The tracks are fitted to a straight line. Tracks with large  $\chi^2$  are excluded for they are likely to have undergone heavy scattering or nuclear interaction with the telescope planes or are not real tracks.

**Alignment.** To reconstruct particle tracks with high precision, it is necessary to obtain the accurate relative position of the telescope planes. The alignment algorithm takes as input the telescope geometry manually measured during the experiment, then adds small corrections to offsets and inclination angles of the planes to obtain optimal inter-plane hit correlation distribution and track residuals.

The last three steps are repeated until an optimal reconstruction of tracks is found.

### 4.3 Data Sample

A data sample with over 1 million triggers was used to extract simulation parameters and to validate the simulation model. It was taken in a testbeam experiment at H8 beamline in the CERN SPS testbeam facility with 180MeV  $\pi^+$  beam. During data-taking, the telescope planes were inclined by an angle of around  $12.5^\circ$ , and the two mid-planes on each arm were additionally flipped by  $90^\circ$  horizontally. The telescope planes were separated by a distance of roughly 10 cm, and the DUT plane was 10 cm away from the last plane on the left arm, and 35 cm away from the first plane on the right arm. The geometry parameters have been reconstructed using the Proteus reconstruction package and used as input for the AllPix<sup>2</sup> simulation. Fig. 4.2a is a photo of the telescope in the same geometry as during data taking. The temperature of the sensors was kept at  $30^\circ\text{C}$ .

### 4.4 Simulation of the FE-I4 Telescope

The simulation model is created with Allpix<sup>2</sup> [38], a generic simulation framework for silicon tracker and vertex detectors written in C++. A full simulation consists of the following steps:

**Geometry construction** A set of detectors, such as a beam telescope, are built with the GEANT4 geometry modeler. Every detector is described by position, orientation, and detector model parameters. The detector model contains parameters describing the geometry of the sensor and the support of the detector. The sensor parameters include type, namely monolithic or hybrid, number of pixels, pixel size, thickness of the sensor, and thickness of the readout chips on the sensor. The parameters of the supporting structure include size, thickness, location, and the type of materials.

**Charge deposition** Simulation of the particle beam and of the deposition of charge carriers inside the sensor as charged particles traverse the active area of the sensors. The interaction of the particle with the sensor is modeled with the FTFP\_BERT\_LIV physics list provided by GEANT4 [39]. The position and direction of the particle beam can be specified to the scale of mm, and the divergence to the scale of mrad [40].

**Charge propagation** Simulation of the propagation of charge carriers through the silicon sensor due to drift or diffusion processes. The final position of the propagated charge is stored. If the charge is ready to be collected, its position is on the pixel implant. The charge can also be outside the pixel implant if it got trapped inside the sensor bulk or if it was lost in another process.

**Assignment of charge to pixels** In this step, the deposited and propagated charges in the sensor are assigned to pixels of the readout electronics. The indices of triggered pixels and the number of charges at each pixel are stored.

**Digitization of charge** Conversion of charge at the pixels to ADC (Analog-to-Digital-Converter) units. The charges above threshold are converted to digitized signals. In the simulation presented in this chapter, they are converted to 16 ADC units based on a linear scale, to best emulate the real case.

The output of the simulation is stored in ROOT format.

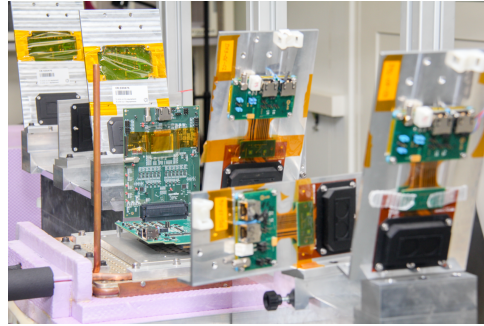
In the simulation, the FE-I4 telescope has been reproduced. A visualization of the simulation is shown in Fig. 4.2b. Six telescope planes have been simulated, and each of them is equipped with a 200  $\mu\text{m}$  thick IBL planar pixel silicon sensor, which consists of 330 columns and 80 rows of 250  $\mu\text{m}$  long and 50  $\mu\text{m}$  wide pixels. The two arms holding the telescope planes have not been simulated since they are not in the beam during data taking. A sensor in the middle to represent the DUT has also been simulated, but has not been considered in the analysis.

The inclination angles and offsets of the telescope planes were obtained from the reconstruction of the geometry in the data sample. The two mid-planes on each arm were rotated by  $90^\circ$  around the beam axis to ensure similar resolution in  $x$  and  $y$  direction. In addition, the three planes on the left were inclined by  $12.5^\circ$  to the upstream direction, and the three planes on the right were inclined by the same angle towards downstream direction. The DUT plane remained upright. The telescope planes were perfectly aligned. The three upstream planes were separated by 10 cm from each other, and so were the three downstream planes. The distance between the two planes next to the DUT plane was about 45cm. The DUT plane was about 30cm away from the closest plane on its left. Details of the position of the telescope planes are shown in Table A.1a and A.1b in Appendix A. The simulated planes were reflected along its longitudinal axis, but this reflection would not influence the results since all chips are symmetric along its long axis.

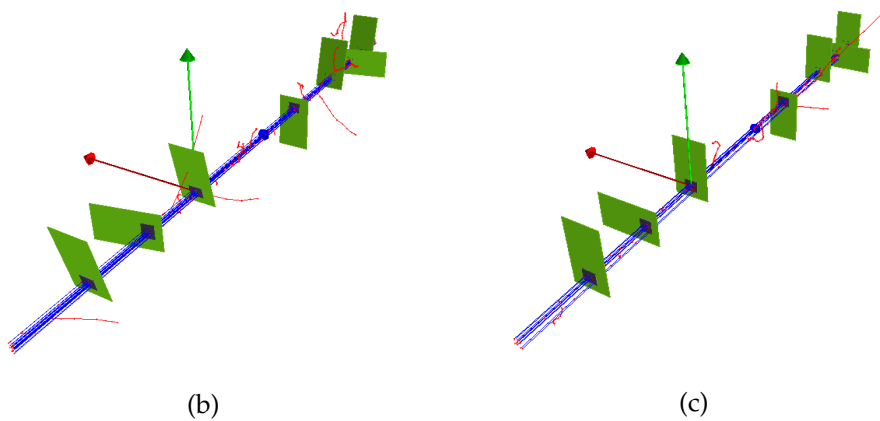
The simulated beam consisted of 180MeV  $\pi^+$ . Beam size, direction, and divergence were those obtained from the data sample. The simulated temperature for charge propagation in the sensors was  $30^\circ\text{C}$ .

As for the digitizer, in the simulation, the charge deposition in the pixels above a threshold of 3000e was kept and converted linearly to 4-bit ADC units that ranges from 1 to 15, and 15 is the overflow bin. However, the testbeam data above threshold were encoded in units from 1 to 14 and 14 was the overflow bin, and the conversion scale differs slightly from a linear relationship. Thus it was not possible to simulate the same digitization with currently available simulation tools. Digitizer parameters including ADC slope and ADC offset have been tuned to make simulation as close to data as possible.

The simulation parameters are summarized in Table A.1 in Appendix A. The simulation model with the parameters described above is referred to as "inclined model" in the following text. In addition, another model with the same parameters but with upright telescope planes (referred to as "upright model") was built, to compare the performance of the reconstruction framework on the inclined and the upright geometry, because the upright geometry was the original construction of the telescope before the inclined geometry was adopted in 2017.



(a)



(b)

(c)

FIGURE 4.2: **a**: Photo of the FE-I4 telescope in UniGE cleanroom. The geometry of telescope planes and the DUT is the same as that in the experiment where the data sample was taken. **b**: Visualization of the inclined simulation model of the FE-I4 telescope. **c**: Visualization of the upright simulation model. This model has been built for the evaluation of reconstruction in section 4.6.

## 4.5 Validation of the Simulation

The simulation and the data sample have been reconstructed with Proteus through the processes described in section 4.2.2. Three variables that serve as direct input for reconstruction have been checked to evaluate the validity of simulation. They include

1. the cluster size, the number of neighboring pixels with a signal above threshold;
2. the cluster value, the number of ADC units of a cluster;
3. the hit value, the number of ADC units of each hit.

Fig. 4.3, 4.4, and 4.5 show the distribution of the three variables in simulation and in data. The cluster size distributions agree well. The number of size 1 clusters and size 2 clusters are almost the same, and they account for over 98% of clusters. Due to the limits in the digitization model, the simulated cluster value and hit value differ slightly from data. The deficit in low value clusters in simulation is caused by the fact that in the simulated digitizer the amount of deposited charge is converted linearly to ADC units, but in the experiment, the function of conversion varies slightly from the linear scale. The difference does not make a big difference, as the agreement of

the cluster value distributions from the simulation and the data is sufficient. The excess in bin 15 and bin 30 in the simulated cluster size distribution is due to the fact that the 15th and the 30th bins are used as the overflow bin. The difference in hit value in simulation and the data is the most obvious among the three variables, because the difference in digitizer mentioned in Section 4.4 renders it impossible to emulate exactly the experiment. Nevertheless, simulation parameters have been tuned to achieve a relatively good level of agreement. Overall, it is safe to conclude that the simulation is valid enough to be used to study the effect of geometry on the resolution of the telescope.

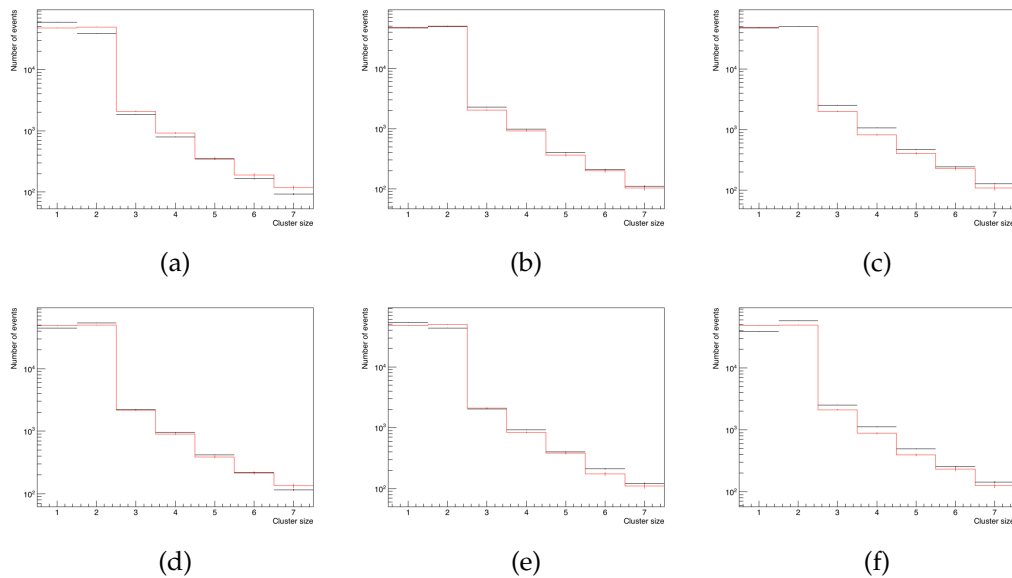


FIGURE 4.3: **a – f**: Distribution of cluster size in the simulated inclined model (red) vs. data (black) on telescope planes 1 – 6.

## 4.6 Evaluation of Reconstruction

The performance of the reconstruction with Proteus [36] of particle tracks through the inclined telescope planes was studied using the simulation model presented above. The performance was evaluated with the residual between the reconstructed cluster position on the telescope planes and the truth particle position on the same plane read from the simulation. In addition, another simulation model with upright telescope planes was generated to study the difference between the reconstruction of inclined and of upright telescope planes. Fig. 4.2c is the visualization of the upright model. The upright model has the same beam, digitizer, and temperature settings. Six FE-I4 telescope planes each holding an ATLAS IBL planar sensor and a DUT plane were simulated and they were separated by the same distance from each other as in the inclined model. Similar to the inclined model, the mid-planes on left and right arm were rotated by  $90^\circ$  around the beam axis. The only difference was that the telescope planes were upright.

For simplicity, only the first telescope plane in both simulation models was considered in the analysis. Fig. 4.6 shows the distribution of the positions of reconstructed clusters and of truth particles on the first telescope plane for inclined and upright model.

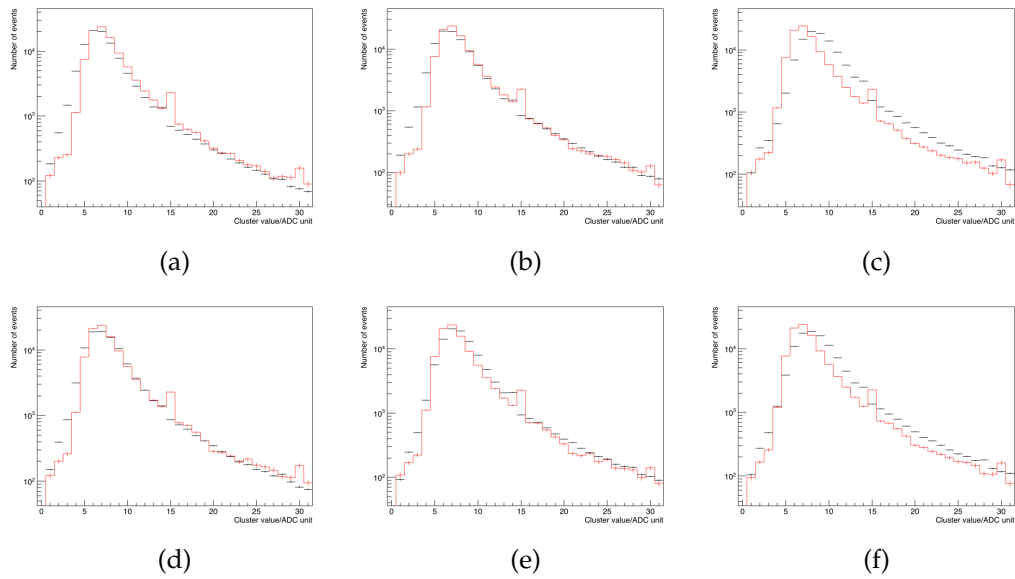
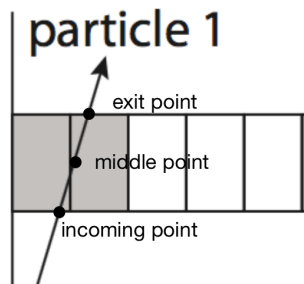


FIGURE 4.4: **a – f**: Distribution of cluster value in the simulated inclined model (red) vs. data (black) on telescope planes 1 – 6. The excess in bin 15 and bin 30 in the simulation is caused by the fact that these two bins are used as the overflow bin.

The residual between cluster position and truth particle position is calculated using Eq. 4.1. It is calculated as the difference between the column/row number of cluster on the sensor on one telescope plane and the  $x/y$  coordinate of the middle-point on truth particle's track through the same sensor.

$$\begin{aligned}
 \text{Res}_x &= \text{column}_{\text{cluster}} - x_{\text{middle-point}} \\
 \text{Res}_y &= \text{row}_{\text{cluster}} - y_{\text{middle-point}}
 \end{aligned} \tag{4.1}$$

where  $x_{\text{middle-point}}$  or  $y_{\text{middle-point}} = \frac{x \text{ or } y_{\text{income}} + x \text{ or } y_{\text{exit}}}{2}$



Demonstration of points on the particle track. Image from [31].

Fig. 4.7a and 4.7b show the distribution of  $x$  and  $y$  residuals between cluster position and truth position in the inclined and upright models. The  $x$  residuals in the inclined and the upright model are similar. They are almost uniformly distributed between  $-140$  and  $140 \mu\text{m}$ . But the  $y$  residuals are different. While the  $y$  residual in the upright model is closer to a uniform distribution from  $-30$  to  $30 \mu\text{m}$ , the  $y$  residual in the inclined model is of a Gaussian shape. The  $y$  residuals in the inclined model are better than those in the upright model, indicating a better reconstruction of cluster position in the inclined model, which translates to better tracking.

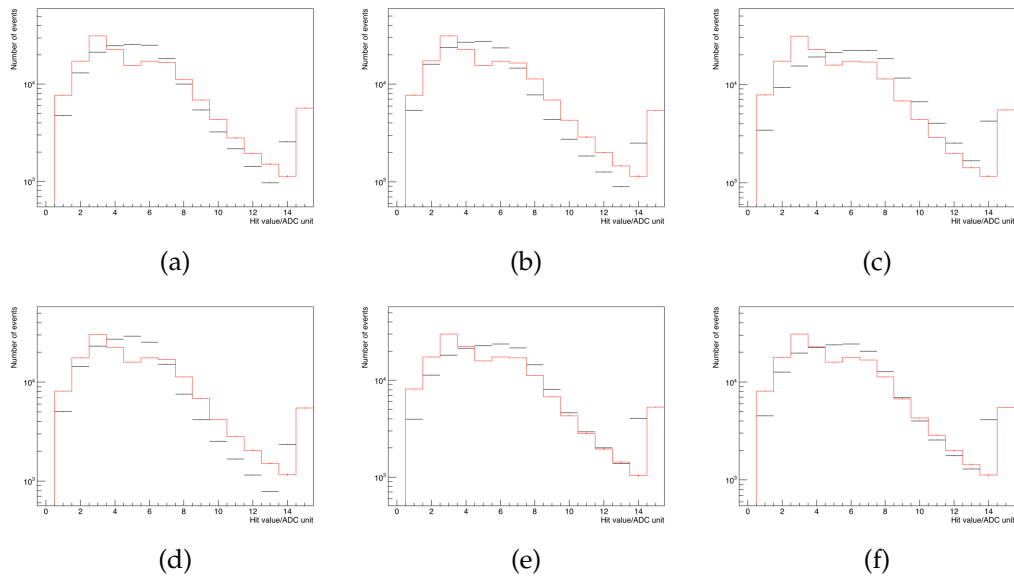


FIGURE 4.5: **a – f**: Distribution of hit value in the simulated inclined model (red) vs. data (black) on telescope planes 1 – 6.

The  $y$  residuals for clusters of each size in inclined and upright model have also been studied. Only clusters of size 1 and 2 have been considered because, as is indicated by Fig. 4.3, size 1 and size 2 clusters make up of more than 98% of clusters. The distribution of  $y$  residuals for size 1 and size 2 is shown in Fig. 4.8a (inclined model) and 4.8b (upright model). For both inclined and upright models, the residual of size 2 cluster is smaller than that of size 1 cluster. In the upright model, the residual distribution of size 2 cluster is of a saddle shape. Further studies are needed to understand this shape.

Fig. 4.9 shows the map of truth particle positions on the first telescope plane on a  $2 \times 2$  matrix of pixels for inclined and upright geometry, respectively. It is obtained by mapping the truth particle hits on all pixels on the sensor to the  $2 \times 2$  pixel matrix on the lower-left edge. Fig. 4.10 shows the map of cluster positions obtained in the same way. When the particle track is close enough to the edge of the pixel, the charge cloud it generates drifts to two adjacent pixels and will result in triggering two pixels. In the upright model, size 2 clusters are formed when the particle track is less than  $5 \mu\text{m}$  away from the edge, while in the inclined model, the mid point of the particle track only needs to be within  $25 \mu\text{m}$  from the pixel edge to lead to size 2 clusters. Thus, in the inclined model, the area where a particle triggers two pixels is enlarged, resulting in an obvious increase in the number of size 2 clusters. Since the position reconstruction of size 2 clusters is better than that of size 1 clusters, as is shown in the simulation results, the reconstruction of cluster position in the inclined model is better, and this could lead to a better telescope resolution when the telescope planes are inclined. This also explains why the improvement of the resolution in the  $y$  direction is more obvious than that in the  $x$  direction. The pixel pitch in  $y$  is  $50 \mu\text{m}$ , which is  $1/5$  of the pixel pitch in  $x$ . As can be seen in Fig. 4.9, in the inclined model, the area where a particle hit leads to a size 2 cluster in the  $y$  direction accounts for  $1/2$  of the total pixel area, while in the upright model this area only makes up  $1/5$  of the total area. Therefore, the inclination of the telescope planes leads to a noticeable increase in the proportion of size 2 clusters in  $y$  direction. However, compared to the pixel pitch of  $250 \mu\text{m}$  in the  $x$  direction, this increase of

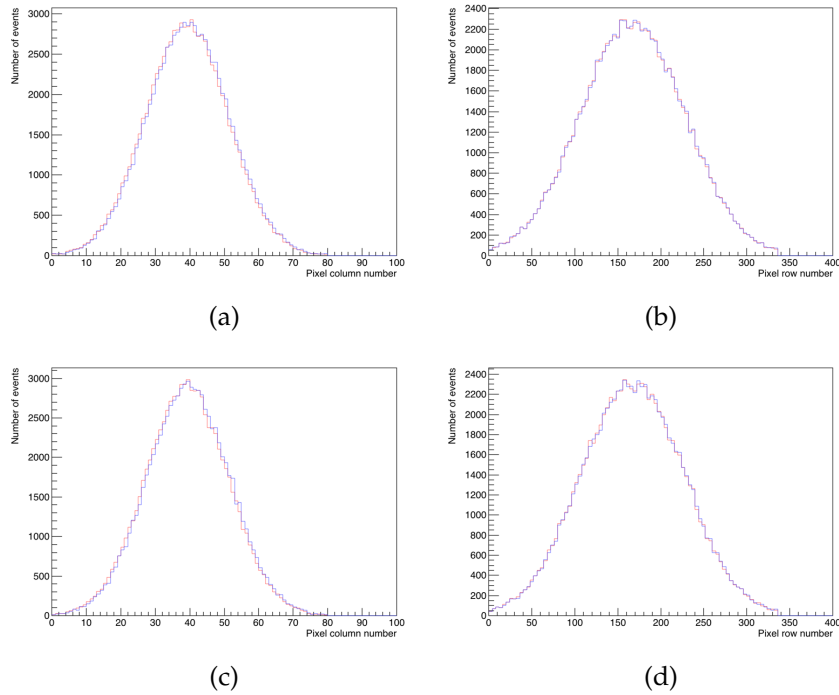


FIGURE 4.6: **a** and **b**: Distribution of  $x$  (**a**) and  $y$  (**b**) positions for truth particles (red) and reconstructed clusters (blue) in the inclined model. **c** and **d**: Distribution of  $x$  (**c**) and  $y$  (**d**) positions for truth particles (red) and reconstructed clusters (blue) in the upright model. Note that the  $x$  coordinate denotes the row or column number of the pixels.

$20 \mu\text{m}$  in the area that allows size 2 cluster is not obvious, and the proportion of the size 2 clusters in the  $x$  direction does not change much. Thus the reconstruction resolution in the  $y$  direction is more sensitive to changes in geometry.

## 4.7 Summary

Simulations of the FE-I4 telescope with inclined and upright geometry were made with AllPix<sup>2</sup>, and validated with the data sample taken during a testbeam experiment at CERN SPS with 180 MeV  $\pi^+$  beam. Besides, the performance of the Proteus reconstruction framework on the inclined and upright models was compared. The reconstruction resolution in the inclined model is better than that in the upright model, indicating that indeed with the inclined geometry, the resolution of the telescope is improved. The explanation is that the increase of size 2 clusters in the inclined model has led to this improvement of the resolution.

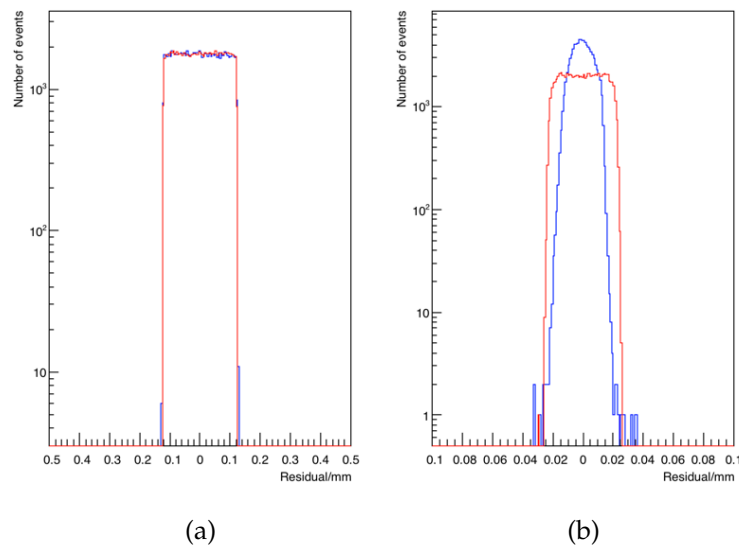


FIGURE 4.7: Distribution of the residuals between the x (a) and y (b) positions of reconstructed clusters and truth particles in the inclined and upright model. The blue lines show the inclined model and red lines show the upright model.

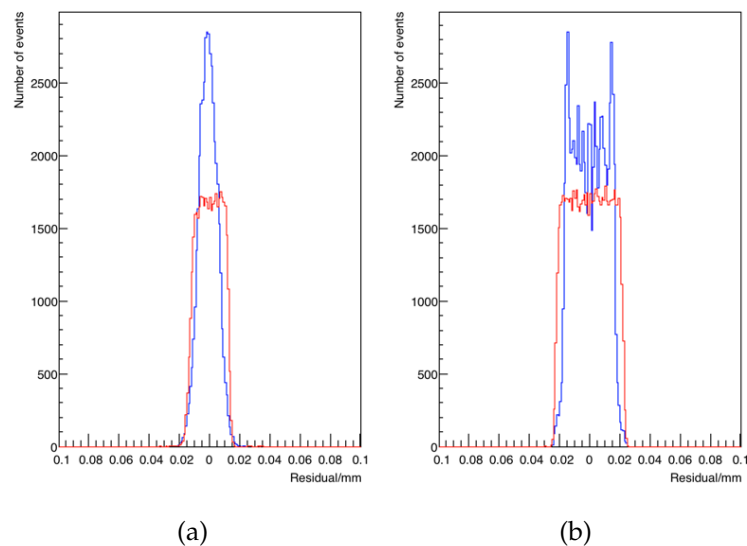


FIGURE 4.8: Residual between y positions of reconstructed clusters and truth particles for size 1 and 2 clusters in the inclined (a) and upright (b) model. The red lines show the residual for size 1 clusters and the blue lines show that for size 2 clusters.

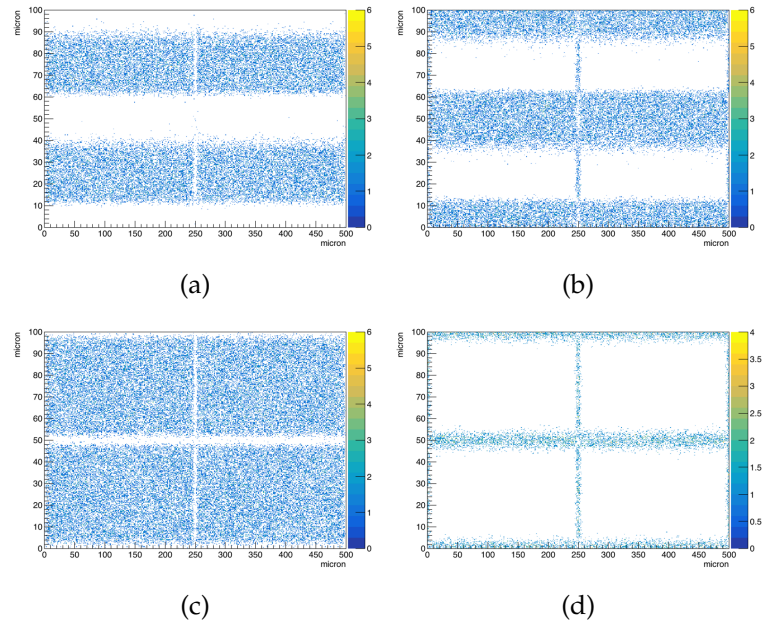


FIGURE 4.9: **a** and **b**: Distribution of truth particle positions for clusters of size 1 (**a**) and 2 (**b**) mapped to a  $2 \times 2$  pixel matrix in the inclined model. **c** and **d**: Distribution of truth particle positions for clusters of size 1 (**c**) and 2 (**d**) mapped to a  $2 \times 2$  pixel matrix in the upright model.

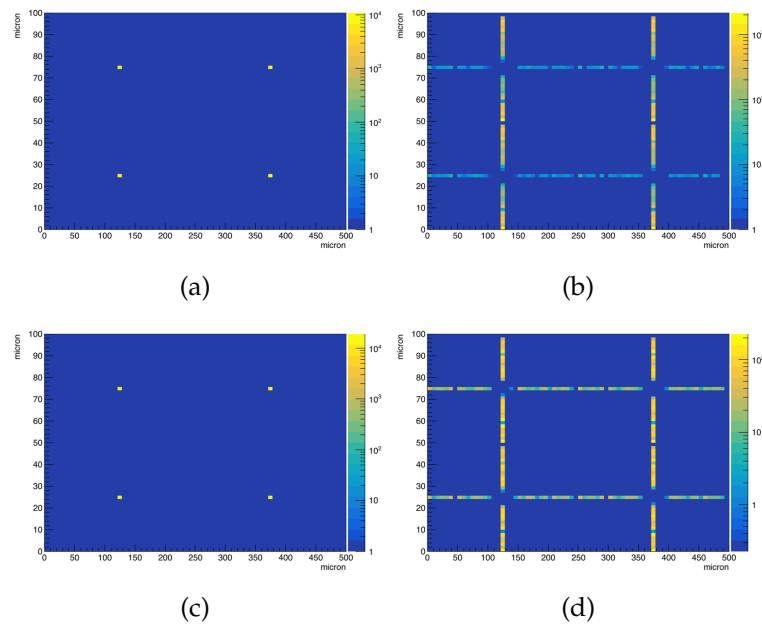


FIGURE 4.10: **a** and **b**: Distribution of reconstructed cluster positions clusters of size 1 (**a**) and 2 (**b**) mapped to a  $2 \times 2$  pixel matrix in the inclined model. **c** and **d**: Distribution of reconstructed cluster positions of clusters of size 1 (**c**) and 2 (**d**) mapped to a  $2 \times 2$  pixel matrix in the upright model.



## Chapter 5

# TCAD Simulation of ATLASPix

The physics goals and the design requirements of LHC phase-II upgrade pose a stringent demand on the resolution, radiation hardness, and production cost on the ATLAS ITk pixel detector. The ATLASPix fabricated using the HV-CMOS technology provided by ams [35] is a fully monolithic sensor candidate under study for the outermost pixel layers of the ITk detector. To aid the development of the ATLASPix, simulation of the ATLASPix Simple matrix on the ATLASPix 1, the first large-scale fully monolithic prototype, was performed with the Technology Computer Aided Design (TCAD) software provided by Synopsis [41] in order to understand the signal formation and collection processes in the sensor. In this chapter, 2D and 3D TCAD simulation results of the ATLASPix Simple pixels will be presented, including electrical properties, response to transient incoming particle, and the charge collection. Models of four different values of bulk resistivity were simulated and compared to study the influence of bulk resistivity on sensor behavior.

### 5.1 Technology Computer Aided Design

TCAD refers to the use of computer simulation in the design process of semiconductor devices. It includes process TCAD, the modeling of the fabrication process, and device TCAD, the simulation of the device operation. TCAD reached its maturity in the mid 1980s, and has remained an essential design tool [42]. By numerically solving the fundamental physical partial differential equations such as the drift-diffusion equation, TCAD software can model the structural properties and electrical behaviors of semiconductor devices. Thus, at early design stages, TCAD allows the exploration of alternative structure designs and the impact of structure on physical performances when experimental data are not available. Besides, in the optimization of fabrication process, TCAD makes it possible to conduct experiments on a broad range of process variables to comprehensively study the fabrication process without the costly and time-consuming experimental runs on real wafers [43].

The TCAD results presented in this thesis are obtained with software provided by Synopsis, one of the major suppliers of commercial TCAD tools [41]. The simulation with the Synopsis software is done in the following 3 steps.

1. Generation of Device Structure.

The first step is to create a geometric structure that contains information of the geometric layout and doping profiles for each region of the device as the input of TCAD. This is done with the Sentaurus Device Editor, a structure editor based on the Scheme scripting language. In addition, this structure editor provides a mesher that divides the structure into small regions, referred to as mesh

elements, on which is obtained the numerical estimation of physical properties such as the distribution of the electric field [44].

## 2. Process TCAD.

The major process TCAD tool provided by Synopsis is the Sentaurus Process. This tool takes as input the structure generated by the structure editor, and parameters such as temperature and pressure. It then uses powerful numerical algorithms to simulate the fabrication steps of the device, such as doping, diffusion of carriers, etc. Besides, with Sentaurus Process, one can specify certain interfacial region to be contacts, where the subsequent tools such as the Sentaurus Device apply electrical boundary conditions. Another useful feature of the Sentaurus Process is that it allows the creation of multi-pixel structure by reflecting the input structure. The output of process simulation is a 2D or 3D structure that can be used as input to device TCAD [45].

## 3. Device TCAD.

The main Device simulation tool is called the Sentaurus Device. It simulates the electrical behavior of the semiconductor for a given set of boundary conditions such as bias voltage or current flux, by solving a set of physical equations that describes the carrier distribution and conduction mechanisms. The input can be structures generated by both the Sentaurus Device Editor or the Sentaurus Process [46].

## 5.2 Model of Single Pixel

A full-flow TCAD simulation is often accomplished with simplified 2D models, as a 2D simulation is finished within hours while a full 3D model can take days or weeks. A 2D model is generated by simulating a cross section of the device and assuming the device is uniform in the third dimension. Full 3D models and simplified 2D models emulating a single ATLASPix Simple Matrix pixel of bulk resistivity of 20, 80, 200, and 1000  $\Omega\cdot\text{cm}$  have been built, to study the influence of the 2D simplification on the electrical properties of the sensor, and to compare the behavior and performance of pixels of various bulk resistivity values. In this section, the simulated structures and the results including the electrostatic potential, depletion zone, electric field, and response to particles will be presented. Besides, a 2D simulation of a matrix of four pixels has also been made to study the charge-sharing and edge effects of neighboring pixels, and the results will be included in the next section.

### 5.2.1 Simulated Structure

To begin with, a full 3D simulation of the ATLASPix 1 pixel has been built. The model is 130  $\mu\text{m}$  in length, 40  $\mu\text{m}$  in width, and 100  $\mu\text{m}$  in thickness. The location and sizes of the implant wells on the front side are specified according to Fig. 5.1. A p-type guard ring (referred to as p-guard ring hereafter) that is 5  $\mu\text{m}$  wide and 1  $\mu\text{m}$  deep is placed at the periphery of the front side of the pixel, and is implanted with boron of a concentration of  $1 \times 10^{16} \text{ cm}^{-3}$ . The p-guard ring serves both as guard ring and bias voltage implant. Besides, a 6  $\mu\text{m}$  deep n-type well (referred to as deep n-well) is placed inside the area surrounded by the p-guard ring. A denser n-type well (referred to as n-well) with a depth of 2  $\mu\text{m}$  is further placed inside the deep n-well. Finally, a 1  $\mu\text{m}$  deep p-type well (referred to as p-well) is placed inside the n-well. The n-type wells are doped with phosphorus, with a dopant concentration of  $1 \times 10^{16}$

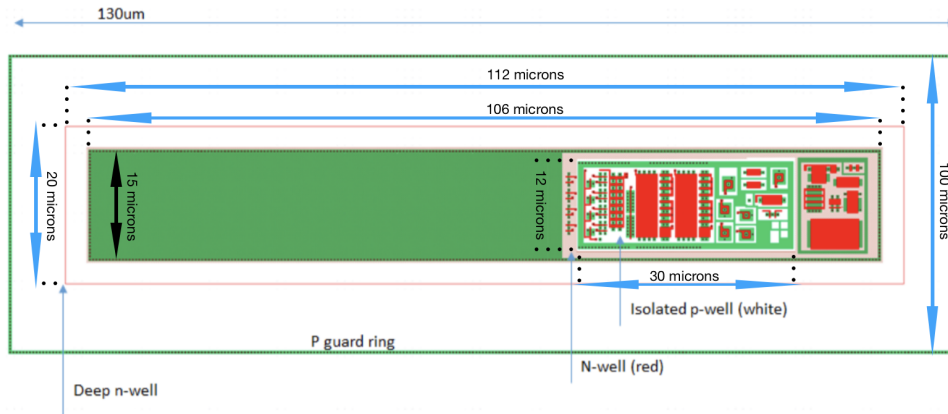


FIGURE 5.1: Schematic drawing of the top view of the ATLASPix Simple pixel, showing position and size of the front-side of the bulk and the implants including the p-guard ring, deep n-well, n-well, and the p-well. Image from [37].

$\text{cm}^{-3}$  for the deep n-well, and of  $1 \times 10^{18} \text{ cm}^{-3}$  for the n-well. The p-well is doped with boron with a concentration of  $1 \times 10^{18} \text{ cm}^{-3}$ . As is mentioned in Section 3.4.2, the deep n-well shields the n-well and p-well, the n-well is responsible for charge collection, and the readout circuit is implanted in the p-well. In addition, two oxide layers are added to the front and back sides of the pixel, to protect the bulk and the implant wells. The bulk is of p-type, and is doped with a chosen amount of boron to tune the bulk resistivity. Four models of bulk resistivity of 20, 80, 200, and  $1000 \Omega \cdot \text{cm}$  have been simulated to study the influence of bulk resistivity on sensor performance. Details about the size and doping concentration of the bulk and implant wells can be found in Table B.1 in Appendix B.

Besides the full 3D models, simplified 2D models of the same values of bulk resistivity have been made. The simulated plane is the vertical cross section through the center of the sensor. It also has a length of  $130 \mu\text{m}$  and a depth of  $100 \mu\text{m}$ , but it is assumed to be uniform in the third direction with a width of  $1 \mu\text{m}$ . The location, length, and depth of the implant wells are the same as those in the 3D model, except that they are also reduced to 2D.

Six electrodes have been added on the front side, with two on the p-guard ring, two on the p-well, and two on the n-type wells, for the specification the electrical boundary conditions at the implants and reading their responses to incoming particles in the device simulation. Two additional electrodes are added on the backside to tune the electrostatic potential at the bulk.

The geometrical layouts with doping concentration of the the models of four resistivities are shown in Fig. 5.2, 5.3, 5.4, and 5.5.

## 5.2.2 Simulation of Device Operations

### Electrical Properties

The behavior of the simulated pixels under a reverse bias voltage of  $-60 \text{ V}$  on the p guard ring and the bulk,  $1.8 \text{ V}$  on the n-type wells, and  $1.0 \text{ V}$  on the p well has been simulated and analyzed. The distribution of the electrostatic potential and the electric field inside the device as well as the position and size of the depletion zone have been obtained by solving the Poisson equation Eq. 3.16 using the external voltages specified above as boundary conditions (See Section 3.3). The Sentaurus Device tool provides a variety of physics models to describe the physics processes inside the

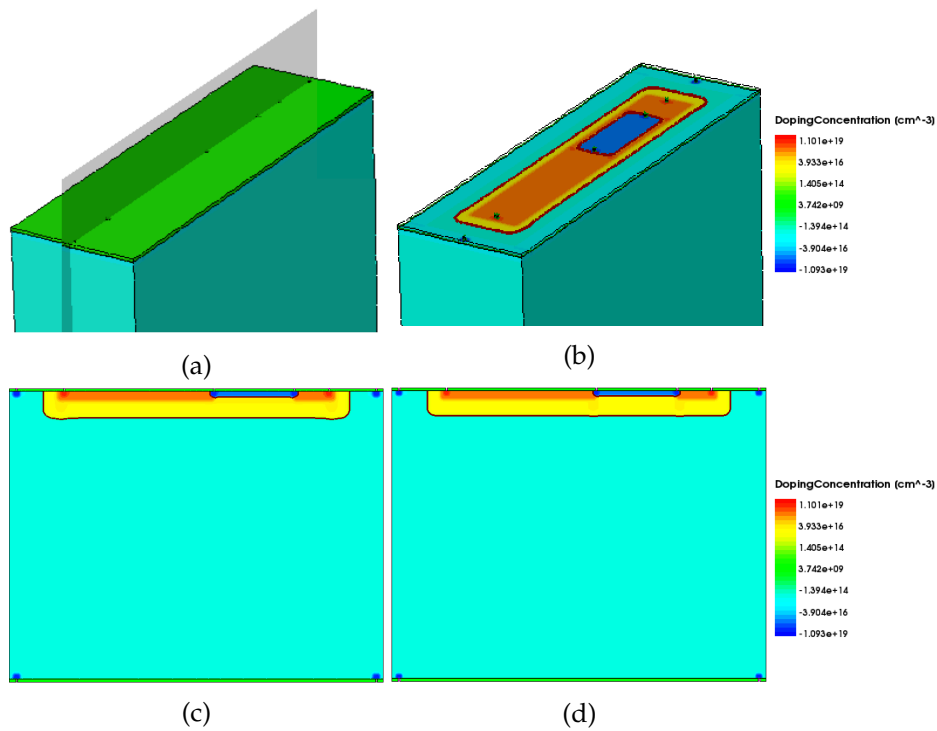


FIGURE 5.2: Models of the 20  $\Omega\cdot\text{cm}$  ATLASPix Simple pixel, including **a** the full 3D model with oxide layers, **b** the 3D model with oxide layers hidden, **c** a 2D cut through the center of the 3D model (the gray plane), and **d** the 2D model. In the doping concentration scale, n-type doping is denoted with positive numbers and p-type with negative numbers.

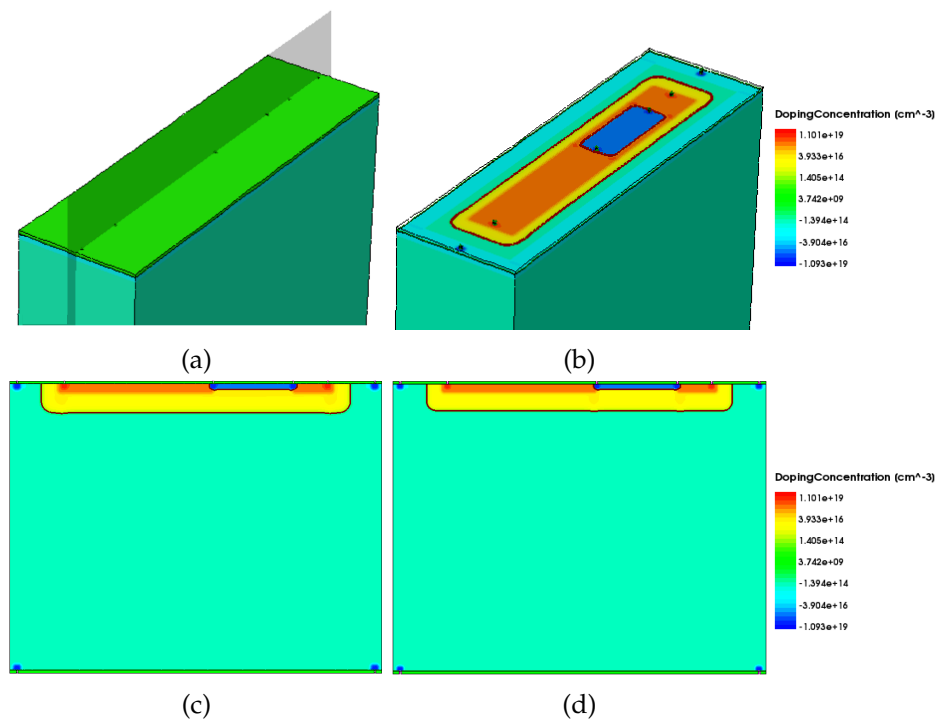


FIGURE 5.3: Models of the 80  $\Omega\cdot\text{cm}$  ATLASPix Simple pixel, including **a** the full 3D model with oxide layers, **b** the 3D model with oxide layers hidden, **c** a 2D cut through the center of the 3D model (the gray plane), and **d** the 2D model.

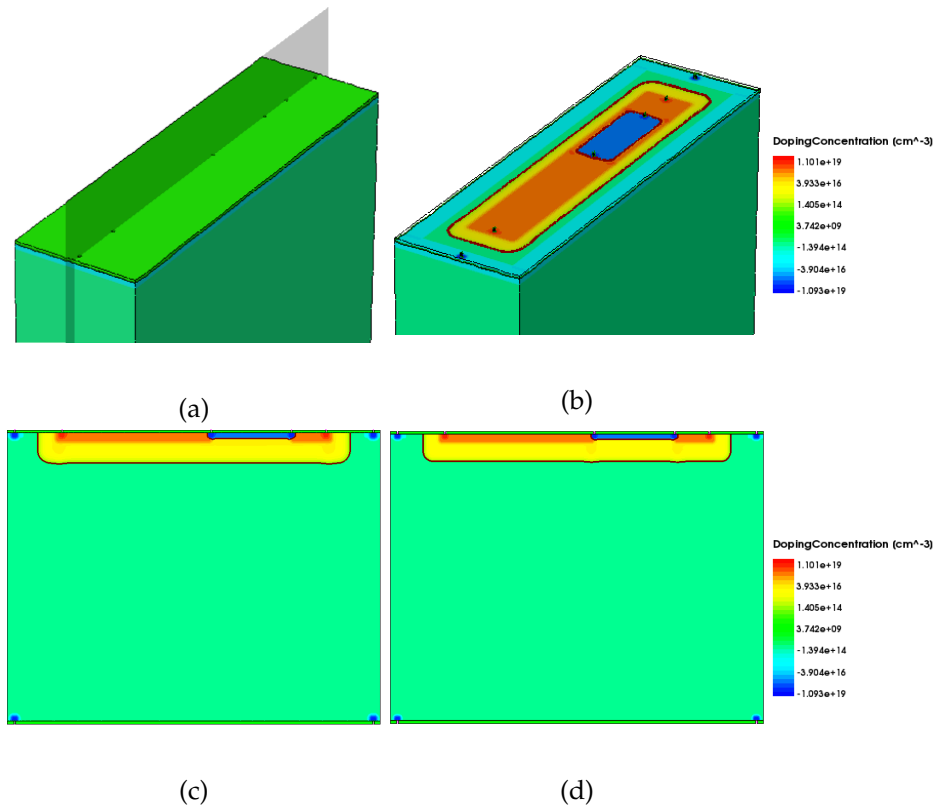


FIGURE 5.4: Models of the 200  $\Omega$ -cm ATLASPix Simple pixel, including the full 3D model with oxide layers, **a** the 3D model with oxide layers hidden, **b** a 2D cut through the center of the 3D model (the gray plane), and **c** the 2D model.

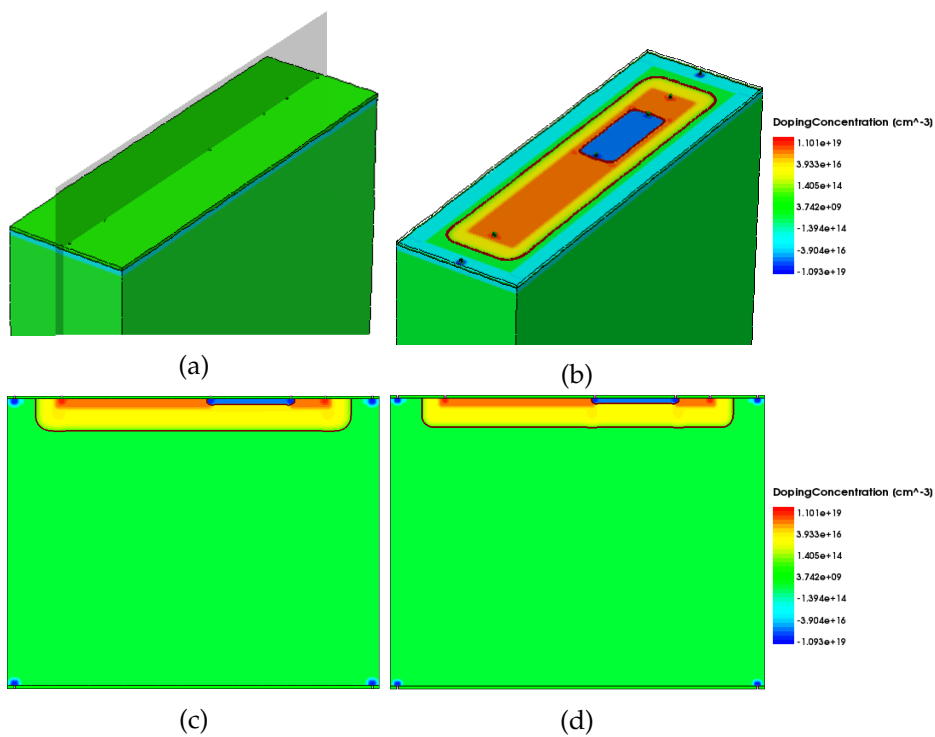


FIGURE 5.5: Models of the 1000  $\Omega$ -cm ATLASPix Simple pixel, including **a** the full 3D model with oxide layers, **b** the 3D model with oxide layers hidden, **c** a 2D cut through the center of the 3D model (the gray plane), and **d** the 2D model.

sensor, such as the transport or the recombination of charge carriers, and the list of models used in this simulation is summarized in Table B.2 in Appendix B.

Fig. 5.6 to Fig. 5.9 show the distribution of the electrostatic potential in the 3D and the 2D models of each of the four resistivities. A 2D cut through the center has been made for each 3D model to compare with the 2D simulation results. The electrostatic potential shows similar trends in all the models. A constant potential of  $-60.5$  V is achieved in the undepleted part of the p guard ring and the bulk, and a constant potential of  $0.5$  V in the p well, while in the undepleted part of the n-type wells, the electrostatic potential is  $2.3$  V. In a word, in p-type regions, the simulated voltage is  $0.5$  V lower than the specified external voltage, and in n-type regions, it is  $0.5$  V higher. This  $0.5$  V shift is caused by the built-in voltage of the p-n junction (see section 3.3). Inside the depletion zone, the electrostatic potential is the highest at its border in the n-type wells, and decreases towards the bulk and the p guard ring. For each resistivity, the 2D cut of the 3D model is comparable to the stand-alone 2D simulation, except that in cut of the 3D model, the resolution of the result is lower, and the decrease of the potential is faster. This is due to a coarser meshing that was used in the 3D model, to keep the computing time reasonable.

The border of the depletion zone is denoted by white lines (or planes in the 3D case). In general, the depletion zone starts near the lower edge of the deep n-well and the p guard ring, and extends into the bulk to form an oval-shaped region that grows deeper towards the center of the pixel. Still, due to the coarser meshing in the 3D model, the border of the depletion zone in the 3D model is not so smooth as that in the 2D model, and the depth of the depletion zone in the 3D model is also slightly smaller than in the 2D model. Besides, the shape and size of the depletion zone vary in models of different bulk resistivity. The  $20 \Omega\cdot\text{cm}$  model has the smallest depletion zone, with a width of  $121.5 \mu\text{m}$  and a depth of  $17.6 \mu\text{m}$  at the widest and the deepest point. The area of the depletion zone grows with the increase of bulk resistivity. The  $80 \Omega\cdot\text{cm}$  model is fully depleted in x direction, and its depletion zone extends to a peak depth of  $29 \mu\text{m}$  in y direction. The  $200 \Omega\cdot\text{cm}$  model is also fully depleted in x, and has a peak depletion depth of  $41.6 \mu\text{m}$ . The  $1000 \Omega\cdot\text{cm}$  model has the biggest depletion zone with an almost flat lower border, which is  $81.5 \mu\text{m}$  deep at its deepest point. The numbers are read from the 2D simulation, as the 2D models are generated with finer resolution.

A comparison of the electric field in the models of different bulk resistivity is shown in Fig. 5.10 to Fig. 5.13. As expected, a strong electric field exists in the depletion zone, and no field exists in the undepleted area. Similarly, the 3D model and the 2D model of the same bulk resistivity have comparable distribution of the electric field, except that the lower resolution and smaller depletion zone in the 3D model. The electric field is strongest at the lower corners of the deep n-well, and gradually decreases toward the edges of the depletion zone. Horizontally, the electric field is roughly uniform in the central part of the pixel, and decreases quickly toward the pixel edge, which indicates that, if a particle hits the edge of a pixel, the generated signal will be slower than that from particles in the central part of the pixel. Besides, the strength of the electric field in the depletion region becomes smaller with larger bulk resistivity. The  $20 \Omega\cdot\text{cm}$  model has the strongest electric field, with a peak value of  $1.15 \times 10^5$  V/cm, and in the  $80 \Omega\cdot\text{cm}$  model, the electric field strength decreases to  $7.8 \times 10^4$  V/cm. In the  $200 \Omega\cdot\text{cm}$  model, the peak electric field strength further decreases to  $5.81 \times 10^4$  V/cm. The  $1000 \Omega\cdot\text{cm}$  model has the weakest electric field with a peak strength of  $3.7 \times 10^4$  V/cm. The peak values of the depletion depth and the electric field for models of the four bulk resistivity values are summarized in Table 5.1.

bulk resistivity [ $\Omega\cdot\text{cm}$ ]	20	80	200	1000
peak depletion (y) [ $\mu\text{m}$ ]	17.6	29.0	41.6	81.5
peak depletion (x) [ $\mu\text{m}$ ]	121.5	fully depleted	fully depleted	fully depleted
peak electric field [V/cm]	$1.15 \times 10^5$	$7.8 \times 10^4$	$5.81 \times 10^4$	$3.7 \times 10^4$

TABLE 5.1: Table of the peak depletion zone width (x) and depth (y) and the peak electric field strength for 2D models with bulk resistivity values of 20  $\Omega\cdot\text{cm}$ , 80  $\Omega\cdot\text{cm}$ , 200  $\Omega\cdot\text{cm}$ , and 1000 $\Omega\cdot\text{cm}$ .

In summary, for all of the four bulk resistivity values, the electrical properties of the simplified 2D model are comparable to those of the 3D model, indicating that the 2D model is a valid approximation. Besides, because a 2D model takes much less time to run than a full 3D model, finer meshing can be applied to the 2D model to obtain results of higher resolution at the center of the pixel volume.

### Response to Particle

As discussed in the last section, as bulk resistivity increases, for a given bias voltage, the depleted volume, that is the sensitive zone for particle detection, becomes larger, but at the same time, the electric field in the depletion zone, which influences the speed of charge collection, becomes weaker. As a result, how bulk resistivity affects the charge collection ability of the sensor is not straightforward. To obtain a better understanding, a simulation of the transient process of charge collection in the sensor after being hit by a Minimum Ionizing Particle (MIP) has been made, and the response of the four models of different bulk resistivity have been studied and compared.

The deposited charge by the MIP is simulated with the Heavy Ion Model provided by Sentaurus Device [46]. This model describes the spatial and temporal distribution of the generated charge with Gaussian distributions, whose width, direction, position, and peak value are specified in the command file. The simulated MIP travels in the y direction through the center of the pixel. It deposits about 80 electron-hole pairs per  $\mu\text{m}^3$  over a length of 100  $\mu\text{m}$ . The width of the spatial distribution of the generated charge is 0.05  $\mu\text{m}$ , and the temporal width is  $5 \times 10^{-4}$  ns. Fig. 5.14a shows the initial spatial distribution of the charge generated by the MIP in the 20  $\Omega\cdot\text{cm}$  model.

The charge collection process in 100 ns after charge injection has been simulated. The transport of the charge carriers including thermal motion, drift, and diffusion, along with their generation and recombination have been taken into account in the simulation (see Section 3.2.2). The current density due to the drift and diffusion of the charge carriers is calculated using Eq. 3.15. The induced current on the collection electrode is calculated using the Ramo theorem (see Section 3.3.2).

Fig. 5.15a shows a comparison of the current induced on the charge collection electrode on the n-well in the first 5 ns in models of different resistivity values. The current in the four models shows similar behavior. It first increases quickly, and reaches a peak value of around  $4.5\text{-}5.5 \times 10^{-7}$  A in 0.2-0.4 ns. but starts to decrease after 0.4 ns and finally reaches a constant value of about  $2 \times 10^{-8}$  A. The 20 ohm model has the highest peak of  $5.45 \times 10^{-7}$  A, and the 1000  $\Omega\cdot\text{cm}$  model has the second-highest peak value of  $5.05 \times 10^{-7}$  A. The peak current in the 200 ohm model is slightly higher than the one in the 80  $\Omega\cdot\text{cm}$  model, and they are both around

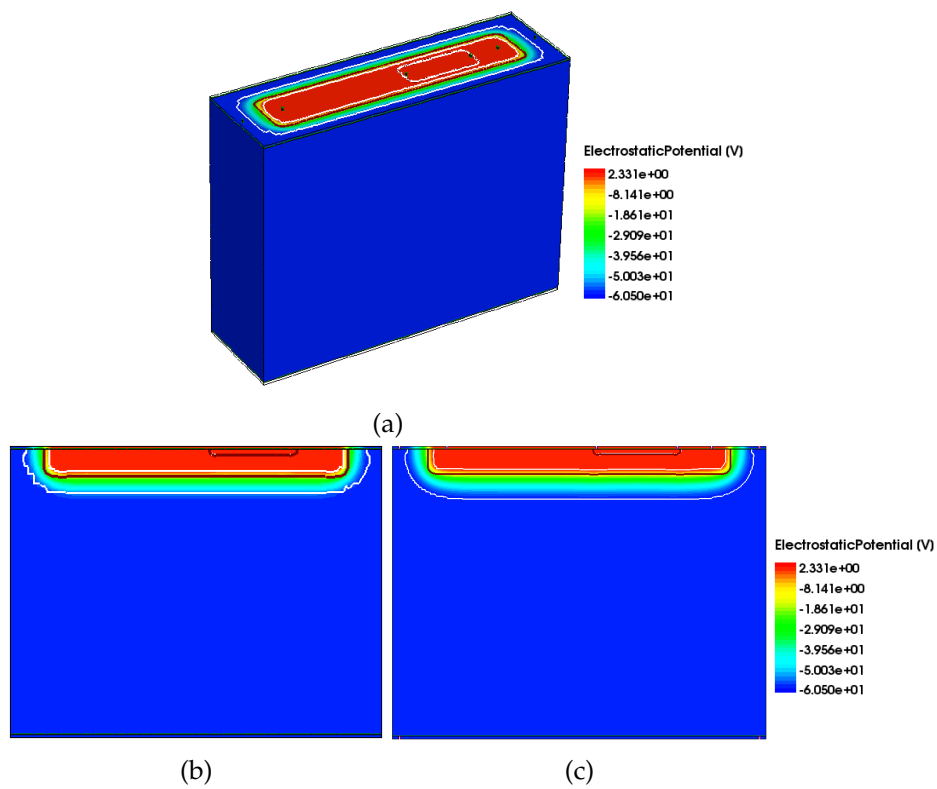


FIGURE 5.6: Distribution of electrostatic potential the 20  $\Omega$ -cm models: **a** 3D model with oxide layers hidden, **b** a 2D cut through the center of the 3D model, and **c** the 2D model. The depletion zone is denoted with white lines.

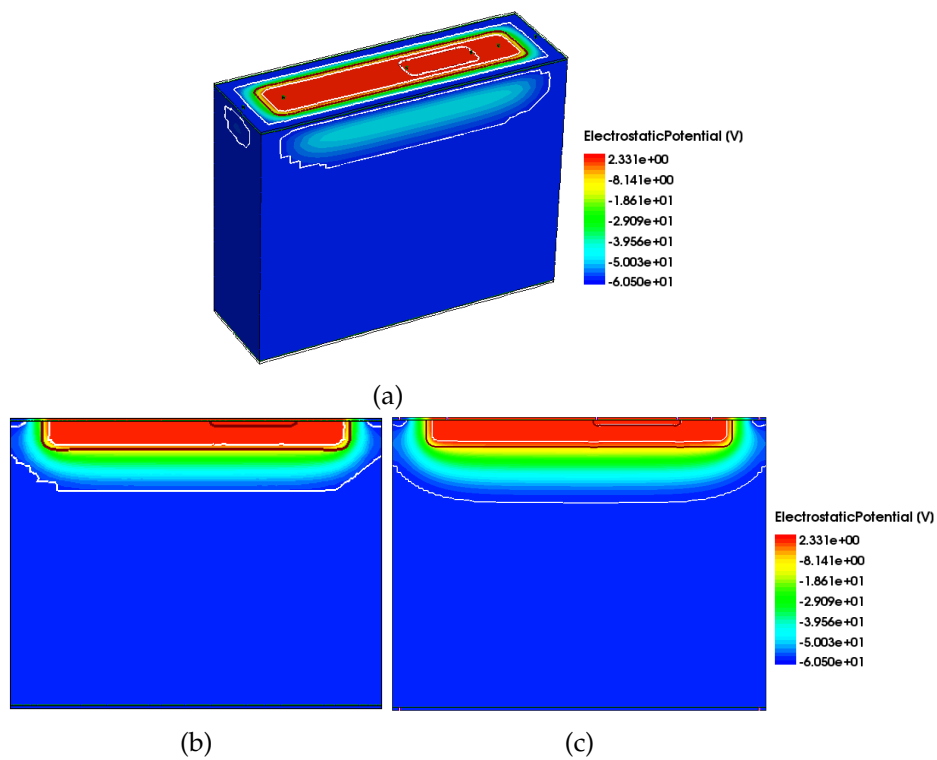


FIGURE 5.7: Distribution of electrostatic potential the 80  $\Omega$ -cm models: **a** 3D model with oxide layers hidden, **b** a 2D cut through the center of the 3D model, and **c** the 2D model.

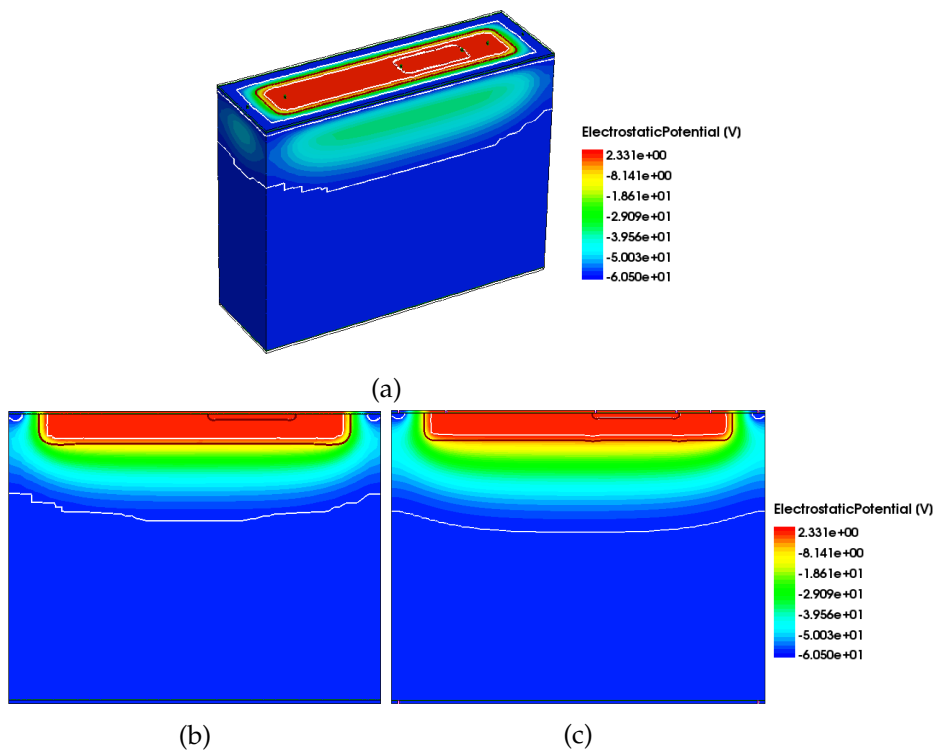


FIGURE 5.8: Distribution of electrostatic potential the 200  $\Omega\cdot\text{cm}$  models: **a** 3D model with oxide layers hidden, **b** a 2D cut through the center of the 3D model, and **c** the 2D model.

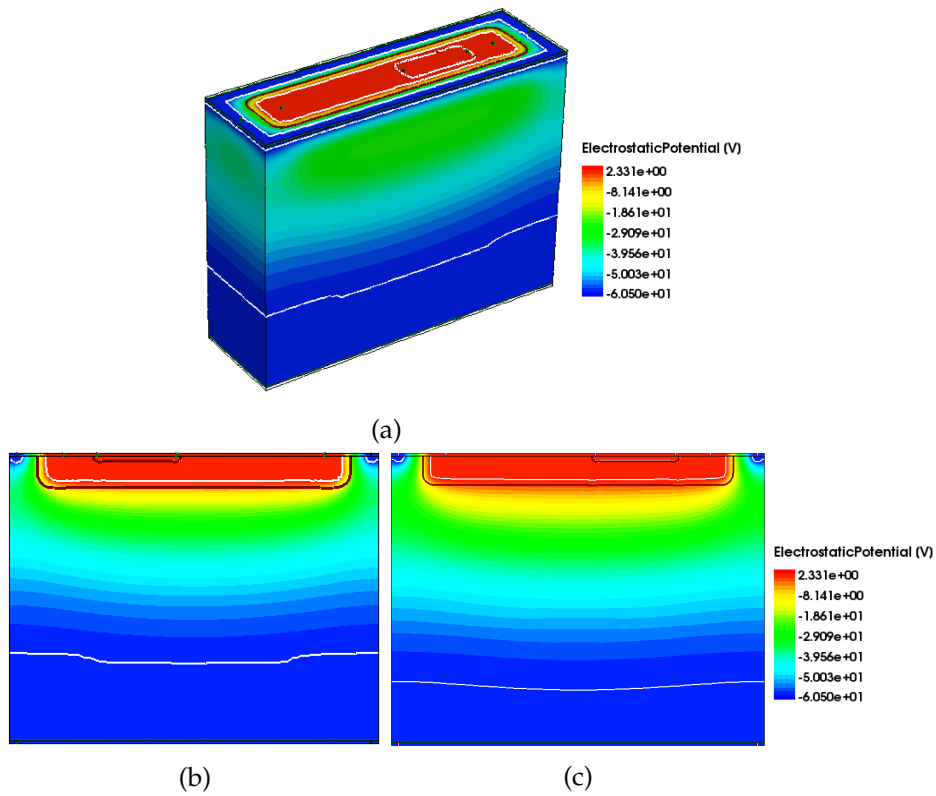


FIGURE 5.9: Distribution of electrostatic potential the 1000  $\Omega\cdot\text{cm}$  models: **a** 3D model with oxide layers hidden, **b** a 2D cut through the center of the 3D model, and **c** the 2D model.

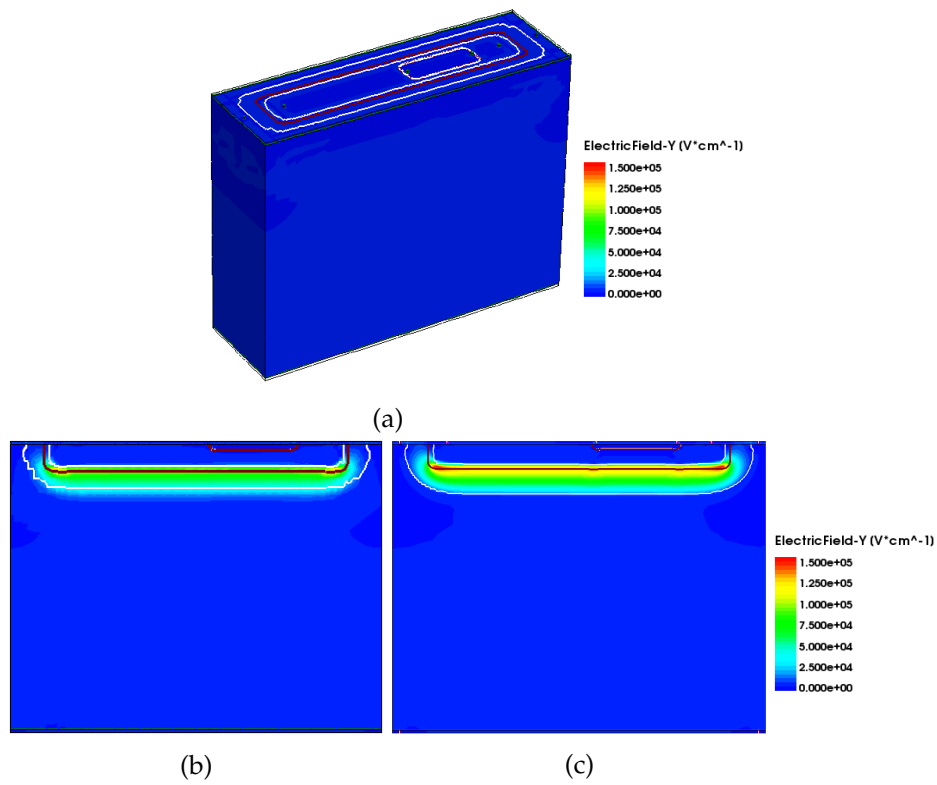


FIGURE 5.10: Absolute value of the electric field in the  $20 \Omega\cdot\text{cm}$  models: **a** 3D model with oxide layers hidden, **b** a 2D cut through the center of the 3D model, and **c** the 2D model.

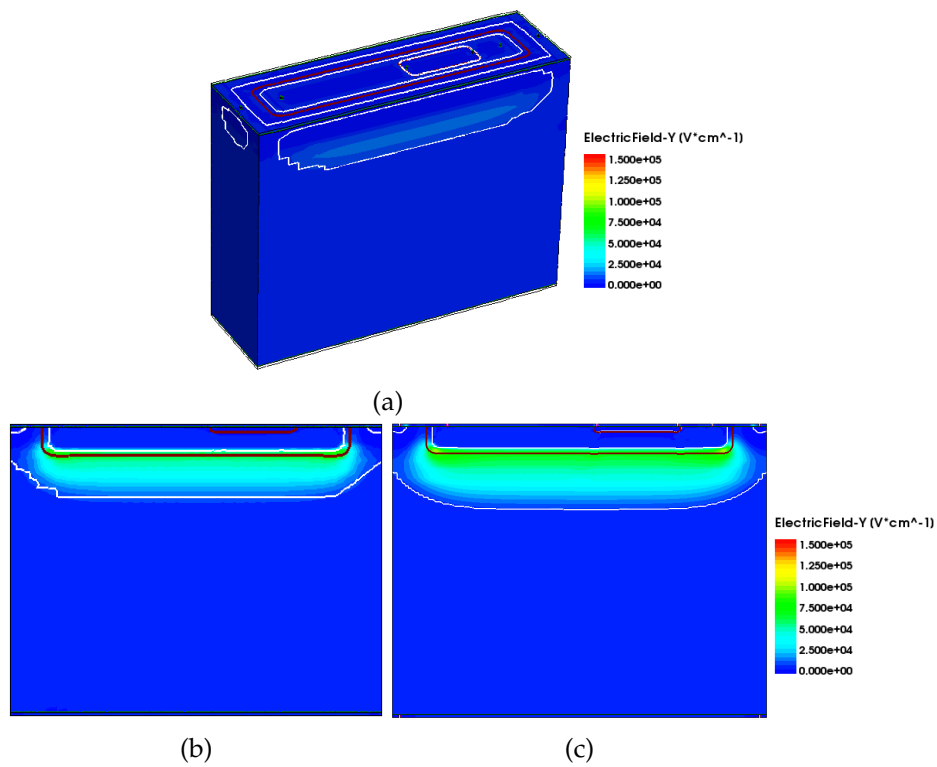


FIGURE 5.11: Absolute value of the electric field in the  $80 \Omega\cdot\text{cm}$  models: **a** 3D model with oxide layers hidden, **b** a 2D cut through the center of the 3D model, and **c** the 2D model.

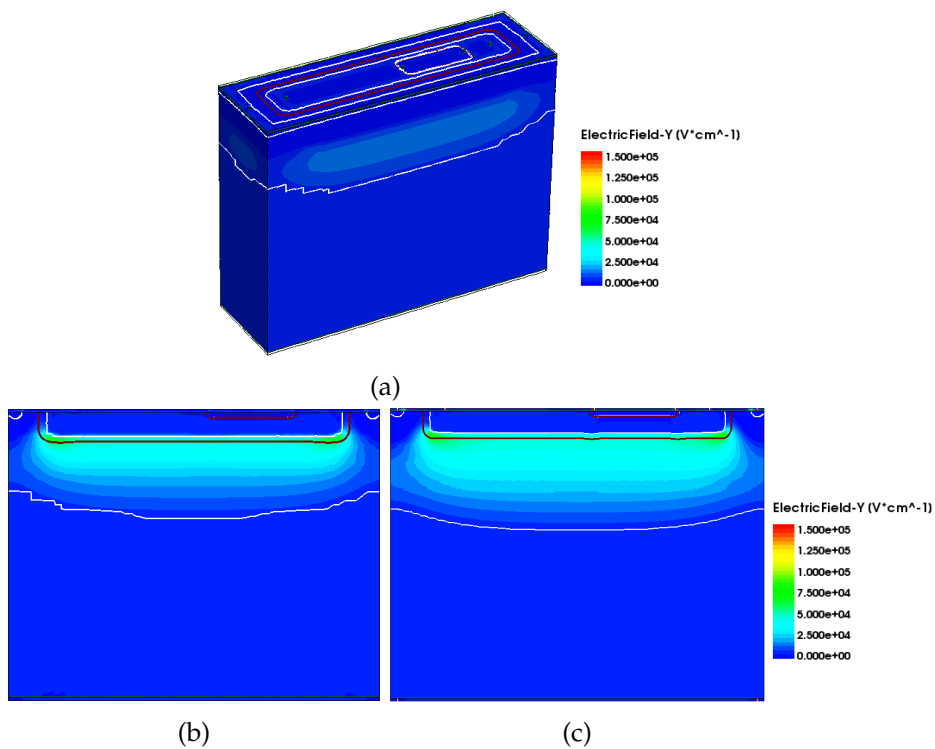


FIGURE 5.12: Absolute value of the electric field in the  $200 \Omega\cdot\text{cm}$  models: **a** 3D model with oxide layers hidden, **b** a 2D cut through the center of the 3D model, and **c** the 2D model.

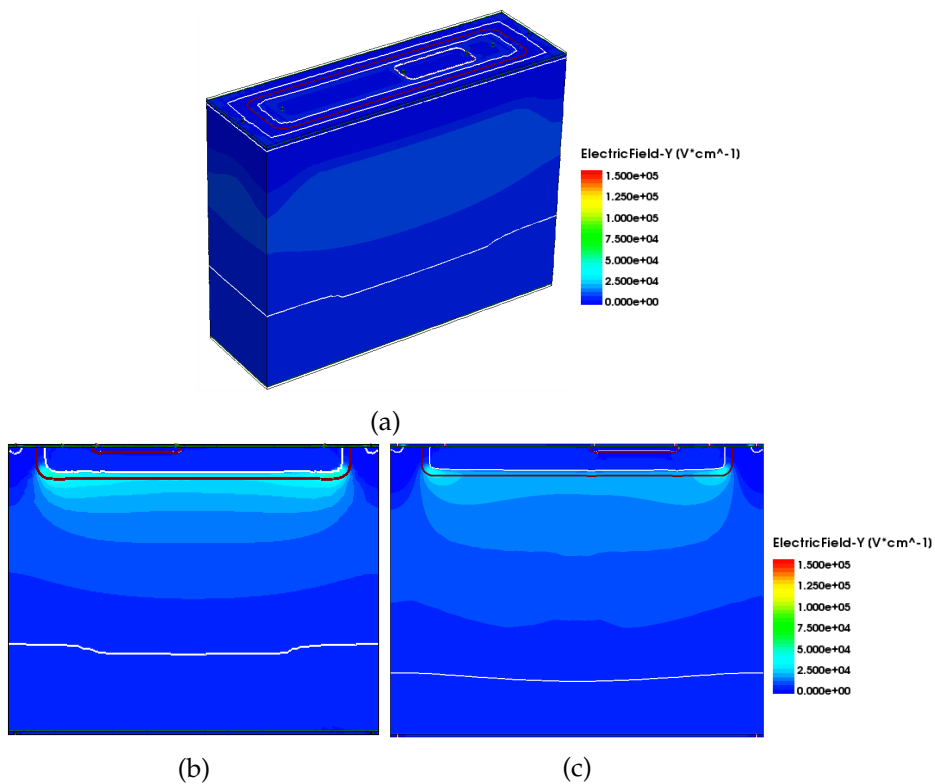


FIGURE 5.13: Absolute value of the electric field in the  $1000 \Omega\cdot\text{cm}$  models: **a** 3D model with oxide layers hidden, **b** a 2D cut through the center of the 3D model, and **c** the 2D model.

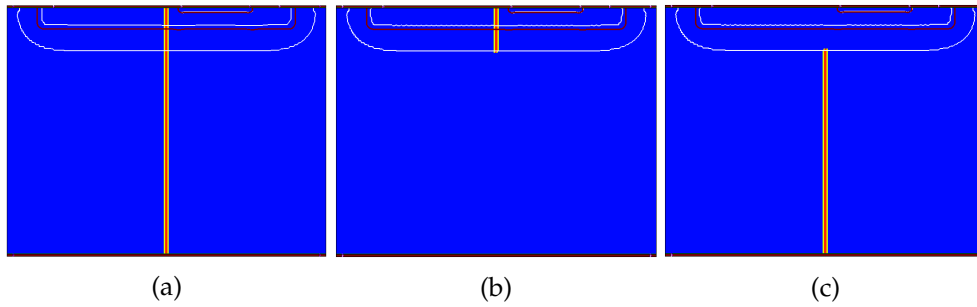


FIGURE 5.14: Initial distribution of the generated charge along different MIP paths in the 20  $\Omega\cdot\text{cm}$  model: **a**, the full MIP path across the center of the pixel, **b** the "drift path" inside the depletion zone, and **c** the "diffusion path" in the undepleted region.

$4.5 \times 10^{-7}$  A. After the peak, the current in the 20  $\Omega\cdot\text{cm}$  model drops the fastest, and reaches the minimum in 2 ns. In models of higher bulk resistivity, the current drop becomes noticeably slower. The current drop in the 1000  $\Omega\cdot\text{cm}$  model is the slowest.

The amount of collected charge is obtained by integrating the induced current over time, and a comparison of collected charge in 100 ns in the four models is shown in Fig. 5.15b. As expected, the amount of collected charge first increases rapidly for a few nanoseconds, and then gradually slows down to a constant and slow increasing speed, as the current reduces to the minimum. The rapid increase of the collected charge lasted no more than 2 ns in the 20  $\Omega\cdot\text{cm}$  model whose current drop was the fastest, while it lasted almost 10 ns in the 1000  $\Omega\cdot\text{cm}$  model with the slowest current drop. Except the first few nanoseconds, in most part of the 100 ns, the model of higher bulk resistivity collects a larger amount of charge. At 100 ns, the 1000  $\Omega\cdot\text{cm}$  model collected 8000 e of charge, while the 20  $\Omega\cdot\text{cm}$  model collected only 2900 e.

The detail of the charge collection process in the first 1 ns is shown in Fig. 5.15c. In the beginning, the charge collection speeds of the four models are similar. The 20  $\Omega\cdot\text{cm}$  and the 1000  $\Omega\cdot\text{cm}$  models collect 700 e in 0.25 ns. The 80  $\Omega\cdot\text{cm}$  and the 200  $\Omega\cdot\text{cm}$  models are slightly slower, and need 0.3 ns to collect 700 e of charge. Therefore, the performance of the four sensors are similar in the first 0.3 ns, and afterwards, the sensors with larger resistivity collect stronger signals.

To better understand the charge collection process, the MIP path has been split into "drift" and "diffusion" parts, as shown in Fig. 5.14b and 5.14c. The "drift" part refers to the particle track inside the depletion region, because the charge generated along this part of the track travels to the collection electrode mostly by the drift mechanism. The "diffusion" part refers to the section of the particle track outside the depletion region, as the charge along this part of the track needs to diffuse into the depletion region before they can be collected. Two simulations of the charge collection process in the sensor in 100 ns have been made with the "drift" MIP path and the "diffusion" MIP path.

The induced currents from the "drift" path simulation (hereafter as "drift" current) and the "diffusion" path simulation (hereafter as "diffusion" current) in 5 ns are shown in Fig. 5.16. The "drift" current was the main contributor to the initial rise in the "full" current, and at that time, the contribution from "diffusion" was negligibly low. Then the "drift" current quickly decreased and would be surpassed by the "diffusion" current as time went by. In addition, the "drift" and "diffusion" current have been summed up and compared to the current from the simulation with the full MIP path (hereafter as "sum" current and "full" current). The "sum" current and the "full" current agree to a sufficient level, but in a certain part in the current drop period, the sum current is slightly lower than the full current, and the discrepancy

becomes larger with larger bulk resistivity. A possible cause of this discrepancy is that the "drift", "diffusion", and "full" MIP paths affect the electric field differently in the simulation, so the sum of the two simulations with "drift" and "diffusion" paths is slightly different from the simulation with the "full" MIP path. Nevertheless, the discrepancy is small and only appear in a few nanoseconds. It is still safe to say that the splitting of the MIP path is valid.

The collected charge from the "drift" ("drift" charge) and "diffusion" paths ("diffusion" charge) in 100 ns for the four models is included in Fig. 5.17. Similarly, the "drift" charge and the "diffusion" charge has been summed up ("sum" charge) and compared to the "full" charge. The difference between the "sum" current and the "full" current is carried to the collected charge, resulting in the "full" charge rising faster than the "sum" charge for a few nanoseconds, which is especially noticeable in models with higher bulk resistivity. The discrepancy then becomes smaller, and after 50 ns, the "sum" charge and the "full" charge converges.

The "drift" charge is collected quickly. In all of the models, the majority of "drift" charge is collected within 5 ns and all of the "drift" charge is collected within 20 ns. On the contrary, the "diffusion" charge is collected slowly and constantly. The collected amount of "drift" charge increases with higher bulk resistivity. At 100 ns, the 1000  $\Omega\cdot\text{cm}$  model has collected 6600 e of "drift" charge, which is almost 6 times more than the amount collected by the 20  $\Omega\cdot\text{cm}$  model. On the other hand, as bulk resistivity increases, the collected amount of "diffusion" charge decreases slowly. The 20  $\Omega\cdot\text{cm}$  model has collected 1850 e of "diffusion" charge at 100 ns, while the 1000  $\Omega\cdot\text{cm}$  model has collected 1400 e. As a result, the charge collection process in low bulk resistivity models tends to be more dominated by diffusion, while the process in models with high bulk resistivity is more dominated by drift. For example, in the 20  $\Omega\cdot\text{cm}$  model, the "diffusion" charge becomes dominant after 35 ns, and accounts for 2/3 of the collected charge at 100 ns, while in the 1000  $\Omega\cdot\text{cm}$  model, the "drift" charge accounts for about 7/8 of collected charge at 100 ns. As is mentioned in Section 3.3.3, the "drift" charge is less influenced by radiation damage, and thus models with higher bulk resistivity will be more resistant to radiation.

## 5.3 Simulation of Four-Pixel Matrix

In this section, the 2D single pixel models are extended to four-pixel matrices, to study the charge sharing and edge effect between the pixels. To begin with, the response of each pixel to an upright particle at the center of a given pixel in the 20  $\Omega\cdot\text{cm}$  and 200  $\Omega\cdot\text{cm}$  models has been simulated and compared. In addition, the charge collection of each pixel for different particle incoming positions has been studied.

### 5.3.1 Simulated Structure

The structure is generated by flipping the single pixel model twice so to achieve a symmetrical structure. Just like in the single pixel model, two aluminum electrodes are added near the left and right edge of the p-well, n-well, and guard rings of each pixel, and two additional electrodes to the backside to tune the bulk potential. One thing to note is that two neighboring pixels share one guard ring and guard-ring electrode. Two models of bulk resistivity values of 20  $\Omega\cdot\text{cm}$  and 200  $\Omega\cdot\text{cm}$  have been simulated and compared. The layout of the simulated structure is shown in Fig. 5.18. The pixels are labelled pixel 1, 2, 3, and 4 from left to right. Periodic

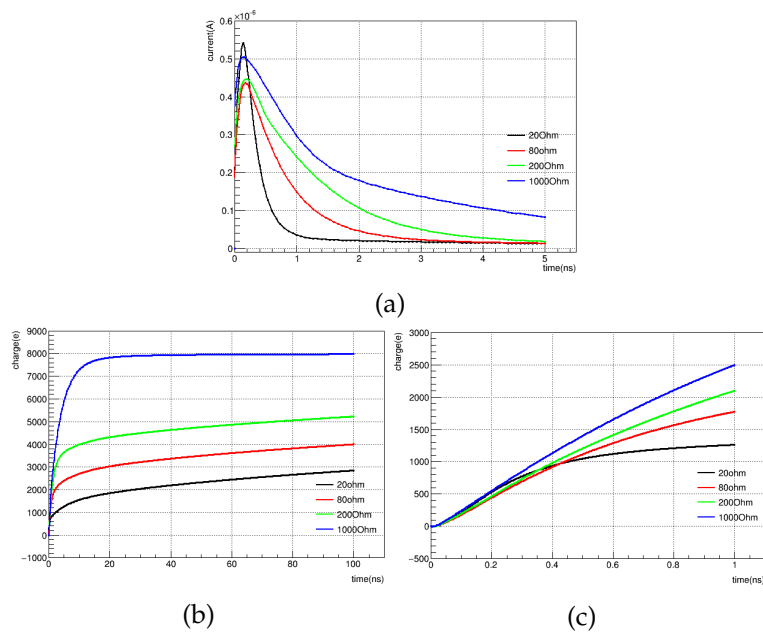


FIGURE 5.15: **a**: Induced current on the charge collection electrodes in models of different bulk resistivity. **b**: Charge collected in 100 ns by the signal collection electrodes in models of different bulk resistivity. **c** Charge collected in the first 1 ns.

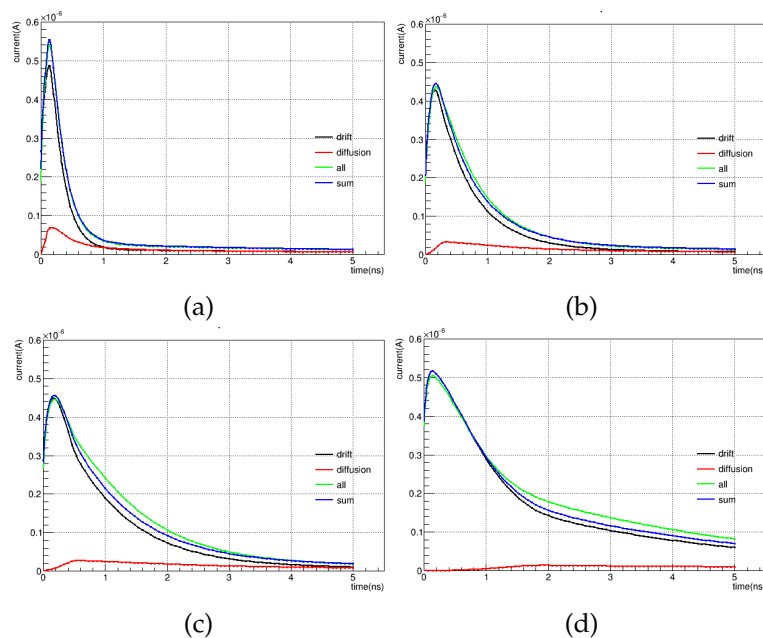


FIGURE 5.16: Induced current on the charge collection electrodes from simulations with "drift" path, "diffusion" path, and full MIP path of models of bulk resistivity of **a** 20  $\Omega \cdot \text{cm}$ , **b** 80  $\Omega \cdot \text{cm}$ , **c** 200  $\Omega \cdot \text{cm}$ , and **d** 1000  $\Omega \cdot \text{cm}$ . The blue curve is the sum of the "drift" and the "diffusion" current. It is compared to the green curve, the "full" current from the simulation with full MIP track.

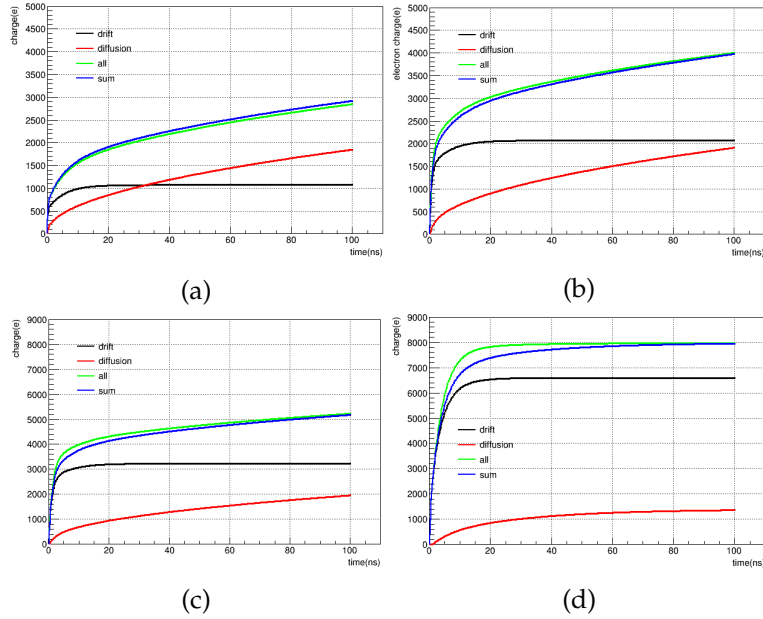


FIGURE 5.17: Collected charge by the charge collection electrodes from simulations with "drift" path, "diffusion" path, and full MIP path in models of bulk resistivity of **a**  $20 \Omega\cdot\text{cm}$ , **b**  $80 \Omega\cdot\text{cm}$ , **c**  $200 \Omega\cdot\text{cm}$ , and **d**  $1000 \Omega\cdot\text{cm}$ . The blue curve is the sum of the "drift" and the "diffusion" charge, and the green curve is the collected charge from the simulation with full MIP track.

boundary conditions were used at edge of the models to best replicate the multi-pixel structure.

### 5.3.2 Simulation of Device Operation

#### Electrical Properties

Similar to the single pixel simulation, the behavior of the four-pixel matrix under a bias voltage of  $-60 \text{ V}$  on the p guard ring and the bulk, a voltage on  $1.8 \text{ V}$  on the n-type wells, and a voltage of  $1.0 \text{ V}$  on the p well, have been simulated. All guard rings and the bulk are connected to the same high voltage source, while the p well and n-type wells in each pixel are connected to separate voltage sources. A comparison of the electrostatic potential, the depletion region, and the electric field is shown in Fig. 5.19 and Fig. 5.20. Again, an electrostatic potential of  $-60.5 \text{ V}$  is achieved at the p guard rings and the bulk, a potential of  $0.5 \text{ V}$  at the p well, and a potential of  $2.3 \text{ V}$  at the n-type wells. Besides, as is expected, in the  $20 \Omega\cdot\text{cm}$  matrix, the depletion zone is narrow and disconnected at the edge, and the electric field inside the depletion zone is strong. The  $200 \Omega\cdot\text{cm}$  matrix has a deeper and continuous depletion zone, but the electric field is only half as strong as the one in the  $20 \Omega\cdot\text{cm}$  matrix. In both models, the depletion zone is deeper and the electric field in the zone is stronger in the center of the pixels than at the edge, which indicates that, for both models, the collected charge from a particle hitting the edge of the pixels is smaller than that from a particle that hits the center of a pixel, and this effect should be stronger for models with lower resistivity.

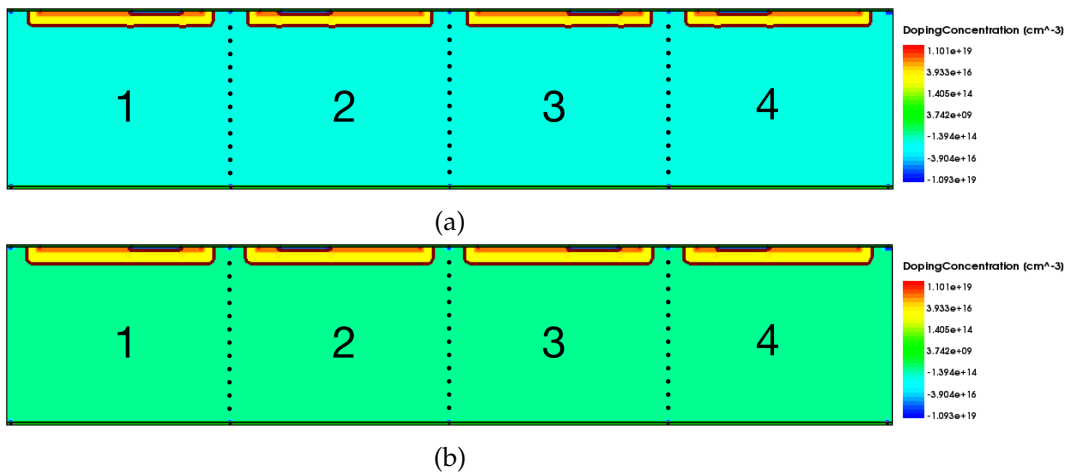


FIGURE 5.18: Simulated structure of a matrix of 4 ATLASPix Simple pixels with bulk resistivity of 20  $\Omega\cdot\text{cm}$  (a) and 200  $\Omega\cdot\text{cm}$  (b).

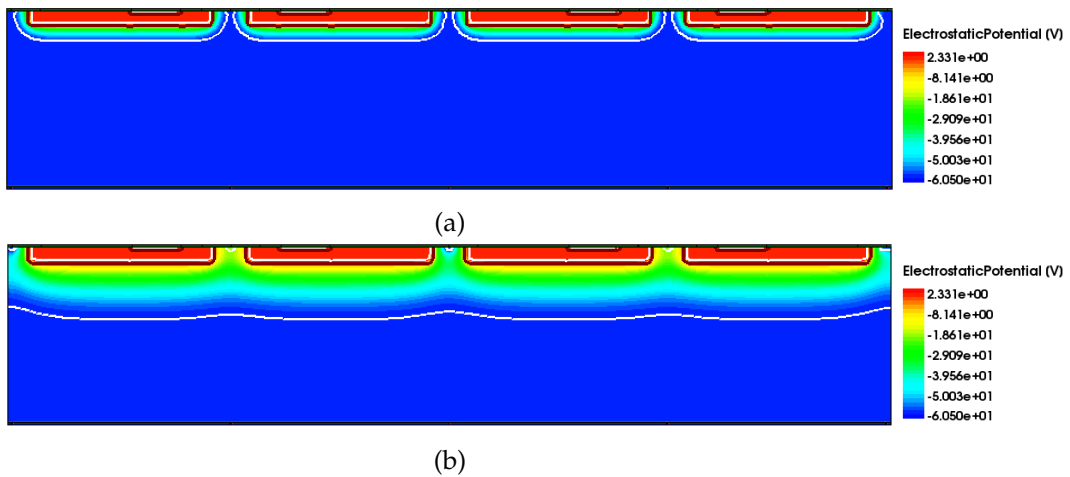


FIGURE 5.19: Electrostatic potential in 4-pixel models with bulk resistivities of 20  $\Omega\cdot\text{cm}$  (a) and 200  $\Omega\cdot\text{cm}$  (b). The white lines denote the border of the depletion zone.

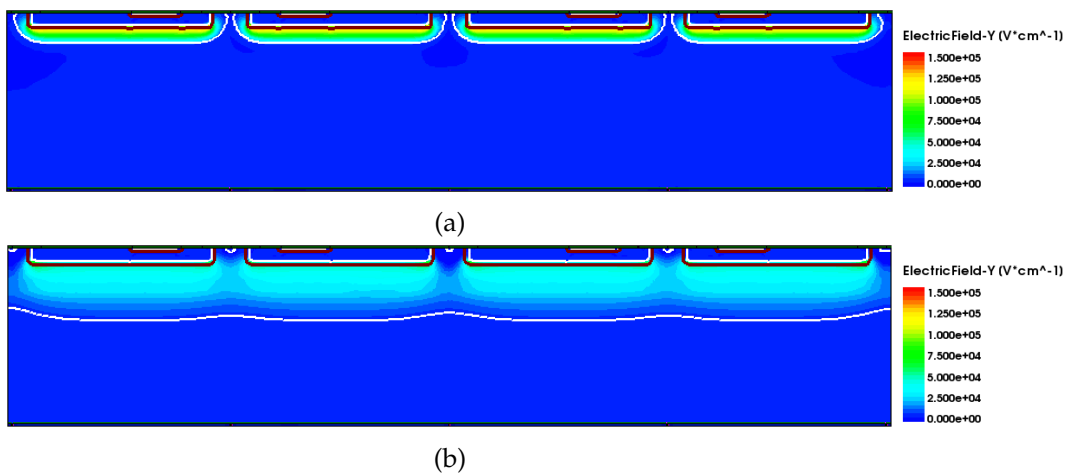


FIGURE 5.20: Electric field in 4-pixel models with bulk resistivities of 20  $\Omega\cdot\text{cm}$  (a) and 200  $\Omega\cdot\text{cm}$  (b). The white lines denote the border of the depletion zone.

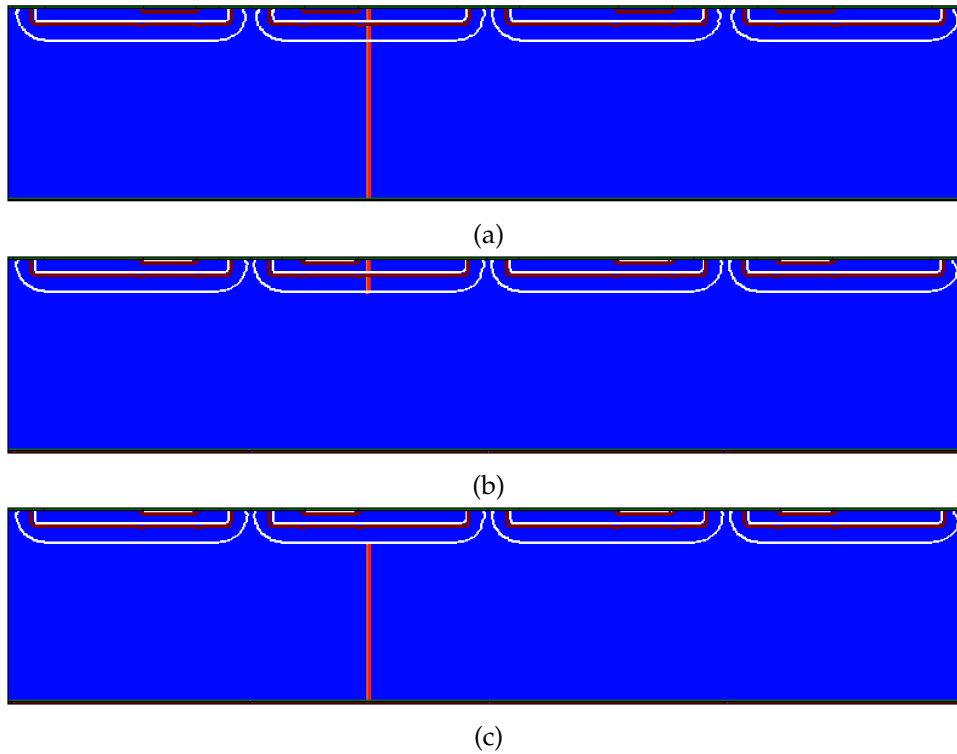


FIGURE 5.21: Generated charge in the 20  $\Omega\cdot\text{cm}$  model along: **a** full upright particle track at the center of pixel 2, **b** the "drift" path, and **c** the "diffusion" path.

### Response to Minimum Ionizing Particle

To study the charge sharing between pixels, the charge collection process in the matrix after a particle hits the center of pixel 2 has been simulated. The induced current and the collected charge of each pixel in the matrix have been simulated and analyzed. Besides, simulations with the full MIP path, the "drift" path, and the "diffusion" path have been made, to investigate the contribution of different MIP paths separately.

The particle is again simulated with the Heavy Ion Model. It travels vertically through the matrix, and has a spatial width of  $0.05\ \mu\text{m}$  and a temporal width of  $5 \times 10^{-4}\ \text{ns}$ . Similarly, the particle creates about 80 electron-hole pairs per  $\mu\text{m}^3$ . The initial distribution of the generated charge along the full particle track, the "drift" path, and the "diffusion" path in the 20  $\Omega\cdot\text{cm}$  matrix is included in Fig. 5.21.

The induced currents on each pixel in the 20  $\Omega\cdot\text{cm}$  and the 200  $\Omega\cdot\text{cm}$  matrices are shown in Fig. 5.22a and 5.22b. The shape of the current pulse in pixel 2 is similar to that in the single pixel simulation. It quickly rises to a peak of  $6.2\text{-}6.5 \times 10^{-7}\ \text{A}$  at 0.2 ns, and then decreases to a minimum around  $2 \times 10^{-8}\ \text{A}$ . The current in the 200  $\Omega\cdot\text{cm}$  model decreases noticeably more slowly than the current in the 20  $\Omega\cdot\text{cm}$  model. Meanwhile, small negative currents are formed on pixel 1 and pixel 3. The negative currents reach a peak of about  $-1 \times 10^{-7}\ \text{A}$  at 0.1 ns, and start to decrease afterwards. They become positive after a while. The positive pulses are lower and wider compared to their negative predecessors, and reduce to 0 as the current on pixel 2 reduces to the minimum. Both the negative and the positive pulses are noticeably wider in the 200  $\Omega\cdot\text{cm}$  model than in the 20  $\Omega\cdot\text{cm}$  model. As for pixel 4, a very small negative current is formed in the beginning, and it reduces to zero in 0.5-1 ns. This current induced in the neighboring pixels is caused by an effect called

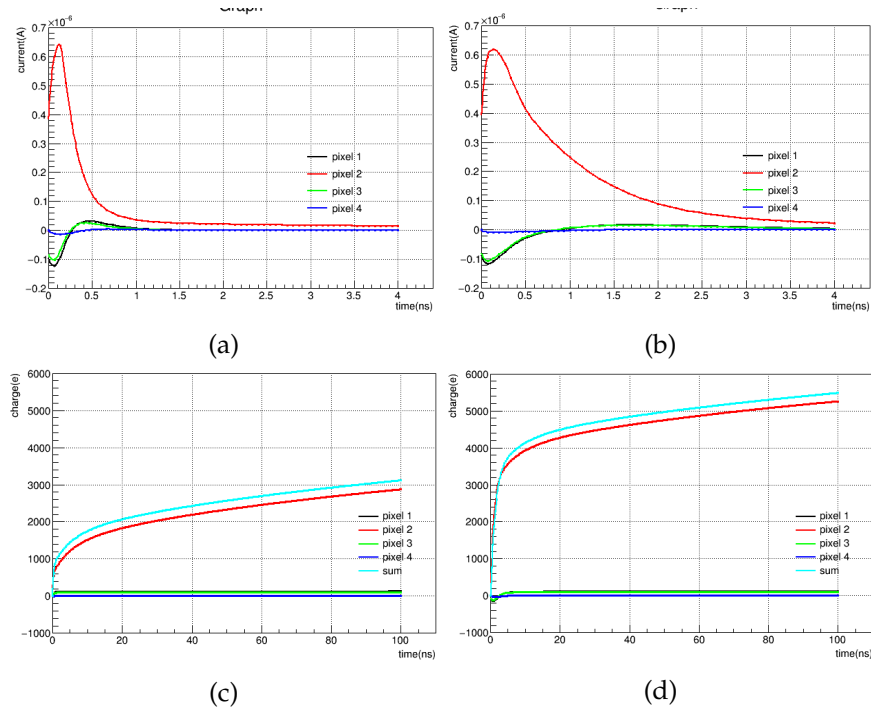


FIGURE 5.22: **a** and **b**: Current on collection electrodes on each pixel after particle hits the center of pixel 2 in the 20 Ω·cm (**a**) and 200 Ω·cm (**b**) matrices. **c** and **d**: Charge collected by the pixels in the 20 Ω·cm (**c**) and 200 Ω·cm (**d**) matrices.

charge sharing.

The collected charge by the pixels in the 20 Ω·cm and the 200 Ω·cm matrices is shown in Fig. 5.22c and Fig. 5.22d. At 100 ns, pixel 2 in the 20 Ω·cm matrix has collected about 2900 e of charge, while pixel 1 and pixel 3 have collected a small amount of charge (100 e) each due to charge sharing. Pixel 4 has collected almost no charge. The total amount of charge collected by the 20 Ω·cm matrix is 3200 e. As for the 200 Ω·cm matrix, the pixel 2 has collected 5300 e of charge in 100 ns. In the first 5 ns, the amount of charge collected by pixel 1 and pixel 3 is negative. Pixel 1 and pixel 3 start to collect positive charge after 5 ns. After 10 ns, their collected charge reaches a plateau of 100 e. Again, pixel 4 has collected no charge. The total amount of charge collected by the 200 Ω·cm matrix is 5500 e.

The contributions to collected charge from drift and diffusion have been simulated and studied. Similarly, the electrons generated along the particle track have been split into "drift" and "diffusion" parts based on whether or not they were generated inside the depletion zone (see Fig. 5.21b and 5.21c), and the charge collection process for both the "drift" and the "diffusion" path has been simulated. The results are summarized in Fig. 5.23.

Fig. 5.23a and 5.23b are the plots of the "drift" and "diffusion" charge collected in 100 ns by the collection electrodes on each pixel in the 20 Ω·cm matrix, and Fig. 5.23c and 5.23d are the plots for the 200 Ω·cm matrix. One can see that the charge sharing effect is only present in the "drift" charge. For the 20 Ω·cm matrix, in the "drift" simulation, pixel 2 has collected 950 e in 100 ns, while pixel 1 and pixel 3 has collected 100 e due to the charge sharing effect. As for the "diffusion" charge, pixel 2 has collected about 1850 e in 100 ns, and the other pixels did not collect any "diffusion" charge. In the 200 Ω·cm matrix, pixel 2 has collected 3300 e of "drift" charge in 100 ns. Pixel 1 and pixel 3 have collected negative charge at first, but have

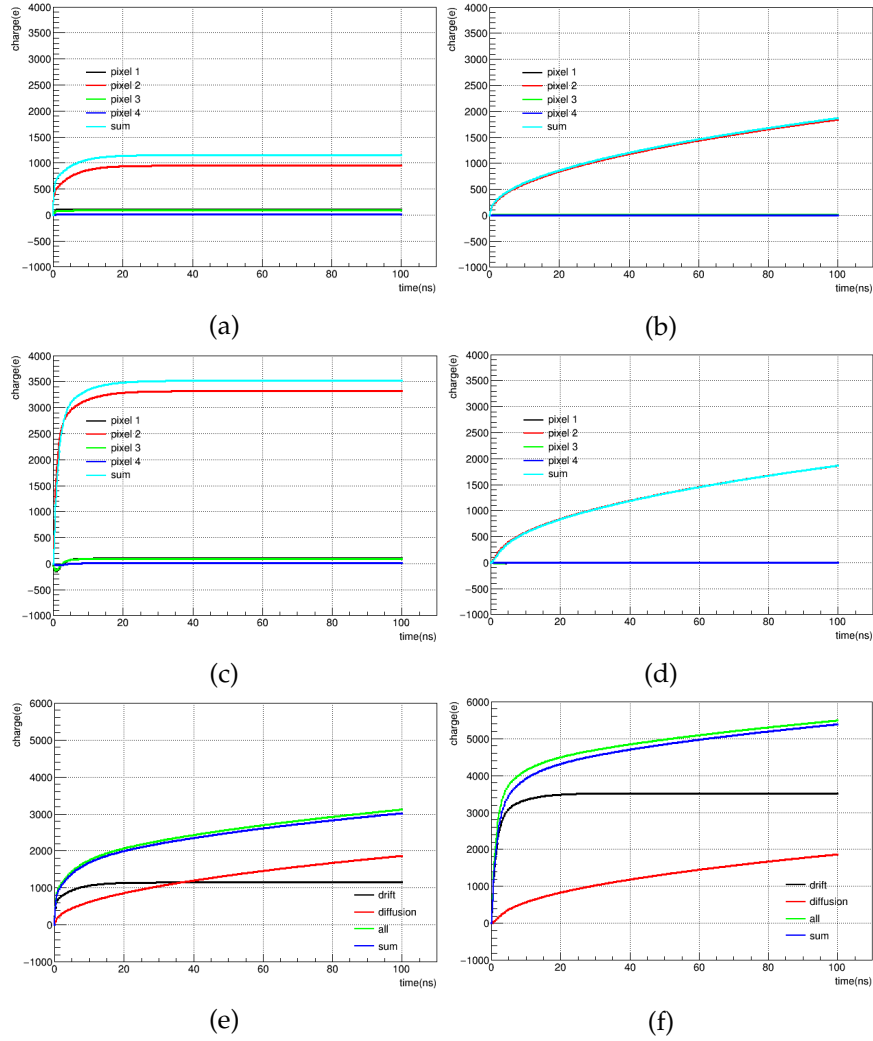


FIGURE 5.23: **a** and **b**: "Drift" (**a**) and "diffusion" (**b**) charge collected by each pixel in the  $20 \Omega\cdot\text{cm}$  matrix. **c** and **d**: "Drift" (**c**) and "diffusion" (**d**) charge collected by pixels in the  $200 \Omega\cdot\text{cm}$  matrix. **e** and **f**: Comparison of the sum of "drift" and "diffusion" charge (blue curve) with the "full" charge (green curve) from the simulation with full MIP path in the  $20 \Omega\cdot\text{cm}$  (**e**) and the  $200 \Omega\cdot\text{cm}$  (**f**) matrices.

each collected 100 e of "drift" charge in the end. The total amount of "drift" charge is 3500 e. Similarly, all "diffusion" charge has been collected by pixel 2, and the diffusion process did not cause the charge sharing effect on the neighboring pixels. In Fig. 5.23e and 5.23f, the "drift" and "diffusion" charge have been summed up and compared to the collected charge in the simulation with the full MIP path. Due to the reason discussed in section 5.2.2, the "sum" charge is slightly lower than the "full" charge. At 100 ns, the discrepancy in both  $20 \Omega\cdot\text{cm}$  and  $200 \Omega\cdot\text{cm}$  models is smaller than 2%, indicating that the simulation results with split MIP paths are valid.

To study the edge effect on charge collection, a series of simulations of upright particles entering at a certain point between the center of pixel 2 and the center of pixel 3 have been made. Fig. 5.24 illustrates the possible positions of the particles. Fig. 5.25 shows the collected charge for particles entering from different locations in the  $20 \Omega\cdot\text{cm}$  and  $200 \Omega\cdot\text{cm}$  models. For a given pixel, the biggest amount of charge is collected when the particle goes through its n-type wells. As the particle leaves its charge collection well and moves further away, the amount of collected charge

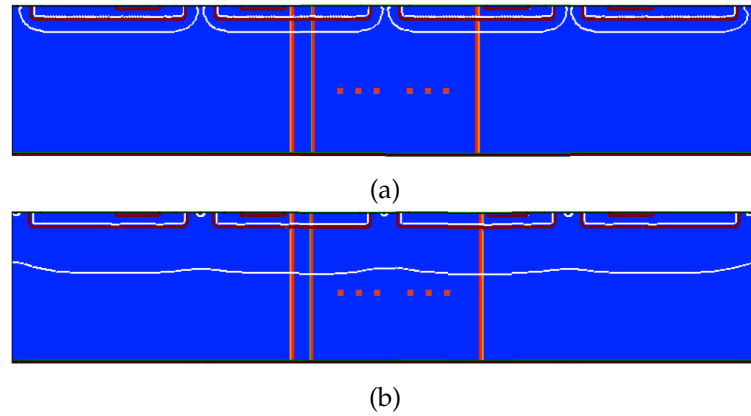


FIGURE 5.24: Possible particle incoming points between the center of pixel 2 and pixel 3 in the  $20 \Omega\cdot\text{cm}$  (a) and  $200 \Omega\cdot\text{cm}$  (a) matrices. For each bulk resistivity, a total of ten particles were simulated.

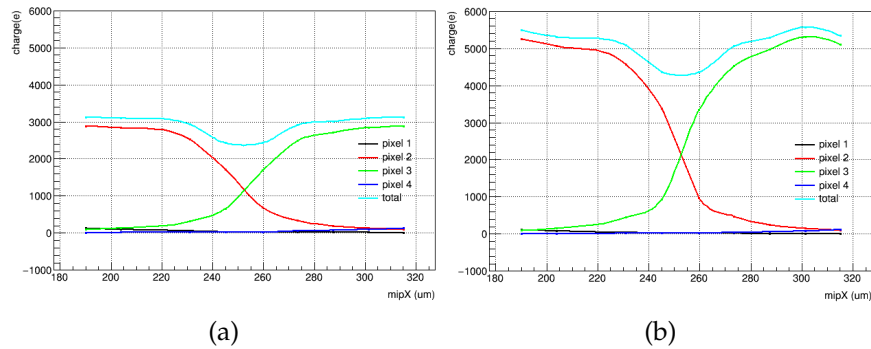


FIGURE 5.25: Charge collected by each pixel in the matrix for different incoming particle positions for: **a** upright particle in  $20 \Omega\cdot\text{cm}$  model, and **b** upright particle in  $200 \Omega\cdot\text{cm}$  model.

starts to decrease. The decrease is fastest when the particle is in the the edge area between two pixels. Finally, the collected charge drops to zero when the particle is two pixels away. As for the total amount of collected charge, one can see that more charge is collected when a particle hits the center of a pixel than when a particle hits the edge between two pixels. This phenomenon is called the edge effect. In the  $20 \Omega\cdot\text{cm}$  model, when the particle hits the center of a pixel, the matrix collects  $3200 e$  in  $100 \text{ ns}$ , and when the particle hits the edge between two pixels, the collected charge decreases by 25% to  $2400 e$ . As for the  $200 \Omega\cdot\text{cm}$  model, the matrix collects about  $5500 e$  in  $100 \text{ ns}$  if the particle is in the central part of a pixel, and collects  $4400 e$  in  $100 \text{ ns}$  if the particle is at the edge. The drop in collected charge caused by the edge effect is 20 %. As expected, the influence of the edge effect is stronger on sensors with low bulk resistivity.

## 5.4 Summary

To begin with, 3D and 2D TCAD simulation models of a single ATLASPix 1 pixel of bulk resistivity values of  $20, 80, 200,$  and  $1000 \Omega\cdot\text{cm}$  have been presented. For each resistivity, the distribution of the electrostatic potential and the electric field in the 3D and 2D models is similar, and thus the 2D model represents a good and fast approximation. Besides, because the 2D simulation takes much less time to finish,

finer meshing can be used to obtain results of higher resolution. The models with higher bulk resistivity have larger depletion zones than low resistivity models, but the absolute value of the electric field inside the depletion zone is also weaker. In the center of the pixel, the depletion zone is deeper and the electric field is stronger than at the edge of the pixel, which means that if a particle hits the edge of the pixel, less charge will be collected than if it hits the center of the pixel.

The response to a ionizing particle crossing the sensor perpendicularly and the charge collection process in the 2D models of the four values of bulk resistivity have been presented. The sensor collects charge quickly during the first few nanoseconds, and then charge collection slows down to a constant speed. The model with larger resistivity has longer charge collection time and in turn collects more charge. In 100 ns, the 1000  $\Omega\cdot\text{cm}$  model has collected more than twice the amount of charge collected by the 20  $\Omega\cdot\text{cm}$  model. Separate simulations with particle paths inside and outside the depletion zone show that the charge created along the path inside the depletion zone is collected quickly in 20 ns, and the charge along the path outside the depletion zone forms a slow but constantly growing signal. The larger the bulk resistivity, the greater is the proportion of the fast signal.

In addition, 2D simulation models of four-pixel matrices of bulk resistivity of 20  $\Omega\cdot\text{cm}$  and 200  $\Omega\cdot\text{cm}$  have been presented. For a vertical particle at the center of pixel 2, a signal similar to the one in the single pixel case is formed on pixel 2. However, in the first few nanoseconds, negative signals are formed on pixel 1 and pixel 3. The negative signals then decrease and become positive. In 100 ns, pixel 1 and pixel 3 have collected about 100 e of charge. This is called the charge sharing effect, and the effect lasts longer in the 200  $\Omega\cdot\text{cm}$  matrix. Separate simulations of the "drift" and "diffusion" signals show that the charge sharing effect comes from the "drift" charge.

Last but not the least, a series of vertical particles entering from the center of pixel 2 and the center of pixel 3 have been simulated to study the edge effect. As expected, when a particle hits the edge between two pixels, less charge is collected than when it hits the central area. In the 20  $\Omega\cdot\text{cm}$  matrix, when a particle hits the edge, the collected charge in 100 ns decreases by 25%, while in the 200  $\Omega\cdot\text{cm}$  matrix, the collected charge decreases by 20%. Thus the influence of the edge effect is weaker for sensor matrix of larger bulk resistivity.



## Chapter 6

# Summary and Outlook

This thesis presents two simulation studies that play an important role in the R&D of the ATLASPix, a monolithic candidate pixel sensor for the ATLAS ITK in the Phase II upgrade.

To begin with, simulation models emulating the FE-I4 beam telescope, with inclined and upright telescope planes, have been constructed with the generic pixel sensor simulation package AllPix<sup>2</sup>. The simulation models have been validated with the testbeam data taken at the H8 beamline of the CERN SPS accelerator. The simulated data have been reconstructed with the package Proteus, and the reconstruction accuracy of the inclined and the upright models has been evaluated and compared. The simulation results confirmed that the inclination of the telescope planes led to a position reconstruction with a better resolution, and thus with a more precise measurement of the prototype sensor properties.

In addition, TCAD simulation has been conducted with the software provided by Synopsis for the ATLASPix Simple matrix, one of the first large-scale fully monolithic prototype pixel matrices of the ATLASPix design. Full 3D models and simplified 2D models of the vertical cross section through the center of the sensor have been constructed for a single ATLASPix Simple pixel with bulk resistivity values of 20, 80, 200, 1000  $\Omega\cdot\text{cm}$ . The devices operation under a given set of external voltages have been simulated, and the results regarding the depletion region and the distribution of electric field inside the devices have been obtained. The 2D cut through the center of each 3D model has been obtained and compared with the 2D model of the same bulk resistivity. It has been found that they agree well, indicating that the simplified 2D model is a valid resource-friendly approximation of the full model. As expected, a strong electric field exists inside the depletion zone, while there is no electric field in the undepleted bulk regions. This simulation has shown that for higher bulk resistivity, the depletion zone is deeper, while the strength of the electric field becomes weaker. For example, the depletion zone in the 1000  $\Omega\cdot\text{cm}$  model is more than 4 times greater than that in the 20  $\Omega\cdot\text{cm}$  model, but the peak value of the electric field in the 1000  $\Omega\cdot\text{cm}$  is only 1/3 of the peak value in the 20  $\Omega\cdot\text{cm}$  model. The charge generation and collection processes in the single pixel models have been simulated for particle at the center of the pixels. The collected charge in all of the four models increases rapidly at first, and then gradually slows down to a small and constant speed. For a threshold of 700 e, a signal appears in 0.25 ns in the 20  $\Omega\cdot\text{cm}$  and the 1000  $\Omega\cdot\text{cm}$  models, and in 0.3 ns in the 80  $\Omega\cdot\text{cm}$  and 1000  $\Omega\cdot\text{cm}$  models. The difference is small, and it is safe to conclude that all models collect signals fast enough. After 0.3 ns, the models with higher bulk resistivity collect noticeably stronger signal than their lower resistivity counterparts. After 100 ns, the charge collected by the 1000  $\Omega\cdot\text{cm}$  model is almost three times larger than the charge collected by the 20  $\Omega\cdot\text{cm}$  model. The contributions from the charge inside the depletion zone, which drifts to the collection electrode, and that from the charge in the undepleted

regions, which needs to diffuse into the depletion zone before they can drift to the electrode, have been studied separately. It has been found that the initial fast signal is due to the "drift" charge, which is fully collected in 20 ns. The slow increase afterwards is due to the "diffusion" charge. The amount of the "drift" signal increases drastically with higher bulk resistivity, while the "diffusion" signal only decreases slightly. As a result, more ohmic models collect stronger signals.

Moreover, 2D models of four-pixel matrices with bulk resistivity values of 20  $\Omega\cdot\text{cm}$  and 200  $\Omega\cdot\text{cm}$  have been constructed to study the influence of the adjacent pixels. The device operation under the same boundary conditions has been simulated and the results agree well with those from the single pixel simulation. The charge collection process after a particle hits perpendicularly the center of pixel 2 has been simulated for both models. The process in 100 ns of pixel 2 is the same as the case of the single pixel, while additional signals are induced on its two neighboring pixels due to charge sharing. On these two pixels, a negative current is induced at first and then succeeded by a weaker and longer-lasting positive current. The charge sharing pulse disappears more quickly in the 20  $\Omega\cdot\text{cm}$  model than in the 200  $\Omega\cdot\text{cm}$  model. The amplitudes of the pulses in the two models are the same, and in both of them a charge of about 50 e has been collected at last. The separate study of the drift and the diffusion charges indicates that the charge sharing effect is caused by the drift charge. A series of particles entering at different positions between the center of pixel 2 and the center of pixel 3 have been simulated to study the edge effect on charge collection. According to the simulation results, less charge is collected while the particle hits the edge of the pixel than when it hits the center. The edge effect is more obvious in the 20  $\Omega\cdot\text{cm}$  model, with 25% less collected charge at the edge in 100 ns. In the 200 ohm model, this effect is mitigated, and the difference in the collected charge in 100 ns between the center and the edge is 20 %. Therefore, it is possible to reduce the influence of the edge effect by increasing the bulk resistivity of the sensors.

The results obtained in this study can be used as the input in many interesting future researches. For example, the 3D simulated results of the electric field can be imported into the charge propagation simulation module of AllPix<sup>2</sup>, to build a realistic simulation of the signal formation process in the ATLASPix 1 with AllPix<sup>2</sup>. By combining this DUT simulation with the simulation model of the FE-I4, a full simulation of the testbeam experiment of the ATLASPix 1 can be obtained. This simulation can help to understand the data from the testbeam experiments of the ATLASPix 1. Apart from the edge effect, the plot of the relationship between the collected charge and particle position shown in Fig. 5.25 also demonstrates the deposited charge in the adjacent pixels if a particle hits a certain place. It can be used to estimate the distribution of cluster size in the x direction on the ATLASPix 1 for upright particles, and can be compared to testbeam data. Besides upright particles, the TCAD model can be adapted to inclined particles, to study the effect of the angles of the incoming particles on the edge effect and the cluster size distribution. It will also be interesting to simulate a pixel matrix in the y direction to look into the distribution of cluster size in this direction. Last but not least, these verified TCAD models can be easily adapted to emulate the other two slightly variant matrices, the ATLASPix IsoSimple and the ATLASPix M2, to compare their performances with the ATLAS Simple and to study the influence of their structural differences. They can also be modified to simulate future devices that are not available in hardware yet.

Appendix A

**Appendix A**

plane	z offset [ $\mu\text{m}$ ]		
1	-200000		
2	-100002		
3	2.43451		
4	454985		
5	555019		
6	625000		
DUT	300000		

(A)

plane	$\alpha$	$\beta$	$\gamma$	plane	$\alpha$	$\beta$	$\gamma$
1	$-167.5^\circ$	$0^\circ$	$0^\circ$	1	$-180^\circ$	$0^\circ$	$0^\circ$
2	$180^\circ$	$12.5^\circ$	$-90^\circ$	2	$180^\circ$	$0^\circ$	$-90^\circ$
3	$-167.5^\circ$	$0^\circ$	$0^\circ$	3	$-180^\circ$	$0^\circ$	$0^\circ$
4	$-12.5^\circ$	$0^\circ$	$180^\circ$	4	$0^\circ$	$0^\circ$	$180^\circ$
5	$0^\circ$	$-12.5^\circ$	$90^\circ$	5	$0^\circ$	$0^\circ$	$90^\circ$
6	$-12.5^\circ$	$0^\circ$	$180^\circ$	6	$0^\circ$	$0^\circ$	$180^\circ$
DUT	$180^\circ$	$0^\circ$	$180^\circ$	DUT	$180^\circ$	$0^\circ$	$180^\circ$

(B)

particle type	$\pi^+$
particle energy	180 MeV
transverse beam size	3 mm
direction	$(9.9 \times 10^{-5}; 9.3 \times 10^{-6} \text{ 1})$
divergence	$(1.8 \times 10^{-4}; 1.1 \times 10^{-4}) \text{ mrad}$

(C)

threshold	3000 e
ADC slope	2100 e/unit
ADC offset	0.5 e

(D)

TABLE A.1: Parameters for the simulation of the FE-I4 telescope. The parameters were extracted from the reconstruction of the data sample. **a**: Offsets of telescope planes and the DUT plane along beam axis. Naming convention of the planes is that the most upstream telescope plane is plane 1, and the most downstream plane is plane 6, and the plane where the DUT is integrated is called DUT plane. **b**: Euler angles of telescope planes and the DUT plane in inclined (left table) and upright (right table) simulation models. **c**: Parameters describing the beam that deposits charge in the planes. **d**: Parameters for the simulated digitizer.

Appendix B

**Appendix B**

well type	deep n-well	n-well	p-well	
doping concentration [ $\text{cm}^{-3}$ ]	$1 \times 10^{16}$	$1 \times 10^{18}$	$1 \times 10^{18}$	
doping type	phosphorus	phosphorus	boron	
length (x) [ $\mu\text{m}$ ]	112	106	30	
width (y) [ $\mu\text{m}$ ]	20	15	12	
thickness (z) [ $\mu\text{m}$ ]	6	2	1	
well type	p-guard ring	dense well at electrode		
doping concentration [ $\text{cm}^{-3}$ ]	$1 \times 10^{16}$	$1 \times 10^{19}$		
doping type	boron	same as the well		
length (x) [ $\mu\text{m}$ ]	around periphery	0.5		
width (y) [ $\mu\text{m}$ ]	5	0.5		
thickness (z) [ $\mu\text{m}$ ]	1	0.9		
bulk resistivity [ $\Omega \cdot \text{cm}$ ]	20	80	200	1000
doping concentration [ $\text{cm}^{-3}$ ]	$6.729 \times 10^{14}$	$1.668 \times 10^{14}$	$6.651 \times 10^{13}$	$1.328 \times 10^{13}$

TABLE B.1: Parameters including the size, doping concentration, and doping type of the bulk and the implant wells used in TCAD structure simulation.

physics	models	sub models
mobility	DopingDependence Enormal HighFieldSaturation	
recombination	SRH	DopingDependence
effective intrinsic density	BandGapNarrowing	Slotboom

TABLE B.2: Physics models used in the TCAD device simulation. The models are provided by the SDevice tool from the Synopsis company.

# Bibliography

- [1] Long, A. A. *The Cambridge Companion to Early Greek Philosophy*, pgs. xxiii, 185.
- [2] Bailey, C. (1928). *The Greek Atomists and Epicurus*, Oxford.
- [3] Clericuzio, A. *Elements, Principles, and Corpuscles; a study of atomism and chemistry in the seventeenth century*, Dordrecht; Boston: Kluwer Academic Publishers, 2000.
- [4] *John Dalton and Atomic Theory*, retrieved from [Lumen Learning Website](#). Accessed 02/12/2018.
- [5] Thomson, J. J. (August 1901). *On Bodies Smaller Than Atoms*, *The Popular Science Monthly*. Bonnier Corp.: 323-335. Retrieved 21/06/2009.
- [6] Chatrchyan, S. et al. (CMS Collaboration) (17/09/2012). *Observation of a new boson at a mass of 125 GeV with the CMS experiment at the LHC*, *Phys.Lett. B* **716** (1): 30-61.
- [7] Aad, G. et al. (ATLAS Collaboration) (17/09/2012). *Observation of a new particle in the search for the Standard Model Higgs boson with the ATLAS detector at the LHC*, *Phys.Lett. B* **716** (1): 1-29.
- [8] *Dark Matter*, Retrieved from [CERN Official Website](#). Accessed 02/12/2018.
- [9] R. Oerter (2006). *The Theory of Almost Everything: The Standard Model, the Unsung Triumph of Modern Physics*, (Kindle ed.). Penguin Group. p. 2. ISBN 0-13-236678-9.
- [10] CERN. *LHC Design Report, Vol. The LHC Main Ring*, [CERN-2004-003](#).
- [11] ATLAS Collaboration (11/4/2012). *Observation of a new  $\chi_b$  state in radiative transitions to  $\Upsilon(1S)$  and  $\Upsilon(2S)$  at ATLAS*, *Phys. Rev. Lett.* **108** (2012) 152001.
- [12] *Supersymmetry*, Retrieved from [CERN Official Website](#). Accessed 14/01/2019.
- [13] Jarlett, Harriet (15/12/2017). *25 Years of Large Hadron Collider Experimental Programme*, retrieved from [CERN Official Website](#).
- [14] ATLAS Collaboration. *Detector&Technology*, retrieved from [ATLAS Official Website](#).
- [15] Mangano, Michelangelo (2/4/2018). *Weighing up the LHC's future* retrieved from [EP Newsletter](#).
- [16] ATLAS Collaboration. *ATLAS Insertable B-Layer Technical Design Report*, [CERN-LHCC-2010-013](#).
- [17] Schmidt, Burkhard (2016). *The High-Luminosity upgrade of the LHC: Physics and Technology Challenges for the Accelerator and the Experiments*, *J. Phys.: Conf. Ser.* **706** 022002.

- [18] Gregor, Ingrid-Maria (2017). *ATLAS Inner Tracker Overview*, 10th Terascale Detector Workshop, DESY Hamburg, Lecture, retrieved from [DESY Indico](#).
- [19] M. Tanabashi *et al.* (Particle Data Group). *The Review of Particle Physics*, *Phys. Rev. D* **98**, 030001 (2018).
- [20] Bohr, N. (1913). *Phil. Mag.* **25**, 10; *Phil. Mag.* **30**, 581 (1915).
- [21] Bethe, H.A. (1930). *Ann. Physik* **5**, 325.
- [22] Bloch, F. (1933). *Z. Physik* **81**, 363 and *Ann. Phys.* **16**, 285.
- [23] Leroy, C. and Rancoita, P.G. *Silicon Solid State Devices and Radiation Detection*, World Scientific Publishing Company Pte Limited, 2012.
- [24] Leroy, C. and Rancoita, P.G. *Principles of Radiation Interaction in Matter and Detection - 2nd Edition*, World Scientific Publishing Company Pte Limited, 2011.
- [25] Born, M., Blin-Stoily, R.J. and Radcliffe, J.M. (1969). *Atomic Physics - 8th Edition*, General Publishing Company, Toronto; reproduced as unaltered replication in agreement with Blakie and Son Ltd. by Dover Publications, Inc., New York (1989).
- [26] Kittel, C. (1996). *Introduction to Solid State Physics - 7th Edition*, John Wiley & Sons, New York.
- [27] Nipun (19/10/2015). *Difference Between p-type and n-type Semiconductor*, retrieved from [Pediaa Website](#).
- [28] [Ioffe Institute Database](#).
- [29] Ramo, S. (1939). *Currents Induced by Electron Motion*, *Proceedings of the IRE* **27** (9): 584-585. doi:10.1109/JRPROC.1939.228757.
- [30] Holbert, E. *Total Ionizing Dose (and Displacement Damage)*, Retrieved from [Lecture notes for EEE598 at Arizona State University](#). Accessed 02/12/2018.
- [31] Garcia-Sciveres, M and Wermes, N. *A review of advances in pixel detectors for experiments with high rate and radiation*, *Rept. Prog. Phys.* **81**, no. 6, 066101 (2018).
- [32] Benoit, Mathieu et al. *The FE-I4 Telescope for particle tracking in testbeam experiments*, *JINST* **11** (2016) no.07, P07003.
- [33] M. Garcia-Sciveres et al. *The FE-I4 pixel readout integrated circuit*, *NIMA* **636** (2011) 155-159.
- [34] Georgakopoulou, K. et al. (17/4/2018). *A 100-ps Multi-Time over Threshold Data Acquisition System for Cosmic Ray Detection*, [Preprint submitted to Journal of Nuclear Instruments and Methods in Physics Research](#).
- [35] *ams AG*, Tobelbader Strasse 30, 8141 Premstaetten, Austria.
- [36] Kiehn, Moritz. *Proteus Pixel Telescope Reconstruction*, [Proteus Website](#).
- [37] Peric, I. et al. *Description of the ATLASPIX Simple and ATLASPIX M2*, *Preliminary v2*.

- 
- [38] Spannagel, S et al. *Allpix<sup>2</sup>: A modular simulation framework for silicon detectors*, *NIMA* **901** (2018) 164-172.
- [39] Geant4 Collaboration. *Geant4 Physics Lists*.
- [40] Wolters, K, Spannagel, S, and Hynds, D (14/03/2018). *Allpix<sup>2</sup> User Manual*, Version v1.1.0.
- [41] *Synopsis*, 690 East Middlefield Road, Mountain View, CA 94043, U.S.
- [42] Lavagno, L., Markov, I. L., Martin, G. E., and Scheffer, L. K. *Electronic Design Automation For Integrated Circuits Handbook*, CRC Press, 2016. ISBN 0-8493-3096-3.
- [43] *TCAD*, Retrieved from [TCAD page on Synopsis official website](#). Accessed 17/12/2018.
- [44] *Sentaurus Structure Editor User Guide*, Version G-2012.06, 06/2012.
- [45] *Sentaurus Process User Guide*, Version G-2012.06, 06/2012.
- [46] *Sentaurus Device User Guide*, Version G-2012.06, 06/2012.